Assessing the susceptibility of existing pipelines to Hydrogen Embrittlement

A combined modelling and in-situ experimental approach

Tim Boot

September 2020

TU Delft

Assessing the susceptibility of existing pipelines to Hydrogen Embrittlement

A combined modelling and in-situ experimental approach

by

Tim Boot

to obtain the degree of Master of Science
at the Delft University of Technology,
to be defended publicly on Tuesday September 29, 2020 at 13:30 PM.

Student number: 4280563

Thesis committee:		
	Dr. Amarante Böttger,	TU Delft department of MSE, chair
	Dr. Vera Popovich,	TU Delft department of MSE, supervisor
	Dr. Carey Walters,	TU Delft department of MT&T, supervisor
	Dr. Ir. Ton Riemslag,	TU Delft department of MSE
	Dr. Poulumi Dey,	TU Delft department of MSE
	Dr. Ping Liu,	Intecsea

TU Delft

TU Delft

Abstract

With fossil fuels being phased out and growing global interest in a hydrogen economy, there is demand for re-purposing existing pipelines for transportation of hydrogen gas. However, hydrogen is known to have adverse affects on the properties of steels. Hydrogen will dissolve in the steel matrix and contribute to a reduction of mechanical properties, causing Hydrogen Embrittlement (HE). There is currently a knowledge gap about the behaviour of pipeline steels and their welds in a gaseous hydrogen environment that prevents re-purposing of pipelines for hydrogen transport.

In this work, a combined approach of modelling and in-situ mechanical testing was used to assess the HE susceptibility of X60 pipeline steel and its girth welds. To this end, a novel tensile setup featuring in-situ charging with high pressure H_2 gas and a sample geometry representing a miniature pipeline was developed and validated. To our best knowledge, this setup design has not been reported elsewhere, making this a breakthrough design. An FEA modelling approach was used to estimate the pre-charging duration as well as to gain an insight into the stress states inside the notched samples.

It was found that both the base and weld metals lose ductility when subjected to gaseous H_2. The base metal showed 27% loss of ductility when subjected to $100\,\text{bar}$ H_2, which further increased to 40% in notched samples. A trend of increasing loss of ductility was found with increasing pressure for the weld metal, which showed up to 14% loss of ductility at $100\,\text{bar}$ H_2. The weld metal also retained more of its reduction in cross-sectional area after fracture in H_2 as compared to N_2 than the base metal. Other characteristics like yield strength and UTS were not affected by the hydrogen gas.

The fracture mechanism in the both metals was found to change from microvoid coalescence (MVC) fracture to quasi-cleavage (QC) fracture. The base metal fracture mechanism changed to QC completely, while the weld metal only showed partial QC fracture. In the base metal, ductile fracture mechanisms like HELP and possibly AIDE were found to be dominant even in the QC fracture mode.

It was concluded that the weld metal is less susceptible to HE than the base metal in a gaseous hydrogen environment. For both metals, HE effects were only observed at high amounts of plastic strain, which is outside of the operating conditions of a pipeline. However, before pipelines can be repurposed for hydrogen transport, fatigue testing should be performed to assess the influence of existing defects and cyclic loading conditions on the HE performance of both steels.

Acknowledgements

First of all, I would like to thank Dr. Vera Popovich and Dr. Carey Walters for their guidance during this research. Their thorough, helpful and honest feedback enabled me to keep a sense of direction during a long project that took many turns. I want to extend my gratitude as well to Dr. Ping Liu for allowing me to work on this project with IntecSea, for the insightful discussions and his continuous support of the project.

Furthermore, Dr. Ir. Ton Riemslag was of great importance for this project because of his innovative ideas for the hydrogen setup. His, as well as Elise Reinton's expertise on mechanical testing was essential for the successful completion of the experiments. I would also like to thank Patrick van Holst for his advice on working with high pressure gasses and for lending us his vacuum pump. Thanks go out as well to Ruud Hendrikx for performing XRF analyses and Sander van Asperen for his advice on sample preparation. From IntecSea I would like to thank Ruud Selker for helping me with constructing the FEA models and working out all the errors, and Dr. Ir. Niels Kerstens for his continued interest and advice on anything relating to the research.

Lastly, I want to express my gratitude towards my parents for their support, for their love and for allowing me to pursue my goals for this project even if it meant further extension of my studies.

Contents

List of Figures

List of Tables

List of acronyms

AIDE	-	Adsorption Induced Dislocation Emission
BM	-	Base Metal
HIC	-	Hydrogen Induced Cracking
HAZ	-	Heat Affected Zone
HE	-	Hydrogen Embrittlement
HEDE	-	Hydrogen Enhanced DEcohesion
HELP	-	Hydrogen Enhanced Local Plasticity
HESIV	-	Hydrogen Enhanced Strain Induced Vacancy formation
HID	-	Hydrogen Induced Decohesion
MVC	-	Microvoid Coalescence
NTS	-	Notched Tensile Strength
QC	-	Quasi-Cleavage
SEM	-	Scanning Electron Microscopy
UTS	-	Ultimate Tensile Strength
WM	-	Weld Metal

1 Introduction

Hydrogen has perhaps never been as relevant globally as it is today. With concerns over climate change ever-growing and bottom-up calls for action against it increasing in severity, governments as well as international bodies are trying to create possibilities of making society more sustainable. Since fossil fuels are a large part of the pollution that causes climate change, finding clean, alternative ways of generating energy is perhaps the most important global issue of our time. Hydrogen is one way of transporting and storing this energy. Although the capability of hydrogen to act as an energy carrier has been known for a long time, large scale implementation has always been looked at with scepticism because it would require immense changes to our existing energy infrastructure. However, with energy technologies developing and the societal pressure for sustainable development growing, implementation of hydrogen as an energy carrier is now being pushed for on a global scale like in the European Green Deal [13].

Offshore wind turbines often produce electricity at night, when the demand for it is low. Hydrogen gas can be generated by splitting water molecules through electrolysis by using energy from these wind turbines, which is generated during off-peak hours. Making use of sustainable electricity to produce clean hydrogen gas (so-called blue hydrogen [67]) is a logical decision since it essentially makes use of excess energy. The hydrogen gas can later be reformed into water to release electricity when the demand for it is higher than the supply.

1.1. Hydrogen projects

By 2030, the Netherlands plans to expand its wind power facilities significantly by placing wind turbines further out from the coast than ever before [74]. A feasibility study was performed by the Dutch electricity grid operator TenneT, Gasunie and DNV GL about the possibility of developing a small island to support operations of a wind field so far from shore [66]. However, even though it proved technically feasible, the Dutch government decided not to implement this strategy because of fears of not completing the project within time limits [75]. The plan was put on hold, but a consortium of companies named OSF (Offshore Service Facilities) called for a further need for research into a possible island because generating hydrogen gas on this island by electrolysis and transporting it to land through existing pipelines could provide cost benefits [52]. For this purpose, a grant was given to various companies to investigate possible scenarios for either partially or fully converting electricity to hydrogen offshore and transporting it through pipelines that are already in position on the sea floor, but will not be used anymore by the time the island is completed [68]. This project is called IJVERGAS, after the zone in which new windmills will be placed by 2030, as depicted in Figure 1.1 as IJmuiden Ver. A Delft engineering company called Intecsea is part of the IJVERGAS project because it involves transporting hydrogen gas through offshore pipelines. They are tasked with calculating operational parameters for the existing pipeline like the operating pressure and are collaborators on this thesis.

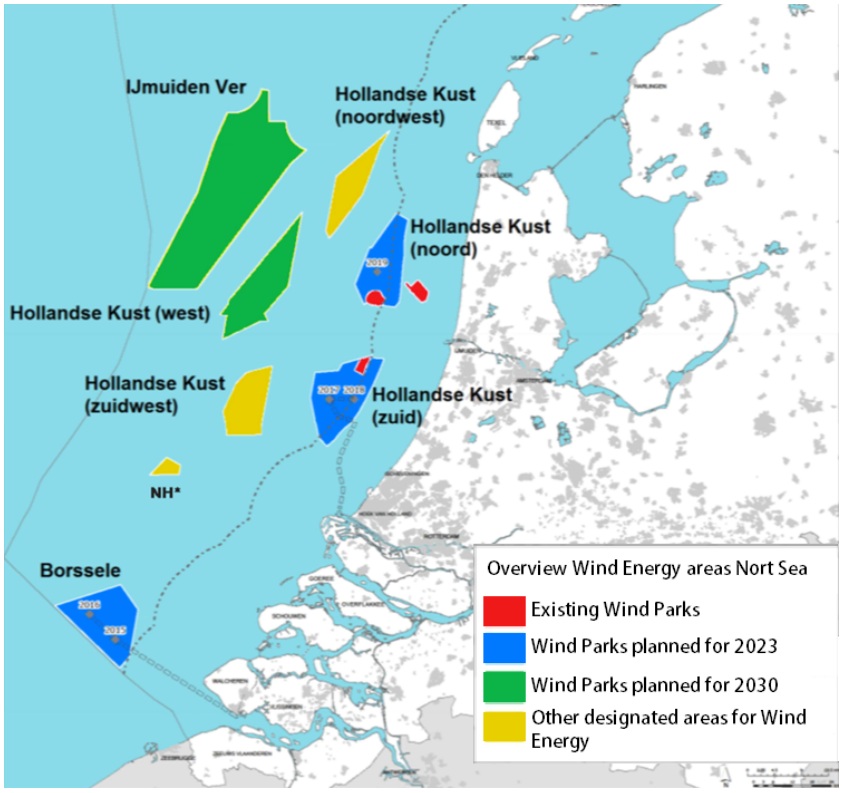

Figure 1.1: Locations of current and future wind parks off the Dutch coast, and the years they will be in use. Adapted from [53].

Other than this project, a similar but not identical structure called NortH2 is planned using wind parks offshore in Groningen. In this case the energy would be generated offshore which is used to produce hydrogen onshore [48]. The hydrogen would be transported through the national gas grid, because natural gas is expected to be either partially or completely phased out during the coming decades. The transport of hydrogen through the national gas grid is the subject of a different project called HyWay27 [58].

The IJVERGAS project distinguishes itself from the others because it would involve pipelines that have already been in use for a different gas for several decades. This involves an older X60 grade pipeline steel. To calculate operating parameters, the interaction between hydrogen gas and the pipeline steel will need to be further understood.

1.2. Hydrogen Embrittlement

Effects of hydrogen on steel are generally characterised as Hydrogen Embrittlement (HE). This finds its origin in 1875 when Johnson discovered that iron, after being submerged in acid, turned more brittle [28]. Similar observations have been made for different metals and steels; after being exposed to hydrogen, metals break at a shorter elongation than they normally would. This effect, along with a consequential reduction in toughness, are all characteristics of brittle behaviour of metals. Therefore, the term hydrogen embrittlement was adopted. However, because hydrogen is the smallest element in the periodic table, detecting it is hard, and evidence of HE was limited to effects of its consequences until recent decades when advances in microscopy allowed for atom-level detection. Multiple models to explain the behaviour of hydrogen inside metals have been proposed since then which although accepted, have not yet been fully understood. These models will be discussed in Chapter 2.

In the offshore industry, the effects of hydrogen have also been noticed for quite a while. Offshore structures are usually protected from corrosion by cathodic protection, which creates a negative potential on the pipeline that inhibits the corrosion reactions. The same potential, however, acts as a driving

force to dissociate hydrogen atoms from seawater and promote them into the steel. This is a frequent cause for failure in the pipeline industry. Coatings are utilised to isolate the pipeline steel from seawater, but as soon as the coating fails in one location along the pipeline, hydrogen is absorbed there. If an offshore pipeline is well designed, the coating does not fail and therefore HE is avoided. However, when hydrogen gas is to be transported through pipelines, the area of contact with the pipeline will be its inside surface. Furthermore, hydrogen will be present throughout the entire operation lifetime of the pipe which will result in absorption into the steel.

Other than the pipeline steel itself, the weld zones in a pipeline are areas of special interest. Large diameter pipelines, ones that are formed from plate material, contain two different welds. One is a longitudinal weld, along the axis of the pipeline, that is used to weld one side of the plate material to the other to form a pipe. The other is a girth weld, or butt weld, that is used to connect different sections of the pipeline. As such, the girth weld is made along the circumference of each section of a pipeline. Weld zones are an area of special interest because they often cause inconsistencies in the wall thickness of the pipeline because of weld toe and weld root geometry, and because they have a different composition and microstructure from the base pipeline steel. Therefore, they will have different responses to a hydrogen environment.

1.3. Problem statement

Offshore pipelines that have been in use to transport natural gas for several decades are planned to transport hydrogen gas in the future. However, current knowledge of the effect of hydrogen gas on pipeline steels and especially their weldments is lacking. This goal of this thesis is to provide new knowledge about the effects of hydrogen gas on X60 pipeline steel and its weldment, and assess the HE susceptibility of both.

1.4. Structure of this thesis

This thesis presents new knowledge about the influence of hydrogen gas on X60 pipeline steel and its girth weld as well as validates a new in-situ tensile setup which allows for characterisation of HE behaviour in pipe-like welded samples under gaseous hydrogen. Chapter 2 provides an extensive literature review into hydrogen effects and HE characterisation methods. Chapter 3 describes the characterisation of pipeline material as well as the experimental and computational methods used in this thesis. The results of the tests performed for this research are presented and discussed in Chapter 4. Finally, conclusions about the research will be drawn and recommendations for future research will be given in Chapter 5.

2

Literature Review

This chapter will serve as a summary of the literature research that has been done for this thesis. Firstly, an introduction will be given on pipeline steels in general. Next, the theoretical background of hydrogen embrittlement will be discussed in terms of the interaction of hydrogen with metals. Afterwards, this background will be used to touch upon the effects that hydrogen has on pipeline steels specifically. Next, different methods of hydrogen charging and measuring will be discussed to provide necessary background information for tests that will be performed for this thesis.

2.1. Pipeline steels

Steels are made to have a wide range of material properties. Alloying, heat treatment and mechanical treatment can be used to create ductile and tough, or strong but brittle steels. Generally, pipeline steels are low alloy steels, designed to be tough rather than strong. Their microstructures contain large amounts of ferrite, which gives the steels the ductile properties necessary for fatigue resistance and weldability. There are several standards of performance for pipeline steels, of which a widely used one is API 5L, a standard by the American Petroleum Institute [25]. Steel grades that fall within this standard are ranked grade A, grade B and X42 - X120. Each grade is held to minimum (and maximum) limits for yield strength, UTS and, elongation and composition. The numbers behind the letters X represent the minimum yield strength in ksi (kilopounds per square inch, one ksi is equal to 6.9 MPa). A general overview of steel grades throughout the last century through 2001 is given in Figure 2.1.

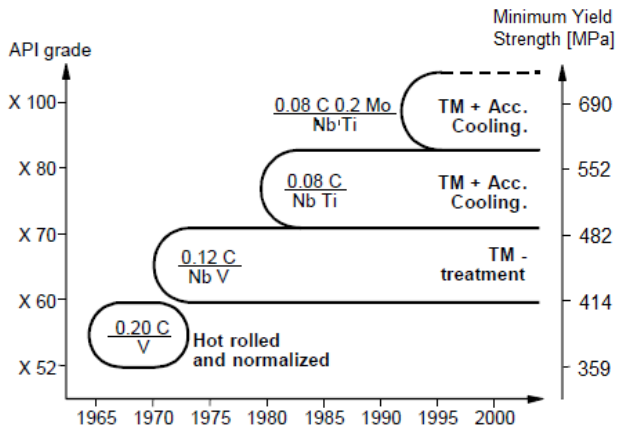

Figure 2.1: Evolution of pipeline steels throughout the last century. Adapted from [22]. Defining elements are noted as well as their required maximum contents in mass%.

The first grades of pipeline steel were created using normal hot rolling. Alloying elements were added to provide strength through precipitation hardening, and microstructures in these steel consisted mainly of ferrite and pearlite phases [22]. Around 1970, companies started making use of thermomechanical (TM) rolling and heat treatments to create microstructures that could not be reached with normal cooling. In X70 steels, average grain sizes are smaller than in X52 and X60 steels, because grain refinement is the only way to increase both strength and toughness. In these steels, strength is obtained from dislocation hardening as well as precipitation hardening, leading to better mechanical performance. Because more strength is obtained from other sources than alloying, the carbon content in these steel is lower to improve weldability at a similar strength. About a decade later, accelerated cooling (Acc. Cooling) was added to create even finer microstructures. Through quick cooling, ferrite/bainite structures can be created that provide a stronger steel, while still having adequate toughness. By controlling cooling rates, the percentage of bainite in the overall microstructure can be controlled, so that even less carbon has to be added to the steel, once again improving weldability. After this, reaching even higher strengths was made possible by adding new alloying elements that dissolved in the ferrite phase, to create a form of solution hardening.

2.2. Hydrogen interaction with steel

2.2.1. Hydrogen absorption, diffusion and trapping

The interaction between hydrogen and metal was recognised as early as 1875 when Johnson noted the brittle behaviour of iron wires after submerging them in acids that produce hydrogen [28]. He also noticed that hydrogen was present in parts of wires that were not immersed in the acid, meaning that hydrogen diffuses into and throughout the iron. When comparing an iron wire with a steel wire, diffusion was much more prominent in the iron wire. However, because of the tiny scale at which hydrogen interaction with steels occur, real understanding of the behaviour of hydrogen in a metal did not occur until well into the next century.

Different mechanisms of absorption

The process of hydrogen absorption into a metal consists of multiple steps. When hydrogen gas comes into contact with an open metal surface, molecules that find their way to the surface are physisorbed by Van der Waals forces. Next, chemisorption occurs, which dissociates the H_2 molecule into two H atoms that become adsorbed on the surface and in sub-surface layers of the metal [5]. This reaction is shown in Equation 2.1. These atoms can then consequently be absorbed into the bulk of the metal, or they can recombine into a hydrogen gas molecule. The former is given in Equation 2.2, and the latter is the exact opposite of Equation 2.1.

$$\mathrm{H_2(g)} \longleftrightarrow 2\,\mathrm{H_{ads}} \tag{2.1}$$

$$\mathrm{H_{ads}} \longleftrightarrow \mathrm{H_{abs}} \tag{2.2}$$

Since both these reactions are reversible, an equilibrium develops between the concentration of hydrogen in the metal and the partial pressure of hydrogen gas in the environment. For diatomic gases such as H_2, this equilibrium was first described by Sievert [61]. It was described by Hirth [23] as

$$c_{\mathrm{o}} = 0.00185\sqrt{P}\exp\frac{-3440}{T} \tag{2.3}$$

where c_{o} is the atom fraction of atomic hydrogen at the surface, P is the hydrogen gas pressure in bar or $0.1MPa$ and T is temperature in K. The term 0.00185 was empirically obtained for diatomic gasses.

However, in many practical cases and literature studies, hydrogen is promoted into a metal by means of a cathodic current or potential created in the metal acting as a driving force [10, 16, 50, 55, 65, 77, 78]. This happens, for example, in cathodic protection of pipelines in sub-sea or acidic soil conditions, or in pipelines that transport a sour gas or liquid containing H_2S. The mechanism of absorption works differently in these cases. Instead of gaseous hydrogen, ionic hydrogen is present in

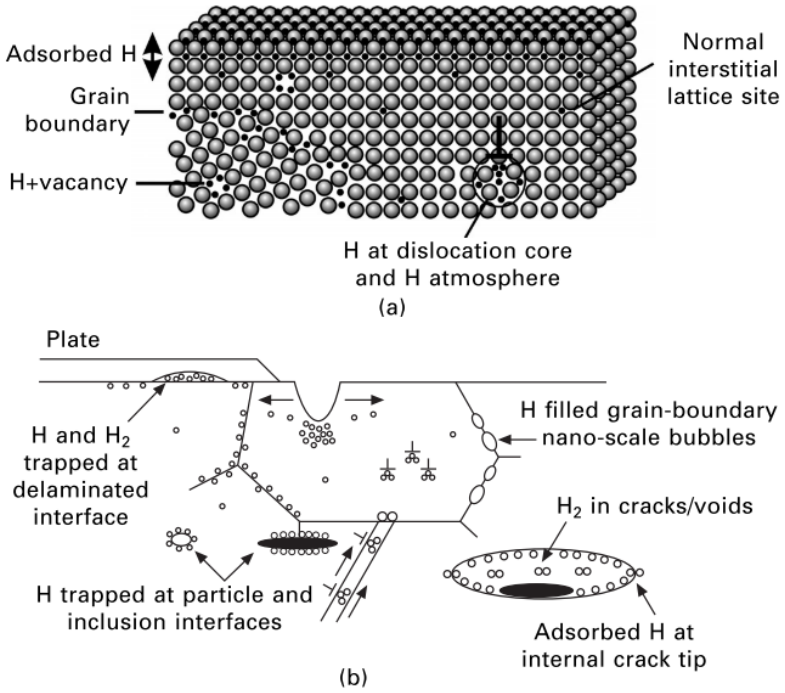

Figure 2.2: Possible trapping sites for hydrogen inside a metal. Taken from [34].

the environment. The ions combine with electrons from the metal provided by the current or potential to form atomic hydrogen that adsorbs on the surface and sub-surface layers [70]. This happens according to Equation 2.4. The reduction of water could also occur, as shown in Equation 2.5.

$$H^+ + e^- \longleftrightarrow H_{ads} \tag{2.4}$$

$$H_2O + e^- \longleftrightarrow H_{ads} + OH^- \tag{2.5}$$

Similar to the equilibrium in gaseous environments, the adsorbed hydrogen atoms can recombine into molecules. Initially, these will dissolve in the environment, but after the solubility limit has been reached, they will transform to gas bubbles on the surface of the metal.

Hydrogen trapping

Darken and Smith [14] were the first to suggest that diffusion of hydrogen into a metal is impeded by imperfections created in the lattice by cold-working a metal. Oriani then built on this and suggested that these imperfections act as ”extraordinary sites” or traps for hydrogen [51]. Different traps have a different depth, or potential, which is their relative energy level compared to an interstitial lattice site. Oriani then went on to develop a formula to calculate the equilibrium between hydrogen stuck in traps, and hydrogen that is free to diffuse, and a way to quantify the amount of traps. He reaches the conclusion that there is a relation between the amount of traps and the amount of diffusion of hydrogen in a metal, and that grain boundaries and micro-cracks rather than dislocations act as strong hydrogen traps.

In later decades, a more complete understanding of the trapping of hydrogen was developed, and several features of a poly-crystalline metal were identified as trapping sites. These have been summarised by Lynch [34] and are shown in Figure 2.2. Listed in approximate order of strength (weak to strong), they are:

- Solute atoms.
- Free surfaces and spaces in between the first few atomic layers under a surface.

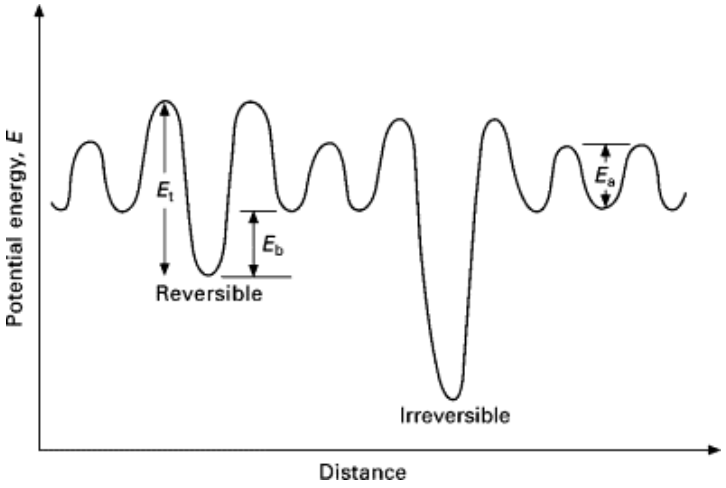

Figure 2.3: A graphic representation of the energy level of hydrogen atoms in a metal. The lattice sites have small energy level fluctuations (E_a) compared to both the reversible and irreversible traps. E_b is the energy level of a trap compared to a lattice site, and E_t is the energy needed to release a hydrogen atom from the trap. E_t rather than E_b determines whether a trap is reversible or irreversible. Taken from [70].

- Vacancies and vacancy clusters.
- Dislocation cores and strain fields.
- Grain boundaries.
- Interfaces between precipitates and the matrix, and strain fields around precipitates.
- Interfaces between inclusions and the matrix.
- Voids and internal cracks.

Furthermore, if voids within the matrix are large enough, hydrogen atoms can recombine into H_2 molecules. If the concentration of hydrogen in the metal is large enough, the formed hydrogen gas pressure can be so high as to initiate cracking in the material. This can happen in voids in between grain boundaries, but also in voids created on an inclusion interface.

In practice, a distinction is often made between reversible and irreversible hydrogen traps. A graphic overview of trap energies is given in Figure 2.3. A trap is reversible when the hydrogen that it contains after being in a hydrogen environment can be released with energy obtained at relatively low temperatures. The energy needed to release hydrogen from a trap is given by E_t in the figure. Weakly trapped hydrogen can therefore desorb from a metal at room temperature. Irreversible traps store the hydrogen contained within them, and only release it at higher temperatures. Castaño Rivera et al. [59] estimated trap densities and energy levels for an API 5L X60 steel. They identified an energy level of $35\,\mathrm{kJ\,mol^{-1}}$ as the distinction between reversible and irreversible traps. Consequently, they find multiple deep traps, which they suspect belong to voids formed in the lattice and around inclusions. Shallow trap energies are coupled with everything above grain boundaries in the list given by Lynch. The study by Castaño et al. also suggests grain boundaries to be shallow traps. However, a study by Maroef et al. characterises grain boundaries in a steel weld metal as having a binding energy of between 18 and $53\,\mathrm{kJ\,mol^{-1}}$ [35]. This large difference in binding energy, spanning reversible and irreversible levels, could be explained by precipitations that are present in some grain boundaries, giving them a higher binding energy than others [40].

Different charging methods result in different absorption conditions. When hydrogen is absorbed by a metal, it occupies traps with a high binding energy first, as shown by Zhao et al. [78]. Only when these traps are occupied, does the hydrogen enter more shallow, reversible traps. Strong hydrogen traps are filled in both charging methods, but cathodic charging methods keep generating hydrogen atoms at the metal surface, leading to a larger concentration of weakly trapped hydrogen in surface

regions. Zhao et al. also showed that this situation is different when the metal is in a gas environment. This is because the diffusion into the bulk is the limiting factor in hydrogen absorption from a gaseous environment. A low surface absorption rate in a gas environment leaves time for the hydrogen to diffuse throughout the bulk, whereas the surface reaction in cathodic charging methods is much faster than bulk diffusion, leading to a surplus of hydrogen atoms near the metal surface that results in a concentration gradient. Care needs to be taken that experiments done with cathodic charging methods might provide very different results than ones done in a high pressure hydrogen gas environment.

2.2.2. Mechanisms of Hydrogen Embrittlement

Once atomic hydrogen has entered a metal, and is trapped within it, it can affect the properties of the material. The most important effect is that it changes the mechanical properties of the metal to behave in a more brittle way, which is why this effect is called hydrogen embrittlement. Rather than a single embrittlement mechanism, several models have been developed to explain brittle behaviour of metals under influence of hydrogen.

Hydrogen Induced Cracking (HIC)

HIC is a process that causes internal cracking of a steel because of the presence of hydrogen gas inside cavities in the material. Small cavities can be present in steels, and are mostly associated with inclusions in the steel matrix. Large non-metallic inclusions are not completely compatible with the bulk matrix, which results in small mismatches that form cavities large enough for hydrogen atoms to combine into hydrogen gas molecules [27]. By a similar relation as Equation 2.3, the gas pressure inside the cavity can become high enough to enlarge the cavity, allowing more gas to form. Susceptibility of steels to HIC depends on the amount and geometry of inclusions, the hydrogen concentration in the steel and the stress state [43]. Other than being a damaging mechanism in itself, cavities created during HIC are also areas where cracks often initiate. In practice, HIC is often observed as blister-like bubbles on the surface of the steel, which is called blistering. Because pipelines often operate in sour environments where they transport gasses that contain partial pressures of H_2S, hydrogen damage has been relevant for the past few decades even when not transporting hydrogen gas. Research shows that if pipelines fail, they often fail because of hydrogen that is absorbed from the sour gas, diffuses into the steel and initiates cracking around inclusions. This will be discussed in more detail in Section 2.3.

Hydrogen Enhanced / Induced Decohesion (HEDE or HID)

The earliest described model of hydrogen embrittlement is HEDE, which is a mechanism where hydrogen present in a metal lattice weakens the atomic bond strength of the metal ions. Troiano described it in 1960 as donation of the 1s electron of hydrogen to the unfilled 3d shell of iron ions [69]. This weakening of inter-atomic potential creates the preference for tensile separation of atoms rather than slip, creating brittle rather than ductile fracture behaviour. Such tensile decohesion can happen at sharp crack tips, at high stress regions in front of the crack tip, or even at the interface between inclusions and the metal matrix. The HID mechanism was first proposed by Gerberich et al. in the 1970s to explain the decrease in crack tip opening with increasing hydrogen concentration. They combine atomistic modelling with experimental data to show that several nanometers in front of a crack tip, hydrogen concentrations are locally increased up to 1 hydrogen atom per iron atom, which decreases the stress needed to cause decohesion in that region [20]. Proof for the HEDE mechanism has been obtained in simulations for example by Koyama et al. who found an influence of hydrogen concentrations at grain boundaries on the reduction of cohesive energy [31] and Katrazov and Paxton, who found a reduction on the cohesive strength between iron atoms due to dissolved hydrogen [29].

Hydrogen Induced Local Plasticity (HELP)

In 1972, Beachem suggested that hydrogen assisted cracking could occur because of the presence of solute hydrogen that facilitates dislocation movement [7]. A high content of soluble hydrogen in front

of crack tips reduces the stress needed to unlock dislocations, leading to localised plasticity. The dislocations combine to create microvoids and accelerate their growth. A high number and growth rate of voids in the region in front of a crack tip leads to an accelerated crack growth rate which translates to a more brittle behaviour macroscopically. The effects of HELP have been identified in several studies. Robertson showed that presence of hydrogen gas can propagate previously stationary dislocations and speed up moving dislocations by in-situ TEM testing [60]. These effects were shown to be reversible upon removing of the hydrogen gas, showing that they depend on diffusable hydrogen like the HEDE mechanism. The same author, with colleagues, also showed that a hydrogen environment reduces the distance between individual dislocations in a dislocation pileup [19]. Barnoush and Vehoff studied the effect of hydrogen on nickel in in-situ nano-indentation experiments [6]. They find that hydrogen affects the energy required to nucleate dislocations, making it easier for a material to undergo plastic deformation. The results of this effect were seen in their experiments as a decrease in pop-in load during the test when using an increasing load, and a decrease in pop-in time when using a constant load. Furthermore, fractographic effects of the HELP mechanism have been observed in several studies, in the form coalescence of microvoids and microscopic dimples on fracture surfaces that appear at first to be the result of brittle cleavage fracture[21, 37, 47].

Adsorption Induced Dislocation Emission (AIDE)
In normal ductile failure, dislocations created in the plastic zone in front of the crack tip cause crack tip blunting and crack growth by moving away from the crack tip. However, because they are created away from the crack tip, only a small amount of dislocations cause crack growth. Clum [12] was the first to couple adsorption of hydrogen to the nucleation of dislocations at surfaces. The AIDE mechanism was first proposed by Lynch in 1975 [33]. He argues that the enhanced nucleation of dislocations due to adsorption of hydrogen leads to a larger amount of dislocation creation at the crack tip. Under the applied stress, these dislocations can easily move away from the crack tip, leading to crack growth. This also happens at the interfaces of microvoids. Accelerated crack growth, as well as microvoid coalescence lead to fast crack advancement and brittle behaviour. The AIDE mechanism contributes to the formation of smaller dimples in the fracture surface by increasing the nucleation and growth rate of microvoids ahead of a crack tip. No direct evidence of the AIDE mechanism exists, but it is rather obtained by research that shows that large amounts of adsorbed hydrogen exist in the first few atomic layers beneath a metal surface and by observations of embrittlement at crack growth rates that are too large for hydrogen diffusion towards the crack tip to be possible [11, 32]. HE fracture surfaces also show similarity to those made under influence of Liquid Metal Embrittlement (LME), which happens when a metal comes into contact with another metal in liquid form. LME has been proven to also reduce surface energy of the solid metal [49], which could explain behaviour similar to that during HE.

Hydrogen Enhanced Strain Induced Vacancy formation (HESIV)
The HESIV model is the most recent of all models discussed in literature, being first proposed by Nagumo as recently as 2004 [45]. He explains a change in material behaviour not because of the hydrogen concentration per se, but because of a steel's likelihood to form vacancies upon straining. A higher vacancy concentration means a larger uptake of hydrogen, leading to brittle behaviour. Furthermore, hydrogen-iron interactions have been shown to lead to an increased vacancy formation upon straining by McLellan and Xu [38]. When a large amount of vacancies is present, they can combine into voids, resulting in faster crack growth. Because the HESIV model only explains the increased presence of voids in metals under the presence of hydrogen, it is not an embrittlement model by itself. However, the mechanisms described by the model can work in combination with other models.

2.2.3. Characteristic fracture surfaces

In practice, two or more of the presented mechanisms occur at the same time when crack growth occurs and they both contribute to crack tip advancement. A graphic overview of the processes working in parallel can be seen in Figure 2.4. In general, what mechanism has been dominant during different phases of fracture can be identified from the fracture surface.

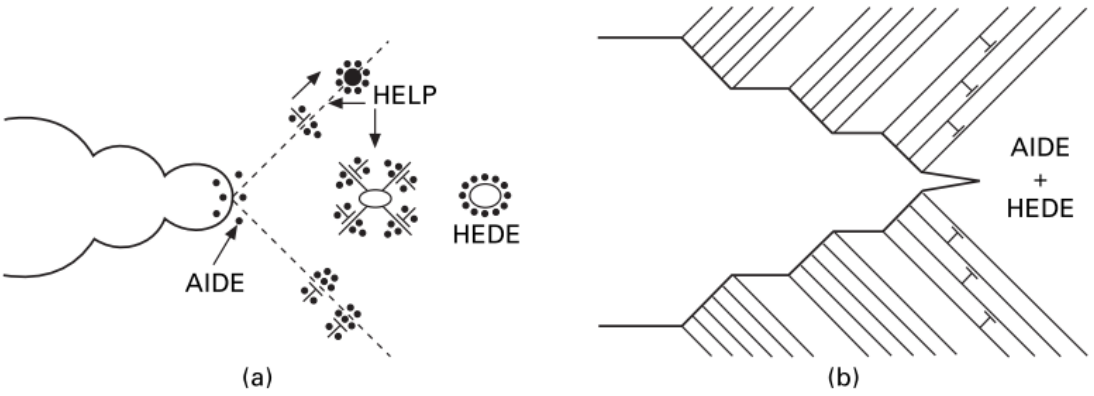

Figure 2.4: A graphic representation of different HE mechanisms working in parallel to accelerate crack propagation. Taken from [34].

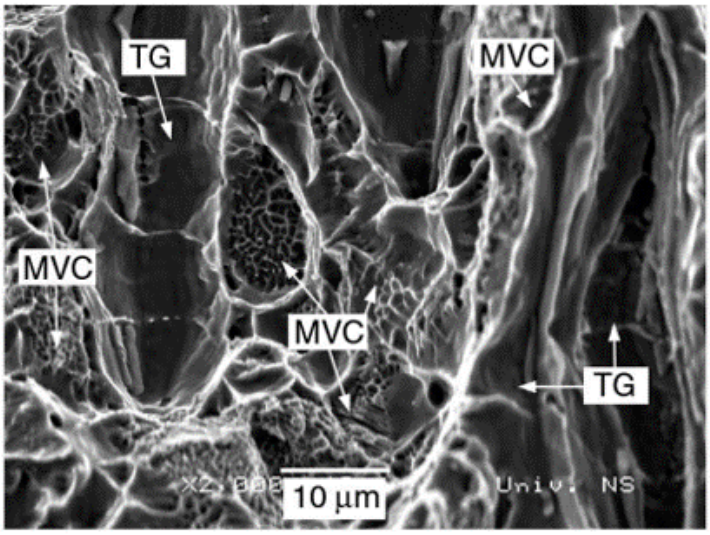

Figure 2.5: A fractographic observation of transgranular (TG) quasi-cleavage fracture related to HEDE, and microvoid coalescence (MVC) fracture related to HELP. Adapted from [15].

Since the HELP, HESIV and AIDE mechanisms contribute to the formation and coalescence of microvoids, dimples should be visible on the surface on a microscopic scale. So-called Microvoid Coalescence (MVC) fracture is the characteristic fracture mode of ductile steels without effects of hydrogen gas as well. However, because of the accelerated void growth and formation due to dissolved hydrogen, grow less before coalescing. The result is that dimples on the fracture surface of a steel that contained dissolved hydrogen are of a much smaller scale. Where normal MVC dimples are on the scale of several µm, dimples on surfaces that underwent HE can be of sub-micron or even nanometer scale [37]. MVC happens within the steel matrix inside grains, and fracture will therefore propagate through grains themselves. This is called trans-granular fracture. If the HEDE mechanism was more dominant, fracture surfaces appear flatter at a microscopic scale, while they still might be dimpled on the nano scale and cannot easily be identified with normal SEM. The HEDE mechanisms has been shown to decrease the cohesive energy both at grain boundaries and between atoms in the matrix. Therefore, this mechanism is associated both with transgranular fracture and intergranular fracture, which means that fracture happens at grain boundaries and propagates in between grains. A fractographic observation from Djukic et al. can be seen in Figure 2.5, where the fracture surface consists of transgranular fracture related to the HEDE mechanism and more ductile MVC to HELP [15].

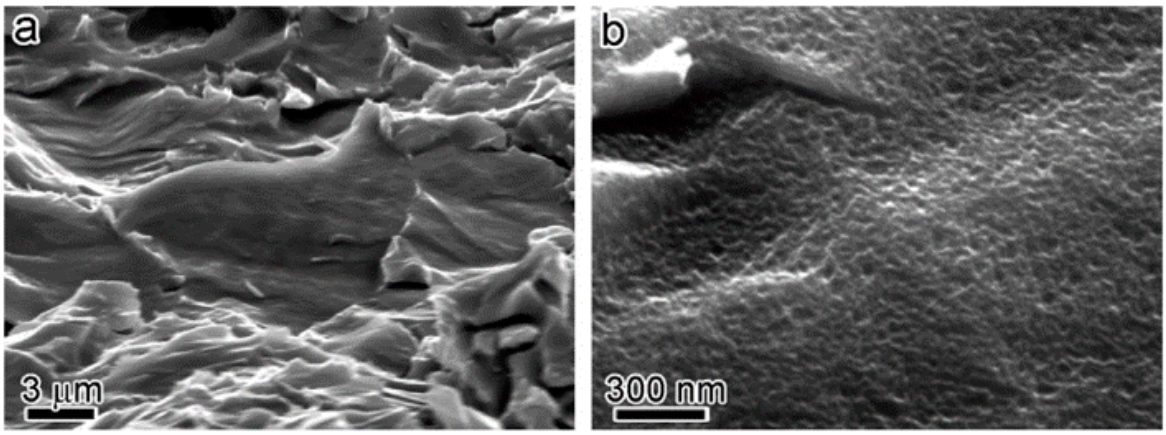

Figure 2.6: Smooth facets on a quasi-cleavage (QC) fracture surface that are shown to be dimples on a nanoscale. Adapted from [37].

Cleavage and Quasi Cleavage fracture

The characteristic fracture mechanism for brittle fracture is called cleavage fracture. Rather than by coalescence of voids, the material fails by fracturing of interatomic bonds across certain planes of the matrix. These planes are called cleavage planes and are continuous throughout individual grains. The crack will propagate along a cleavage plane in one grain, then change direction to adhere to a cleavage plane in other grains. This gives rise to characteristic smooth facets that can be observed on the fracture surface. When hydrogen is introduced in the system, a fracture surface arises that is called Quasi Cleavage (QC). QC fracture shows facets just like cleavage fracture, but there are several differences. Merson et al. study the facet sizes and orientations of true cleavage and quasi cleavage fracture [39]. They find that although the size of facets in both mechanisms is similar, the average misorientation angle between facets is much smaller for QC. This means that QC fracture does not adhere to the same cleavage planes as true cleavage does. Furthermore, they discover that the crack can change direction within one grain, which supports this theory. They suggest that plastic deformation plays a role in QC fracture.

Martin et al. study QC fracture surfaces in two different papers [36, 37]. They identify three characteristic features of a QC fracture surface; secondary cracking, smooth surfaces and ridges. They go into more depth on the latter two, which are shown here in Figures 2.6 and 2.7 respectively. For both features, they find a high density of dislocations beneath the fracture surface, proving that plastic deformation was involved. As seen in Figure 2.6, facets that appear to be smooth at lower magnifications actually are dimpled on a nano scale. The authors link this to the HELP mechanism of fracture. For the characteristic ridges, they propose a model where fracture is induced by dislocations gathering at slip band intersections, their mobility influenced by hydrogen, that combine to form voids. These voids grow to the point when they almost intersect, which is when the material in between them ruptures, leaving behind sharp ridges that match on both sides of the fracture surface. This model has been visualised in Figure 2.8.

Even though QC fracture surfaces can look similar to those found in true cleavage, these findings suggest that the mechanisms behind quasi cleavage fracture are distinctly different from those in play for true cleavage fracture.

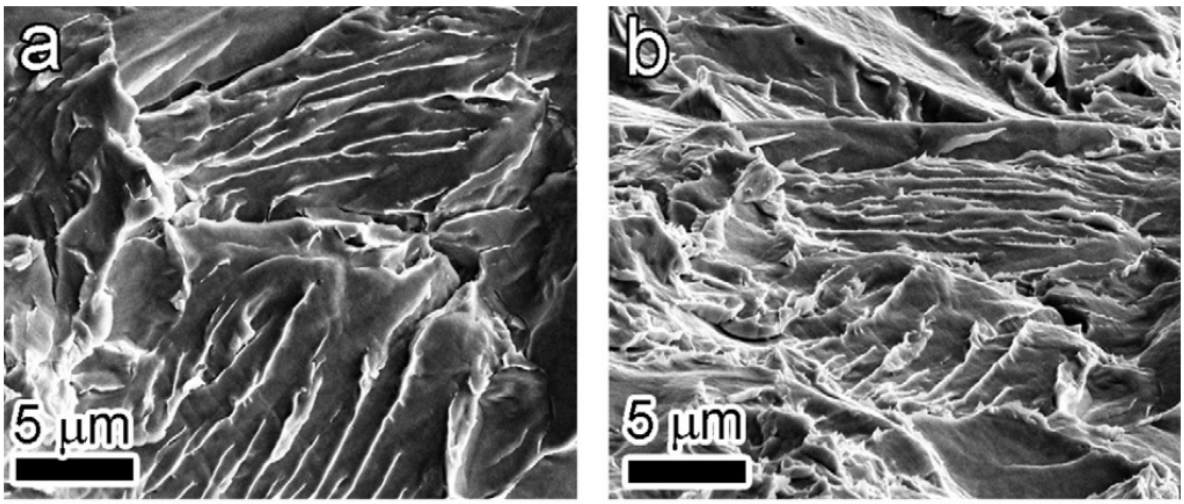

Figure 2.7: SEM imaging of characteristic ridges found on a quasi-cleavage (QC) fracture surface. Adapted from [36].

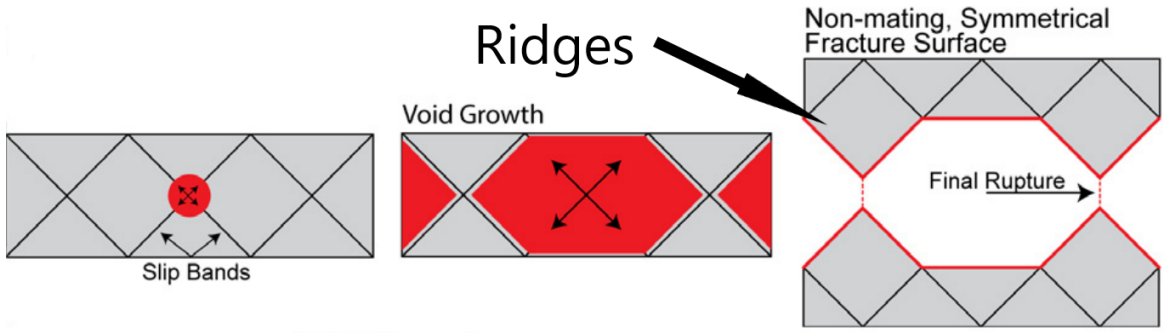

Figure 2.8: The fracture mode model proposed by Martin et al. to produce characteristic QC ridges. Adapted from [36].

2.3. Hydrogen effects on pipeline steels

In the previous section, the fundamental mechanisms behind hydrogen embrittlement were discussed. In this section, the effects hydrogen embrittlement has on pipeline steels will be dealt with. The susceptibility of different types of pipeline steels will be discussed, as well as the specific effects on mechanical performance that the presence of hydrogen in a steel has.

2.3.1. Hydrogen absorption

Hydrogen absorption can happen in a number of ways. Most commonly, hydrogen is absorbed during the steelmaking process because molten and high temperature steels have a high hydrogen solubility. Other than that, processes like surface coating, welding or pickling can also introduce hydrogen into a metal. Especially electrochemical processes like coating, pickling or corrosion cause high amounts of hydrogen to be absorbed, up so several ppm [64]. Pipeline steels are available in various grades, which have various characteristic microstructures, as was discussed in Section 2.1. The difference in susceptibility of different steels to hydrogen embrittlement has been researched extensively in the literature. This section summarises relevant studies that characterised these differences.

Park et al. produced different microstructures from the same X65 steel by changing the heat treatment and characterised the reaction of these microstructures to hydrogen [55]. Their results have been shown in Table 2.1. The three distinct microstructures they produce all have ferrite as their main phase, but differ in second phase between degenerated pearlite (DP), acicular ferrite (AF) and bainite (B).

Table 2.1: Hydrogen permeation data for tested steels. F, ferrite; DP, degenerated pearlite; AF, acicular ferrite; B, bainite; D_{app}, apparent diffusivity; $J_{app}L$, permeability; C_{app}, apparent solubility. Taken from [55].

Specimen	Microstructure	Fraction of DP/AF/B	M/A fraction	D_{app} (10^{-10} m^2 s^{-1})	$J_{ss}L$ (10^{-9} mol_H/ms)	C_{app} (mol_H/m^3)
A1	F/DP	3.75	1.28	9.27	13.3	14.33
A2	F/AF	8.12	5.73	4.05	8.47	20.91
A3	F/DP	3.93	0.88	9.38	12.9	13.79
A4	F/B	9.38	4.45	4.44	12	27.13

D_{app} represents the diffusivity of hydrogen in the lattice and reversible traps, $J_{ss}L$ the permeability of hydrogen and C_{app} the hydrogen trapped in the lattice and reversible traps. The main observation in this and other related papers [50, 62, 77], is that a decrease of D_{app} and $J_{ss}L$ often corresponds to an increase in C_{app}, meaning that more hydrogen is trapped and less hydrogen diffuses through the material. This signifies a high trap density. What can be distinguished in these particular microstructures is that the F/AF and F/B microstructures have lower diffusion and higher solubility than the F/DP steels. This leads to the conclusion that AF and F/B phases, which are high in M/A (Martensite/Austenite) fraction, have a large concentration of reversible trap sites. However, the trend of low diffusion linked to high solubility does not continue between these two samples. Therefore, using another diffusible hydrogen measuring method, the authors measured the diffusible hydrogen content of the samples once more. This showed that the amount of diffusible hydrogen is higher in the AF microstructure, most likely because of the high density of grain boundaries and dislocations. Another interesting observation in their data is that the diffusivities for all of the microstructures are lower than the normal diffusivity in α-iron, which is on the order of 10^{-9} m^2 s^{-1} [30]. This means traps that slow down diffusion are present in all microstructures.

Olden, Alvaro and Akselsen performed similar expriments on X70 pipeline steel, a weld metal (WM) and a simulated heat affected zone (HAZ) [50]. They report a ferrite/pearlite microstructure for the base metal (BM), a largely martensitic phase for the HAZ, and an AF and polygonal ferrite weld metal. The susceptibility to hydrogen embrittlement increases in the order of BM, WM, HAZ. This supports previous findings that AF and martensitic structures are more susceptible to hydrogen embrittlement than metals with a F/P or F/B microstructure. In this study, the structure of the HAZ had a much higher martensite fraction than the metal tested in the study by Park et al., which is why the susceptibility is likely to be greater than that of the weld metal.

Because Park et al. studied four microstructures created from the same steel, they disregarded the influence of inclusions on the difference in hydrogen content [55]. However, they do recognise the important role inclusions play as deep traps for hydrogen, thereby increasing the material's susceptibility to HIC. Many studies have been performed to assess different steels' susceptibility to HIC and the microstructural differences between them [16, 24, 27, 42, 43]. However, because pipelines often operate in sour environments, transporting gases that contain partial pressures of H_2S, hydrogen damage and HIC has already been relevant for the past few decades.

In the 1980s, a relationship between the susceptibility of pipeline steels, inclusions and certain alloying elements was already discovered [9]. In a more recent paper, Mohtadi-Bonab et al. show the existence of cavities and crack initiation near a MnS inclusion, as shown in Figure 2.9 [42]. MnS inclusions are considered especially harmful because they are soft, which means that they are elongated during the rolling process of the steel. This causes them to become sharp inclusions that cause high stress concentrations. The discovery of these microstructural relationships to HIC lead to the development of special Sour Service (SS) pipeline steels [22]. Pipelines for sour service are generally used when the medium that is transported contains H_2S, which is a source of hydrogen. Pipeline steels for sour service have lower alloying contents than normal pipeline steels, making them more ductile, but less strong. This means that lower grade steels can be made less susceptible just by reducing the alloying content. However, the loss of strength means that higher API grades cannot easily be reached.

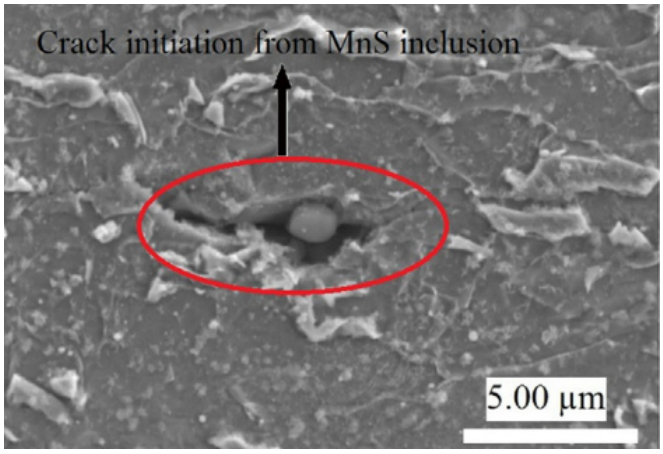

Figure 2.9: SEM image of a MnS inclusion as a source for crack propagation after electrochemical charging of a API 5L X70 steel. Adapted from [42].

To produce X60 to X70 SS steels, two methods were used. One is the addition of niobium and vanadium to the steel. These elements will not produce inclusions in the production, but rather go into solid solution, providing solid solution hardening while not deteriorating HIC performance. The other method is adding titanium to the steel and increasing the niobium content. Titanium binds nitrogen in the steel at high temperatures, so that niobium carbonitrides cannot be formed upon cooling.

Mostafijur Rahman et al. compared the HIC behaviour of X60, X60 SS and X70 steels [57].The X60 SS steel had a lower Mn content. Ca was added to the alloy instead, to form CaS inclusions instead of MnS, which are of a rounder shape and are thus considered less harmful for the steel. However, in tensile testing, the authors found that the X60 SS steel had a higher reduction in ductility than both the X60 and X70 steels. They attribute this to the formation of Ca-Al-O inclusions, which were found along the crack surface in the X60 SS steel. Both Ca and Al were present in the X60 SS steel in higher amounts than in the other alloys. This means that not only MnS, but non-metallic inclusions in general are an initiator of HIC cracks. These findings are supported in a study by Mohtadi-Bonab et al. from 2016 where they study X60 SS as well [43]. They find that the steel is not susceptible to HIC when not applying stress, but is considerably embrittled by the presence of hydrogen when stress is applied. This means that not just the hydrogen content is a measure for the extent of hydrogen embrittlement, but miscrostructural paremeters and stress states also contribute to specific material behaviours in a hydrogen environment. Park et al. also showed, for example, that even though the AF phase had a higher hydrogen solubility, it's susceptibility to HIC was lesser than that of the martensitic phases, because of the inherent toughness of the AF phase that causes crack arrest [55].

Lastly, it should be noted that all of the studies discussed above loaded their steel using electrochemical charging methods. This means that a higher hydrogen content is usually present here than is found in gas charging. Consequently, the amount of embrittlement or HIC will depend on the charging environment. Jin et al., for example, calculated that for Al-O oxides in an X100 steel, a hydrogen threshold concentration of $3.24\,\mathrm{ppm}$ is necesarry to induce HIC cracking and blistering in the absence of stress [27]. This is much lower than what would be reached under gas charging conditions, which is well below $1\,\mathrm{ppm}$ [78].

2.3.2. Mechanical response

In the previous section, different microstructural factors were discussed in relation to their hydrogen absorption characteristics and the extent of their embrittlement. In this section, the knowledge of what effects different microstructures have will be translated to the mechanical response of the steels.

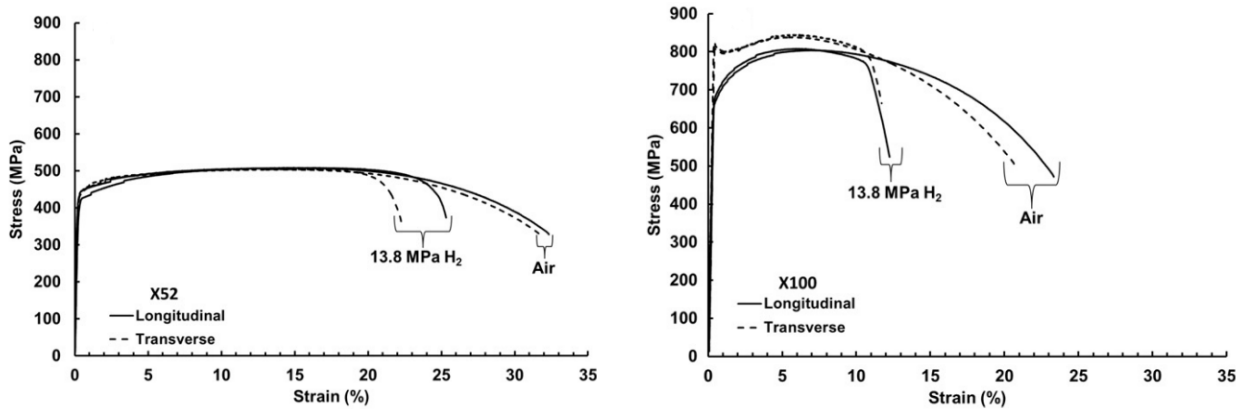

(a) (b)

Figure 2.10: The tensile responses of a) API 5L X52 and b) X100 steel under inert and hydrogen gas environments. The strain rate used was $7 \times 10^{-3}\,s^{-1}$. The longitudinal and transverse directions are relative to the length of the pipe. Adapted from [46].

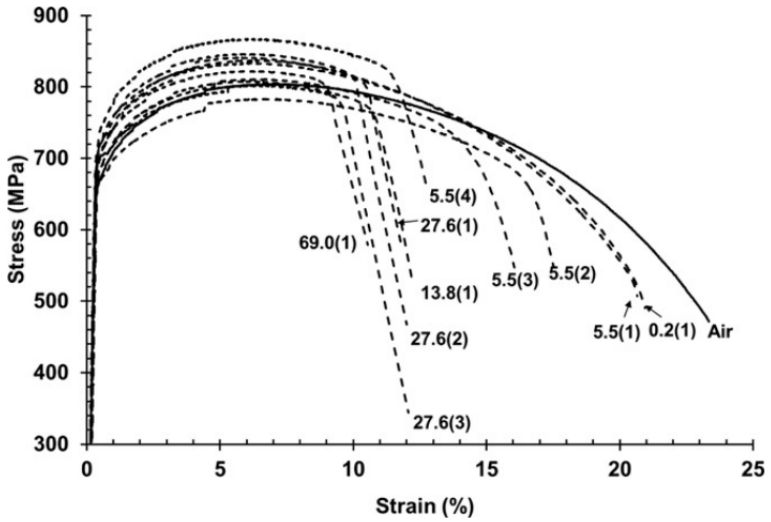

Figure 2.11: Tensile curves of an X100 steel in different hydrogen gas pressures. The strain rate used was $7 \times 10^{-3}\,s^{-1}$, numbers in between parentheses represent different repeated specimens. Taken from [46].

Effect of the microstructure and hydrogen pressure

A study by Nanninga et al. compared three pipeline steels (API X52, X65 and X100) under inert and gaseous hydrogen environments [46]. Because they test pipeline steels with varying microstructures and mechanical characteristics, general characteristics of hydrogen embrittlement effects can be seen in this study. Tensile curves of the X52 and X100 steels under both inert and hydrogen environments are shown in Figure 2.10. What immediately becomes apparent from these curves is the smaller strain at failure of both steel types. This is, unsurprisingly, what hydrogen embrittlement gained its name from. Behaviour in the elastic region, and the plastic region before failure is almost identical to that in an inert environment, but the total elongation until failure is reduced. This is explained by the rapid crack growth in steels as a consequence of the presence of hydrogen. The more hydrogen is present, the quicker microcracks will propagate, and the quicker the sample will fail. The reduction in elongation at failure is accompanied by a lower reduction in fracture area compared to specimens tested in inert environments. The response of an X100 steel to different gas pressures is given in Figure 2.11 the large deviation in results for pressures of 5.5 and 27.6 MPa is explained to happen because of differences in surface finish and partial pressures of water in the test chamber. The relationship between increasing pressure, and decreasing ductility can be seen very clearly in this figure.

Another observation that can be made from this study is that neither the yield strength nor the ultimate tensile strength (UTS) are affected by the hydrogen environment. However, this is not unanimously agreed upon in literature, since many papers do report an influence on yield strength and UTS. Mohtadi-Bonab et al., who tested X60 SS steel under electrochemical charging, find that the material fails in a brittle way without even reaching the yield point [43]. Olden et al. report a fracture stress of a simulated HAZ from X70 steel under constant loading in electrochemical charging conditions that is only $35\,\%$ of the yield stress [50]. In contrast, Pussegoda and Tyson report a slight increase in $0.2\,\%$ proof stress for a quenched low carbon steel [56]. Because the HELP mechanism creates a lower energy requirement for dislocation movement, reduction of the yield stress seems a more understandable consequence of hydrogen presence rather than increase.

The general trend is that steels with a higher strength undergo more severe deterioration due to hydrogen because they often have a higher density of grain boundaries, dislocations and inclusions that all act as strengthening mechanisms as well as hydrogen traps. The hydrogen in the material will firstly influence the ductility until plastic deformation is inhibited completely. If hydrogen concentrations are increased even further, the strength at break will decrease below the yield strength.

Effect of stress concentrations

In the previous section, it was shown that most pipeline steels lose ductility under influence of hydrogen, but do not undergo significant reduction of other properties, except when hydrogen concentrations are very large. However, in presence of localised stresses and strains, the material response can be very different. Wang, Akiyama and Tsuzaki study high strength steels in slow strain rate tensile tests [73]. They test smooth samples, and ones with two different stress concentrations induced by circumferentially notching a round specimen. Because they test a high strength steel, the effects of hydrogen are larger than in pipeline steels. However, even though they find a 60% reduction in fracture stress for smooth samples, they find a 80% decrease in notched tensile strength (NTS) for similar charging conditions under influence of a stress concentration. The decrease in NTS was measured relative to a sample with a similar notch tested in air. They test samples until failure, and recognise an area close to the notch root, where a crack initiated in a brittle intergranular fashion, pointing to high hydrogen concentrations. Further from the crack initiation area, fracture modes became more ductile, ending in ductile shear lips near the edge of the sample. They even identified these brittle crack initiation sites when the diffusible hydrogen content was as low as 0.05 wppm.

Similar experiments on pipeline steels were done by Briottet et al., and Song et al. on X80 and X70 pipeline steels respectively [8, 63]. Briottet et al. report a reduction of tensile strength in a notch sample when charging with $300\,\mathrm{bar}$ of H_2 gas, but the values they report are questionable for the type of steel they used. Song et al. provide more detailed information on the test they perform. Some of their results are shown in Figure 2.12. The reduction of NTS in relation to specimens tested in helium gas is explained to happen because of the hydrostatic and tri-axial stresses that exist inside the notch root. These stresses will dilate the lattice, so that more hydrogen will penetrate this region and cause a more significant loss of mechanical properties. This effect is exaggerated at zones of higher stress tri-axiality. This also relates to the plastic zone at crack tips, which will be discussed further in the next section. Another explanation dislocations to form, allowing for more hydrogen to be stored in this region, as also explained by the authors. This connects to the HESIV mechanism of embrittlement as well.

Effect of the strain rate

What can also be seen in these graphs is a definite dependence of the NTS on the crosshead displacement speed. Another study by Wang, Akiyama and Tsuzaki researches the effect of crosshead speed or strain rate on notched AISI 4135 steel samples [72]. They modelled the local hydrogen concentrations ahead of the notch at a stress of 0.9 times the break stress of the samples that were tested, as shown in Figure 2.13. They conclude that the crosshead speed has a definite influence on the hydrogen concentration, because lower speeds allow for more continuous diffusion towards the stress concentration zone. This is, however, in contrast to the reduction in NTS loss for X70 steel at very low crosshead speeds in Figure 2.12. The difference between these two remains unexplained.

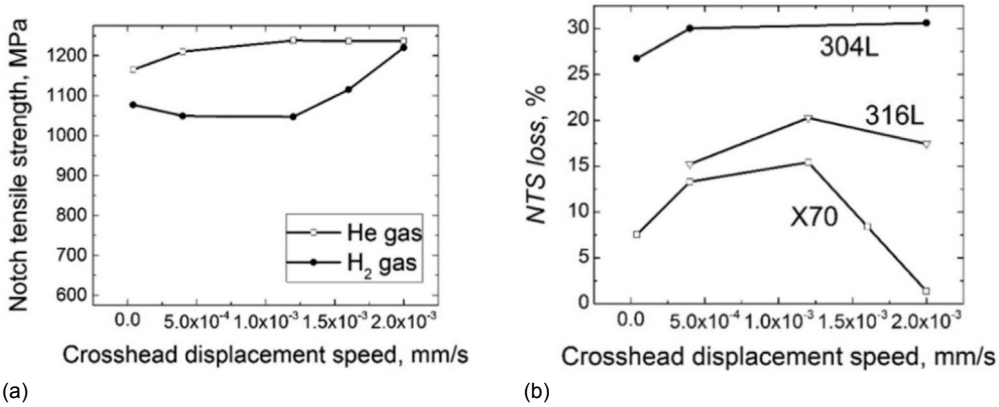

Figure 2.12: a) Notched tensile strength versus crosshead speed in X70 steel, and b) loss in NTS versus crosshead speed in X70 steel. All samples were tested in 10 MPa of H_2 gas. Adapted from [63].

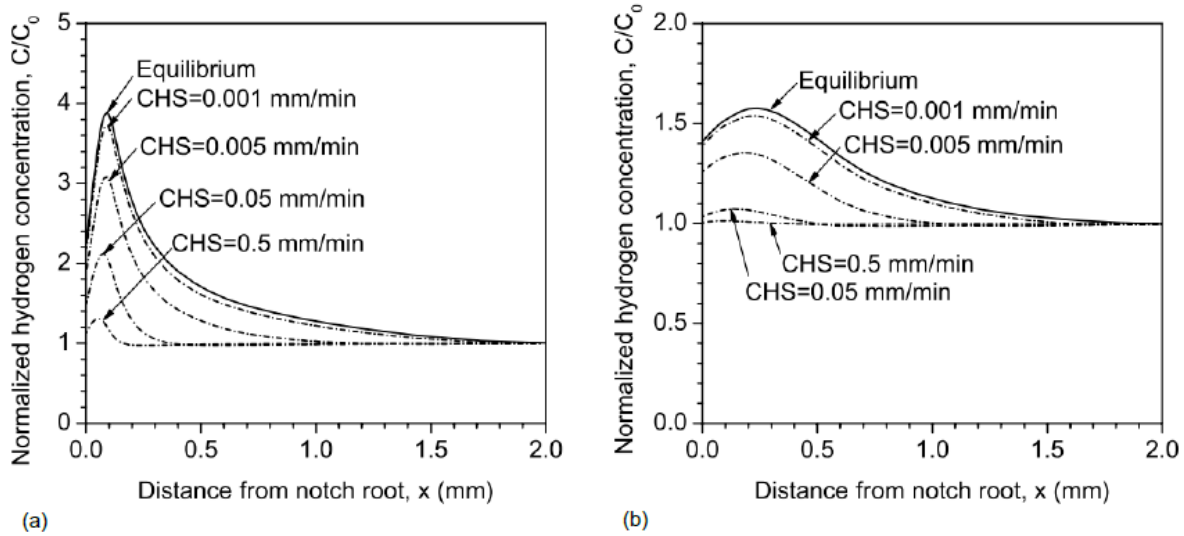

Figure 2.13: The influence of crosshead speed on the local hydrogen concentration ahead of the notch, as studied by Wang, Akiyama and Tsuzaki at 0.9 times the break stress of the sample [72]. (a) was calculated for $K_t = 4.9$ and (b) for $K_t = 2.1$.

Moro et al. study the effects of strain rate on an X80 pipeline steel. Their results are shown in Figure 2.14. The effects on the extent of hydrogen embrittlement of a lower strain rate look visually similar to those of an increased hydrogen concentration in the steel during testing in Figure 2.11. The strain to failure at higher strain rates in hydrogen is similar to that in nitrogen, but at lower strain rate values, elongation starts decreasing significantly in a hydrogen atmosphere. Similar results were also obtained for X100 steel by Nanninga et al., who explain that since loss of ductility is related to crack propagation mechanisms, an equilibrium hydrogen concentration cannot be achieved when the mechanisms for crack propagation are faster than mechanisms for hydrogen absorption [46]. At high strain rates, the crack might move faster than hydrogen can diffuse towards it, leading to a reduced embrittlement effect. When the strain rate is low enough, equilibrium conditions should be reached. This will be elaborated upon further in the following sections.

Effect of the charging method

Zhao et al. charged the same steel using both electrochemical and gaseous methods [78]. They then measured the hydrogen content using Thermal Desorption Spectroscopy. Their results are shown in Figure 2.15. They find that using different charging techniques results in substantial differences in hydrogen concentrations in the steel. In the figure, the graph C_E is the result obtained by electrochemical

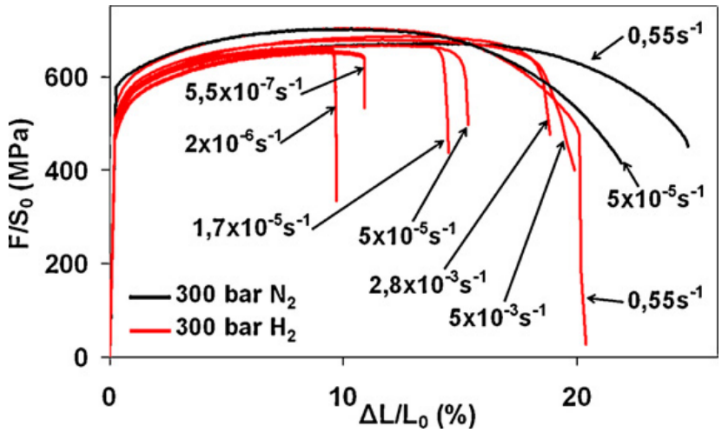

Figure 2.14: Tensile curve of X80 steel at different strain rates. The black curves are control tests with a nitrogen environment instead of hydrogen. Taken from [44].

charging. There is a big peak at lower temperatures which can be assigned to the concentration of diffusible hydrogen. A smaller peak arises at higher temperatures that signifies the concentration of hydrogen trapped in deeper traps. The curve C_G is the result obtained by gaseous charging. The diffusible hydrogen peak has completely disappeared from this curve, whereas there is only a small amount of trapped hydrogen. The total amounts of measured hydrogen were 3.94 wppm for electrochemical charging and 0.24 wppm for gaseous charging. The type of charging that is used therefore has a very big effect on the amount of hydrogen that will be present in the steel and a charging type should be chosen accordingly depending on the environment that is to be modelled.

2.4. Test methods for HE

This section discusses different types of test methods that are used to assess a material's susceptibility to hydrogen embrittlement. Some standardised test methods will be discussed, as well as other test setups that were discovered in the literature.

2.4.1. Differences in hydrogen charging

In Section 2.2.1, the differences between hydrogen absorption from a gaseous phase, or from an aqueous phase were discussed. In this section, the various ways that have been used in literature to obtain these conditions will be dealt with.

Electrochemical methods

Although involving a more complicated process of absorption than gaseous charging, electrochemical charging of hydrogen into steels is easier to perform since it does not require high pressure hydrogen gas, which can be a safety risk. Therefore, many of the studies that have been done to characterise hydrogen embrittlement behaviour, charge steel samples through electrochemical methods [10, 16, 50, 55, 65, 77, 78]. Setups in these studies use the sample as the working electrode, often paired with a platinum counter electrode. They charge the sample either potentiostatically or galvanostatically, meaning that the sample is charged at a constant potential or constant current density, respectively. Either of these methods can yield similar hydrogen concentrations, depending on the calibration and the electrolyte used.

A major advantage of electrochemical charging methods is that by controlling the amount of electrons that are transferred trough the sample, the surface conditions can be controlled quite accurately. By increasing the applied potential or current density, the rate of surface evolution will increase.

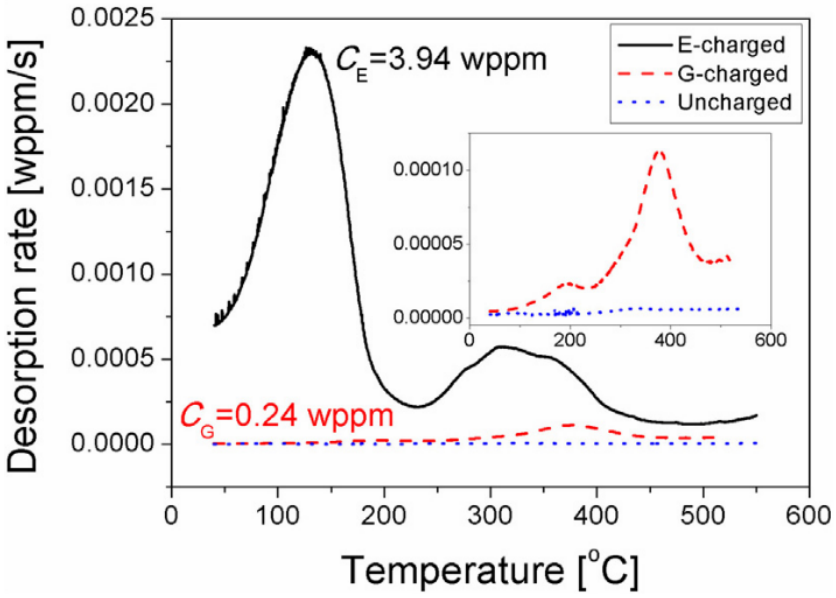

Figure 2.15: A TDS curve as obtained by Zhao et al. [78]. C_E is a curve obtained from an electrochemically charged specimen, whereas C_G was obtained from a gas charged specimen. The baseline dotted curve was obtained as a reference from an uncharged sample.

However, there is a major pitfall to this method. Because the electron transfer in the charging setup only governs the reduction of hydrogen ions to adsorbed hydrogen atoms, as in Equation 2.4, it does not intrinsically say anything about the amount of absorbed hydrogen. This is because the equilibrium of Equation 2.1, the recombination of two adsorbed hydrogen atoms to gas, still holds. Therefore, an increased potential or current density could lead to more gas production instead of hydrogen absorption. To counter this, and promote hydrogen absorption, a so-called recombination poison is often added to the electrolyte that inhibits recombination into gas. As_2O_3 used to be a popular recombination poison, but because of safety issues, thiourea, an organic compound, is now often used. However, even when applying recombination poison, gas formation will happen at high potentials or current densities. This problem is also why measuring the hydrogen concentration when charging electrochemically is difficult.

Gaseous methods

Gas charging of samples is done in just a single way, namely exposing the sample to a high pressure hydrogen gas environment. The surface conditions in the sample are dependent on the gas pressure, which will eventually determine the equilibrium condition in the steel. Some studies perform the charging at ambient temperature, whereas others perform at elevated temperature, to speed up the diffusion process and reach equilibrium conditions quicker [1, 78].

In-situ charging

Since reversibly trapped hydrogen, or diffusible hydrogen, can desorb from steels at room temperature, the time between charging of a sample and testing becomes important. The longer a sample stays out of the charging environment, the lower the hydrogen concentration will become. Wang et al. chose to coat their externally charged samples with a thin layer of cadmium to stop diffusion of hydrogen out from their samples during slow strain rate testing in order to circumvent this problem [73]. However, especially for slow strain rate tests of long duration, it is expected that the cadmium coating cracks with increasing elongation, once again allowing hydrogen to diffuse out of the sample. Moreover, fracture surfaces that are created during the test will not be coated, creating a significant area for hydrogen desorption. Another popular method is to store the charged samples in liquid nitrogen before testing, but this does not solve the problem of desorption during the test, or during warming to test temperature, either.

Instead, some authors use in-situ charging devices to maintain charging conditions during testing [17, 46, 76]. For in-situ gas charging setups, it is not clear whether the environment was contained around just the sample, or around the whole test setup. Either way, the pressure vessel must have some entryway for cables or the moving parts of the tensile device. This brings with it complications when constructing the setup, and safety concerns. This is why many studies that perform in-situ charging tests choose for electrochemical charging methods instead.

2.4.2. Standardised methods

Several methods exist that are widely used to either qualitatively or quantitatively determine the susceptibility of a steel to hydrogen embrittlement. A well developed test to quantitatively determine hydrogen susceptibility is described in ASTM F1624, called the incremental step loading technique [4]. In this test, a specimen is loaded in four point bending, where the load is increased in set increments. Each increment is held for long enough that a hydrogen concentration equilibrium is reached. If the displacement does not change for the given load, the load is increased to the next increment. If the displacement changes for a constant load, this signifies the onset of fracture. With this method, depending on the size of load steps, a threshold value for the stress for onset of fracture can be relatively accurately determined. However, since the concentration of hydrogen throughout the specimen has to be homogenised every step, the tests can take a very long time. This method can be used in combination with either ex-situ or in-situ electrochemical hydrogen charging.

Another, more qualitative method is a disk rupture test, in which a disk of the material to be tested is loaded with a high pressure gas at one side, while leaving the other side open to rupture. Rupture disks are used in industry as fail safes for high pressure equipment, because they can be engineered to burst at a specific pressure [26]. If the high pressure gas is hydrogen gas, the material will embrittle over time, changing the rupture characteristics. Because of the characteristics of hydrogen embrittlement, it will rupture earlier under influence of hydrogen gas. The ratio of rupture pressure in normal gas to rupture pressure in hydrogen gas is an indication of the susceptibility of the material to hydrogen embrittlement.

Lastly, a slow strain rate tensile method for evaluation of resistance against environmentally assisted cracking is described in ASTM G129 [2]. It is performed in a damaging environment, like a hydrogen gas environment. In this test, a smooth or notched specimen is subjected to a slowly increasing extension, until fracture. Afterwards, the fracture behaviour of a sample is compared to a sample that was tested in an inert environment. For smooth specimens, changes in ductility or time to failure are indicators, for notched specimens it can be notched tensile strength. The fracture surface is also examined for changes in fracture behaviour. The strain rate of this test can be adjusted to be slow enough to allow for hydrogen diffusion throughout the sample to guarantee a homogeneous concentration profile. Since this is a continuous displacement test, it can be performed faster than the incremental load test, but it will not give the same type of information about crack initiation. It can give more information about the type of fracture mechanism that the sample underwent in the environment.

2.4.3. Methods from literature

A good overview of an in-situ charging setup is given in Withagen's Master Thesis, which involved constructing such a setup [76]. It is shown in Figure 2.16. By creating a bath of electrolyte around one of the tensile arms, the electrolyte moves with the sample, therefore allowing for continuous charging throughout the test. Although this setup is also quite complicated, because individual elements need to either be isolated from the electrolyte or connected to the charging current, safety hazards are removed if a safe electrolyte is used. By maintaining a constant potential during the test, Withagen manages to obtain an equilibrium hydrogen concentration throughout the test. If calibrated correctly, a similar setup could provide similar hydrogen concentrations to certain gas environments.

A different method of electrochemical hydrogen charging is called Cyclic Voltammetry (CV). This was used at TU Delft by Uluc to investigate hydrogen sorption of Pd-alloys and steels [71]. In cyclic voltammetry, it is not a constant potential or current density that is used to charge the sample, but

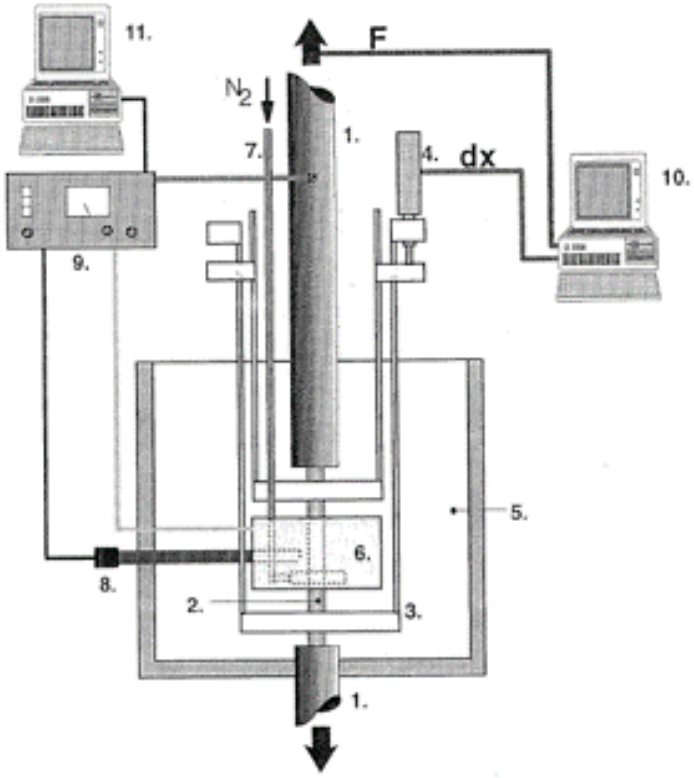

Figure 2.16: Overview of Withagen's in-situ electrochemical charging setup. The different numbers stand for the tensile tester (1), sample (2), extensometer clamp (3), extensometer (4), electrolyte (5), Pt counter electrode (6), nitrogen supply (7), reference electrode (8), potentiostat (9), tensile data acquisition (10) and charging data acquisition (11). Taken from [76].

rather a potential sweep is done over a predefined range. Usually, a sweep is performed from the most cathodic voltage at which hydrogen is evolved (around $-1.2\,\mathrm{V}$) to $0\,\mathrm{V}$. A CV sweep only takes minutes, after which different reactions can be identified. Characteristic for a CV curve is that both hydrogen absorption and desorption are shown, and can be compared. Uluc compares different CV curves, ones before and after prolonged potentiostatic charging, to identify a difference in hydrogen desorption, relating to a hydrogen concentration. Even though accurate hydrogen concentration measurements with this method are hard due to the recombination reaction, qualitative differences in desorbed hydrogen can easily be identified using this method. Moreover, oxide layers can form depending on the metal that is used, which can trap hydrogen as well. This method is shown in Figure 2.17. Both the CV and charging steps can be performed in the same setup, without having to remove the sample.

Nanninga et al. used an in-situ gaseous charging setup to measure the tensile response of X52, X65 and X100 steels [46]. They fit a stainless steel pressure vessel around the tensile specimens to be able to test at high pressures. The specimens were connected by means of a pull-rod that was attached through the wall of the pressure vessel by means of a sliding seal. In order to accurately measure the strain and force, both a strain gauge and the load cell were placed inside the pressure vessel, which were both designed to be able to perform under high pressure hydrogen gas. This type of test setup is the most widely used one in the literature.

In order to test the influence of hydrogen on a notched pipe, Capelle et al. tested an X52 pipe with a diameter of $219\,\mathrm{mm}$ with internal pressures of a hydrogen/natural gas mixture [10]. They machined both internal and external notches in the pipe and subjected it first to a constant pressure for a long time period, before increasing the pressure until the pipe burst. In order to conduct this experiment safely, they used both internal and external cylinders around the pipe to minimise the gas volume and protect against explosions. Furthermore, they filled both internal and external cylinders with argon to reduce combustion risk and conducted the entire experiment in a specially equipped laboratory.

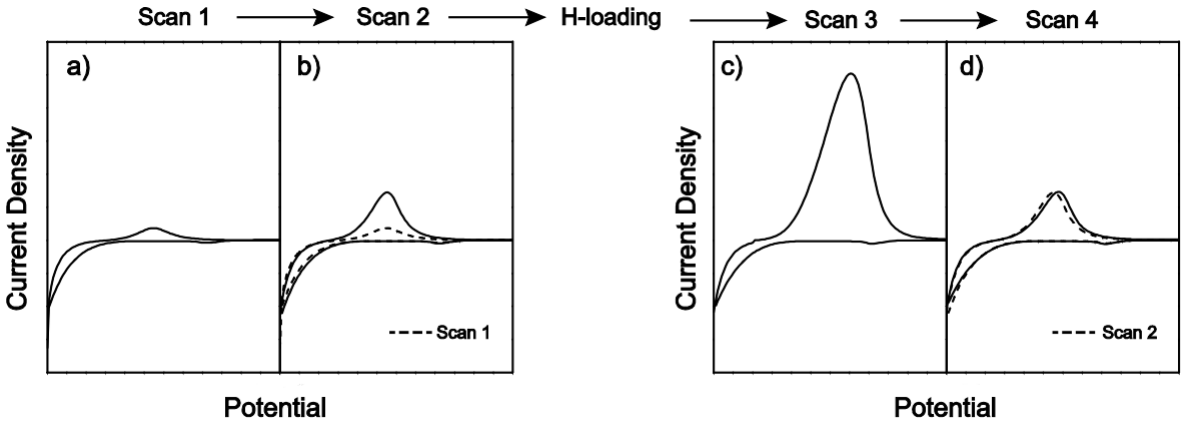

Figure 2.17: Several cyclic voltammetry (CV) curves before and after hydrogen charging. a) is a cleaning step to clean oxidation layers, b) is the first CV sweep, c) is a first sweep after hydrogen charging and d) is a last reference sweep. A big desorption difference can be seen between curves b) and c) that is related to the hydrogen charging. Taken from [71].

2.5. Conclusions and research objectives

After discussing the literature relevant to the topic of hydrogen embrittlement in pipeline steels, conclusions can be drawn from the review. This section will outline those conclusions, and derive some research objectives from them that this thesis will aim to complete.

In summary, this review has discussed that hydrogen can enter steels in several ways during steelmaking as well as operating conditions. Through several mechanisms, the dissolved hydrogen can embrittle the metal, reducing its ductility and possibly its strength. This is called Hydrogen Embrittlement (HE). The fracture mechanisms related to HE are fundamentally plastic in nature, contrary to the embrittlement that is observed in the material. Hydrogen diffuses towards regions of high stress triaxiality like notches and regions in front of crack tips where it causes extra deterioration of mechanical properties. How much a steel is susceptible to HE is determined by its microstructure as well as the amount and shape of defects in the lattice like non-metallic inclusions. Several standard tests are used to characterise HE susceptibility and more are used in the literature. The charging conditions during testing are of high importance to provide a hydrogen environment that is representative of operating conditions, especially for pipeline steels since they are in continuous contact with hydrogen gas.

2.5.1. Conclusions

- There is an interest from industry to transport gaseous hydrogen through existing sub sea gas pipelines.
- Continued exposure of pipeline steels to a gaseous hydrogen environment will cause an equilibrium concentration of hydrogen dissolved in the steel.
- Hydrogen dissolved in a steel will get caught in reversible or irreversible traps and embrittle the steel by several mechanisms, namely HEDE/HID, HELP, AIDE, HESIV and possibly HIC.
- Different regions of the pipeline, like weld regions, will have different behaviour in this hydrogen environment, because of their individual microstructures and alloy compositions. Steels with a more refined microstructure have been shown to be more susceptible to hydrogen embrittlement.
- Ductile steels, like pipeline steels, have been proven to undergo a significant reduction in ductility in presence of hydrogen. Higher hydrogen concentrations will lead to more reduction in ductility and eventually reduction in strength.

- When stress concentrations or zones of tri-axial stresses are present in the material, hydrogen effects will be more pronounced in these regions, because the local equilibrium concentration of hydrogen is higher in these regions.
- The strain rate plays an important role in the severity of embrittlement effects, because higher strain rates will inhibit diffusion of hydrogen to critical zones, whereas strain rates roughly on the order of 10^{-3} and below will allow this, leading to a larger susceptibility to embrittlement.
- Several methods exist for charging steel specimens with hydrogen under different conditions, leading to different hydrogen concentrations. Examples also exist of in-situ charging setups in testing apparatus, allowing for maintaining charging conditions during testing.
- Although in-situ tests have been done on pipeline sections, no setup has been developed that aims to characterise the susceptibility of the weld metal in gaseous charging conditions.

2.5.2. Research objectives

Several questions have not been answered in the literature. Some of these have been chosen as research objectives that this thesis will aim to complete or answer. Specifically, the behaviour of X60 pipeline steel and its welds in a high pressure gaseous environment carries the interest of Intecsea, and has not been sufficiently discussed in literature. Because failure of pipelines has often happened due to hydrogen induced cracking in the weld zone, the behaviour of the weld metal is of special interest. The research objectives that this thesis will aim to complete are:

1. To develop an in-situ gaseous charging setup with the aim of simulating the charging situation in a pipeline for gaseous hydrogen transport.
2. To validate the setup by testing several hydrogen pressures and characterising changes in mechanical performance of the specimens.
3. To identify how these hydrogen pressures will alter the fracture behaviour of the weld metal in presence of a stress concentration and what embrittlement mechanisms dominate fracture.
4. To assess the performance of X60 pipeline steel and its weldment to hydrogen pressures expected to be used in hydrogen pipelines.

2.5.3. Approach

To answer the research objectives, a combined experimental and modelling approach is used in this thesis. An in-situ gaseous charging setup is designed and built to simulate pipeline operating conditions. The sample geometry is designed to mimic a pipe where the girth weld is still present in its original location. The sample features a blunt notch in the weld zone to enforce fracture in the weld metal. FEA models are used both to estimate the necessary time for pre-charging of the samples in hydrogen gas and to gain insight into the stress state that develops in the notch during the test. Knowledge of the stress state in the sample during testing is combined with the tensile results, measurements of the cross-sectional area and SEM fractography to characterise the dominant embrittlement mechanisms and assess the susceptibility of both steels to HE.

3

Materials and Methods

This chapter discusses preparatory work that was done for the tests that were performed for this thesis. Firstly, Section 3.1 contains the details regarding characterisation of the X60 pipeline material. Then, Section 3.2 deals with the design of the test setup, sample and procedures that were designed as part of the thesis work. Lastly, Section 3.3 deals with two finite element models that were created to both support test design and gain further understanding of the stress states in the specimens during the test.

3.1. Material Characterisation

This thesis studies X60 pipeline material that was provided in sections of the circumference of a piece of pipe, including girth welds. This means that two different steels are included in the research. Both need to be characterised because when the characteristics of both are known, their individual responses to a hydrogen environment can be related back to their microstructures. This section contains an explanation of the different characterisation methods that were used, namely compositional identification with X-ray fluorescence and combustion analysis using a LECO machine, micro-structural characterisation using optical microscopy, and hardness measurements made with a micro-hardness tester. A cross-section of the weld area was prepared for microstructural characterisation of the base and weld metals, by sanding and polishing up to a $1\,\mu m$ finish. It was then etched using a 5% nital solution for the different microstructures to become visible with an optical microscope.

3.1.1. Base metal

Composition
The composition of the two metals was determined using two different techniques. Firstly, the different elements present in the metals were analysed with X-ray fluorescence (XRF) scanning. The XRF composition data was combined with that from a LECO composition analyzer which allows for carbon content to be measured as well. The compositions of the base metal is listed in Table 3.1.

Both analysis techniques measured the Sulfur content of the metals. Since both techniques measured similar amounts of S in both metals, the S measurement serves as a cross-verification of both methods. All elements present in the X60 base metal are present in quantities below the maximum levels stated in the API 5L standard, except for Mn [25]. However, since the content of $1.662 \pm 0.060\,\%$ Mn is only slightly above that of the limit of $1.6\,\%$ and within the error limit, this could be a measurement error. Additionally, the standard states that maximum limits can be altered upon agreement between customer and supplier.

Microstructure
The base metal has a largely polygonal ferrite structure with some regions of pearlite. The low carbon content of the steel results in small pearlite regions. This gives rise to the ductile but tough mechanical

Table 3.1: The composition of the base metal, combined from XRF and combustion analysis data.

Element	C	Mn	Si	Cr	Nb	Al	P	S	Rest
% of total mass	0.06	1.66	0.26	0.06	0.04	0.04	<0.01	<0.01	97.88

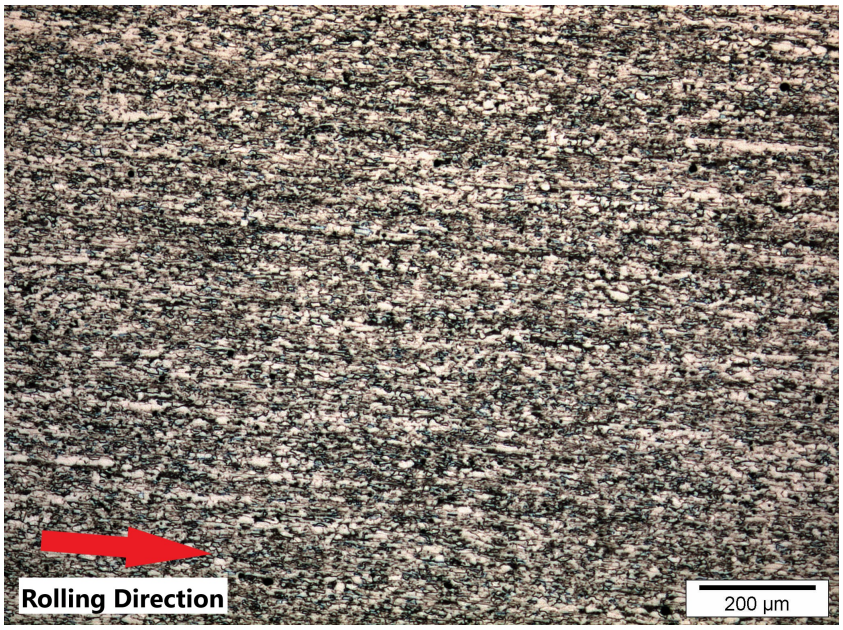

Figure 3.1: A low magnification overview of the base X60 weld metal where segregation bands can be seen.

response of the X60 pipeline steel. At a lower magnification, as shown in Figure 3.1, segregation bands can be seen in the structure that exist parallel to the rolling direction of the steel plate. These originate due to the deformation during the rolling process, where the steel is plastically deformed and spread out in the rolling direction. Figure 3.2 shows two pictures of the microstructure of the X60 metal at a x500 magnification. Grains can be seen to be elongated in the rolling direction, as a direct consequence of the shear forces applied during rolling of the steel plate. Another effect of rolling is grain refinement at the surfaces of the plate, which is where the highest shear forces are present. This grain refinement can be seen in the figure as a difference in grain size between the inside surface in Figure 3.2a and the middle section of the pipe in Figure 3.2b. The inside surface clearly shows smaller grains than the middle section.

3.1.2. Weld metal and HAZ

Weld Macro

An overview of the geometry of the weld is given in Figure 3.3. Because the weld is a girth weld, the pipe's length is in horizontal direction and the top and bottom are the outer and inner surfaces of the pipe wall, respectively. The pipe thickness, width of the weld zone and thickness of the first and last weld passes have been measured using a Keyence digital microscope, which was used to make this figure. The pipe thickness is measured as $15.4\,\mathrm{mm}$ and the weld thickness over most of the pipe wall is $6\,\mathrm{mm}$.

The individual weld passes can be identified from this figure at low magnification. The thickness of the first (bottom) and last (top) weld passes were both measured to be under $2.5\,\mathrm{mm}$. This becomes important when designing a tensile sample, because if these passes are included in the tensile tests, the residual stress or possible plastic deformation will have an effect on the hydrogen diffusion, hydrogen concentration and mechanical characteristics in those regions of the sample. The girth weld in this pipeline was made automatically and is therefore considered as consistent along the circumference of the pipe. Start-stop locations of the weld were identified and are not included in the research.

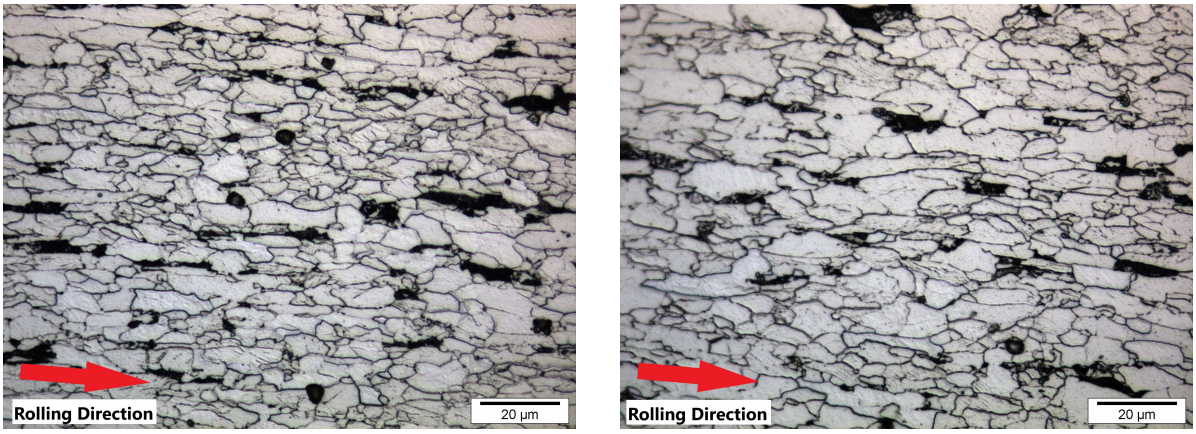

(a) (b)

Figure 3.2: x500 magnifications of microstructures of (a) the inside surface and (b) the middle of the pipe thickness, showing a microstrucure of mainly ferrite (white) with small amounts of pearlite (black). Differences in grain size can be seen as well as elongated grains.

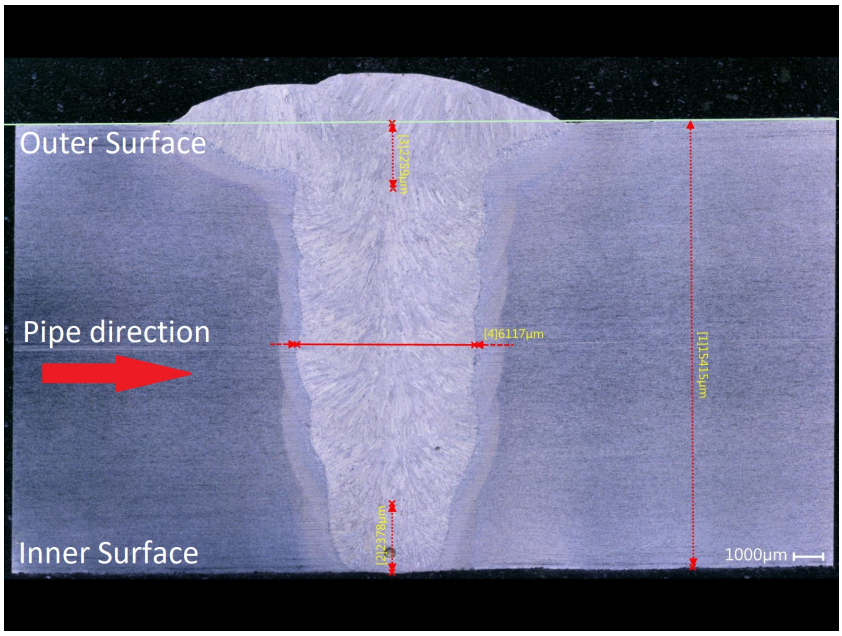

Figure 3.3: Cross section of the girth weld made with a Keyence digital microscope. The pipe thickness is 15.4 mm, the weld width is approximately 6 mm and the distances from the first and last weld passes are both under 2.5 mm.

The region that can be distinguished around the weld metal is the Heat Affected Zone (HAZ). This zone has the composition of the base metal, but due to several heating cycles during the welding procedure the microstructure differs from that of the base metal. Therefore its microstructure and hardness where characterised separately.

Table 3.2: The composition of the weld metal, combined from XRF and combustion analysis data.

Element	C	Mn	Si	Cr	Nb	Al	P	S	Rest
% of total mass	0.07	1.45	0.58	0.05	0.01	0.01	0.01	0.01	97.81

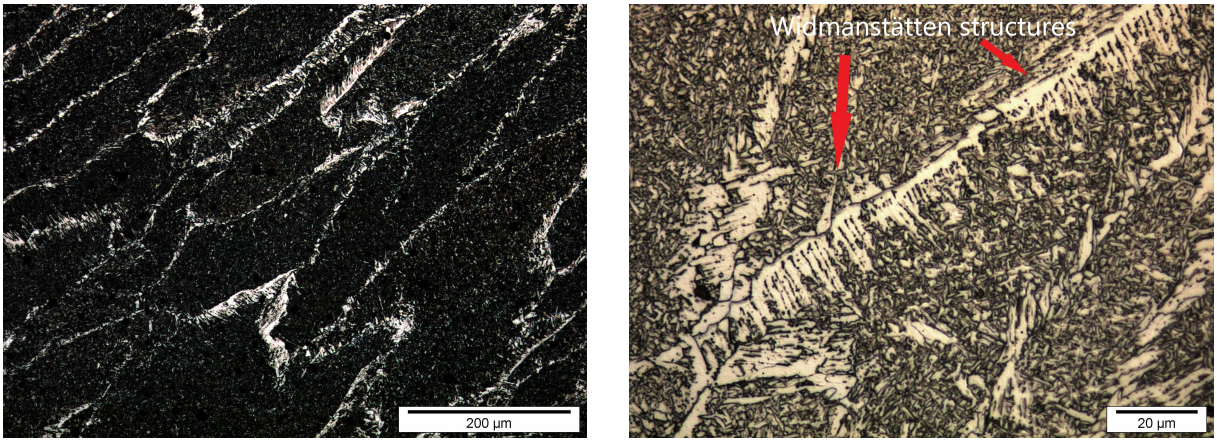

(a) (b)

Figure 3.4: Different magnifications of the WM showing a) a x100 magnification where the columnar prior austenite grains are visible. and b) a x500 magnification that reveals Widmanstätten structures from the prior austenite grain boundaries.

Composition
The composition of the weld metal is listed in Table 3.2.

Microstructure of the weld metal
The weld metal has a very distinct microstructure that can be observed even without magnification after a sample has been etched. This is what is shown in Figure 3.3. With the naked eye, the different weld passes as well as the coarser microstructure can already be distinguished. These coarser grains that can be seen with the naked eye are prior austenite grains that are created when the weld metal starts solidifying after each weld pass. This is shown in Figure 3.4a. These columnar austenite grains grow in direction of solidification of the weld metal. When solidification has occurred and the metal is cooled down further, the metal separates into ferrite and cementite phases. The speed of cooling determines which phases are created. Initially, diffusion of atoms is fast since the temperature is still high, and ferrite starts to be created at the austenite grain boundaries. Then, as the temperature lowers, diffusion of carbon out of the ferrite phase is no longer fast enough for it to grow homogeneously out of the grain boundaries, and so-called Widmanstätten structures start to form. These are columnar needle-like structures where carbon does not diffuse perpendicular to the grain boundary, but parallel to it, causing sharp needles to be formed sticking out of the grain boundary. They are visible in Figure 3.4. Eventually, at even lower temperatures, nucleation of new ferrite grains at inclusions is preferable over growth of existing grain boundary ferrite grains. This is when acicular ferrite starts to appear, which is formed by nucleation at inclusions followed by growth of grains in a similar way to the Widmanstätten structures but in three dimensions. In a two dimensional slice they look like a basket weave pattern. At even lower temperatures, bainite forms. The cooling rate controls the timespan in which each phase is created. In the welds that were tested, both grain boundary ferrite, Widmanstätten ferrite and acicular ferrite is present, which is a typical result of medium cooling rates. The exact cooling rate of the welds is not known.

A high magnification image of the acicular ferrite regions is shown in Figure 3.5. In this figure, the needle-appearance of the acicular ferrite crystals is clearly visible. Also, some spots can be seen that might be inclusions where nucleation of the grains originated.

Microstructure of the HAZ
Figure 3.6 shows the microstructure of the HAZ. It is evident form this picture that many different microstructures are present in this small part of the material. Large grains exist near the weld metal, which transition into the smaller polygonal grains of the base metal as the distance to the weld increases. Because of the several weld passes performed, the HAZ near the weld has been heated up several times, allowing for more recrystallisation and grain growth to happen near the weld zone. Because the HAZ

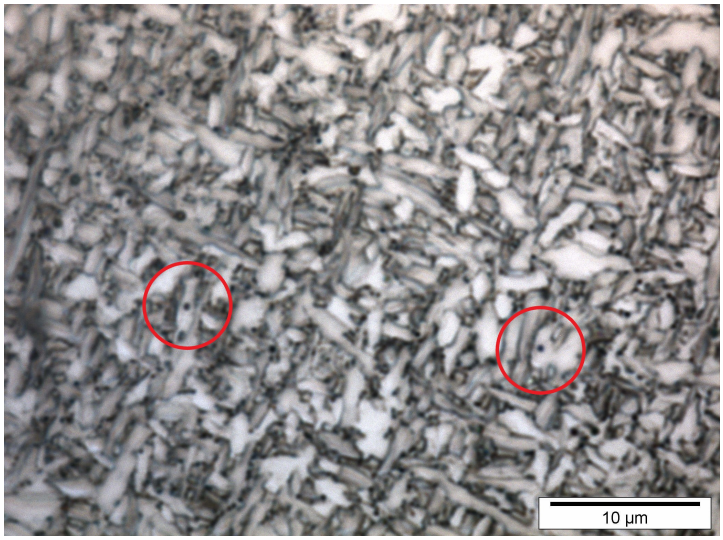

Figure 3.5: x1500 magnification of the acicular ferrite phase in the weld metal showing their needle-like shape. Some features have been circled in red that could be identified as nucleation sites for the grains that grew around it.

was originally base metal, the microstructure transitions to that of the X60 steel near the outside of the heat affected zone. This large variation in microstructure in just a short distance from the weld zone leads to a large change in mechanical behaviour. Because these different microstructures will also behave differently in a hydrogen gas environment, the failure behaviour of the HAZ will be very unpredictable and hard to characterise or relate to a single specific microstructural feature. Since fracture will be localised to the weld zone in this thesis, the behaviour of the HAZ will not be included. Therefore, the performance of the heat affected zone will not be further discussed.

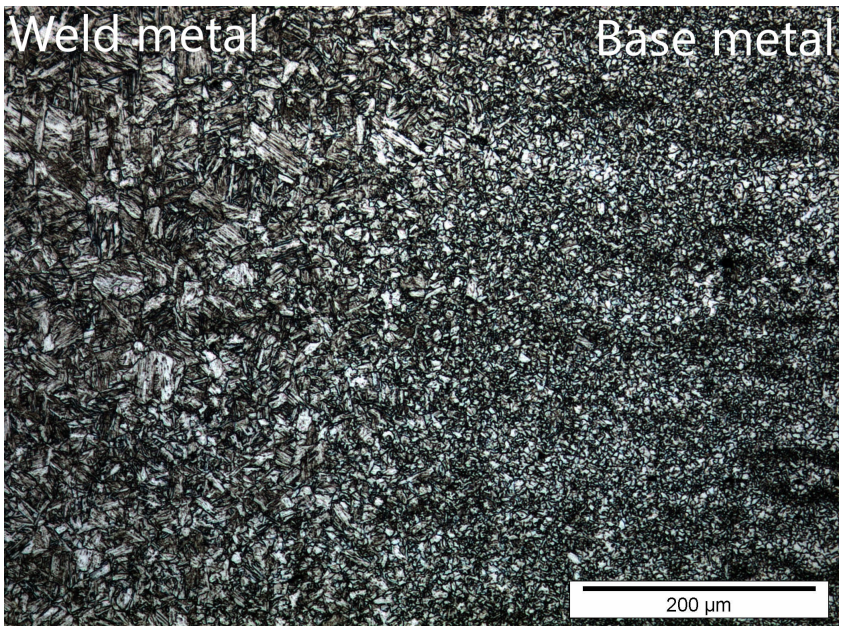

Figure 3.6: An overview of the different microstructures in the HAZ. The weld is to the left side of this area, whereas the right side transitions into the base metal.

Table 3.3: HV1 measurements for the base metal and weld metal. Weld metal averages and standard deviations consist of 24 measurements. Base metal data consist of 19, 21 and 20 measurements for rows 1, 2 and 3, respectively. The HAZ consists of 6 measurements for each row.

	base metal	**weld metal**	**HAZ**
Hardness [HV1]	200.0 ± 3.7	248.0 ± 9.9	225.0 ± 20.5

3.1.3. Mechanical properties

Hardness

To measure the hardness of both metals, a weld section sample was placed under an automatic Vickers micro-hardness testing machine. Three rows of measurements were made, extending through the weld section. Since the applied force was $1\,\mathrm{N}$, Vickers hardness values of the type HV1 were recorded.

The diagonal of each measurement indent was measured to be larger than $85\,\mu\mathrm{m}$, which is significantly larger than the grain size in both steels. Possible differences in measurements because the indent is made on a grain boundary are therefore eliminated. Individual measurements were manually chosen to belong either to the base metal or weld metal. Measurements close to the weld zone that deviated from the base metal measurements were assumed to be measured in the HAZ. Because of the large difference between microstructures in the HAZ, the standard deviation for the hardness values is much higher than that of the other two regions. The hardness of the HAZ can be seen to lie in between that of the BM and WM zones because its microstructure gradually evolves from that of the BM to a higher value as a result of the heat treatment. Hardness measurements for each metal are averaged between the rows of measurements. The higher standard deviation for the weld metal compared to the base metal is a result of the three rows passing through different positions in a weld pass.

Tensile Strength

For the X60 base metal, a requirement for the tensile strength has been set at a minimum of $490\,\mathrm{MPa}$ by the API 5L standard [25]. For the exact weld metal, no data is available. However, a data sheet for an ESAB 70S-6 weld metal described a tensile strength $620\,\mathrm{MPa}$ as welded, which is the same material as was used to create the welds in this pipeline [18].

3.2. Experimental Methods

In order to accurately model the hydrogen environment that would be present inside a hydrogen pipeline, it is important to use a test setup where the charging conditions are similar. The large difference between electrochemical and gaseous charging environments that was discovered in the literature stresses the need for accurately matching charging conditions with practice. To be able to perform tests that are representative of a pipeline under operational conditions it was decided to design a new setup that could test specimens in a gaseous environment. This section outlines the design of this setup, as well as the design of the sample geometry that is tested and the test matrix and procedures.

3.2.1. Setup design

To be able to perform tensile tests in-situ in high pressure hydrogen gas, a Zwick Z100 electromechanical tensile tester was modified with newly designed adapters. By keeping the hydrogen gas under pressure and in contact with the specimen throughout the test, very similar environmental conditions to some actual operating conditions of a hydrogen pipeline can be achieved. Several different preliminary designs were made for the new test setup, which were all evaluated on terms of safety and practicality. The final design features a hollow test sample that is loaded with hydrogen gas from the inside. The sample design is discussion in Section 3.2.2. The sample also acts as the gas containment volume throughout the test. A schematic overview of the final configuration is shown in Appendix A. Figure 3.7 displays a close-up image of the test specimen as placed in the test setup. A detailed description of the test setup including operating instructions for pre-charging and testing is given in Appendix A as well.

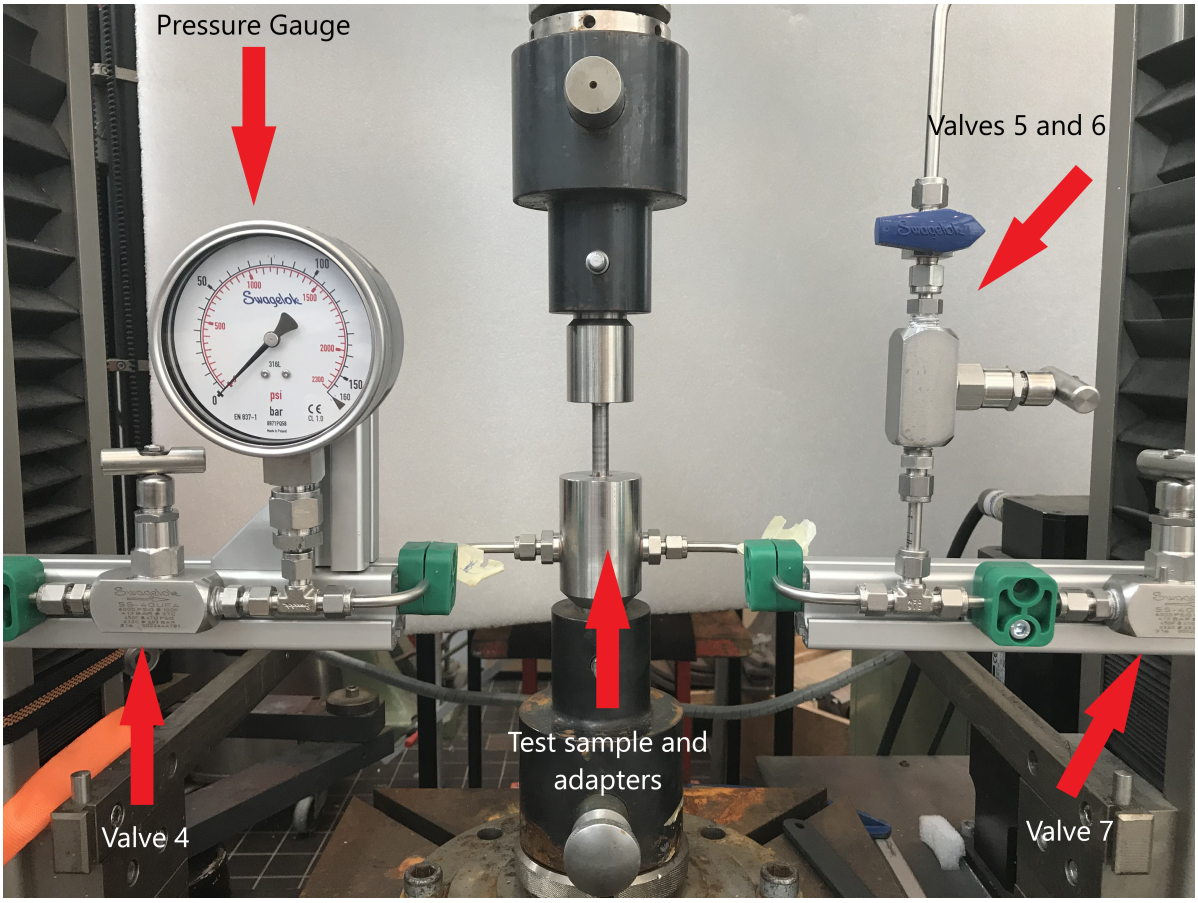

Figure 3.7: An overview of the test setup showing the sample and some peripheral equipment. Details about peripheral equipment are given in Appendix A.

The design is simplified significantly by using the sample as the gas chamber. Using a separate containment volume that encompasses the sample would create complications because the movement of the cross-head needs to be accommodated without causing leakage. These complications are not present in the current design since the containment volume itself extends during the test which eliminates the need for a sliding type sealing. Furthermore, the required volume of hydrogen gas is very low compared to an external gas chamber. However, the complication for this design lies in the fact that the sample has to be tested until fracture, which means that the hydrogen gas will escape from the containment volume. Upon fracture, hydrogen is released and mixes with air, creating a zone where the concentration of hydrogen gas is such that combustion is possible. However, with small volumes of gas, this volume in which hydrogen can be present in combustible amounts is only between 0.5 and 2.5 l large. If ignition sources are not present in this zone, combustion will not occur. Furthermore, because H_2 is so light, it quickly disperses itself in air which dilutes it to non-combustible concentrations. Controlling the volume of hydrogen that escapes upon sample fracture and removing any ignition sources are sufficient safety precautions to safely perform the tensile tests until fracture.
For further safety, a polycarbonate blast shield is placed in front of the setup to protect the operator from any particles that might be propelled away from the setup as a result of the high pressure.

3.2.2. Specimen design

A schematic drawing of the sample geometry is shown below in Figure 3.8. A detailed explanation of the design and a drawing with full specification can be found in Appendix B.

These cylindrical specimens were cut from X60 pipeline material in the orientation that is shown in Figure 3.9. The geometry of the girth weld and its location in the sample is analogous to how it was

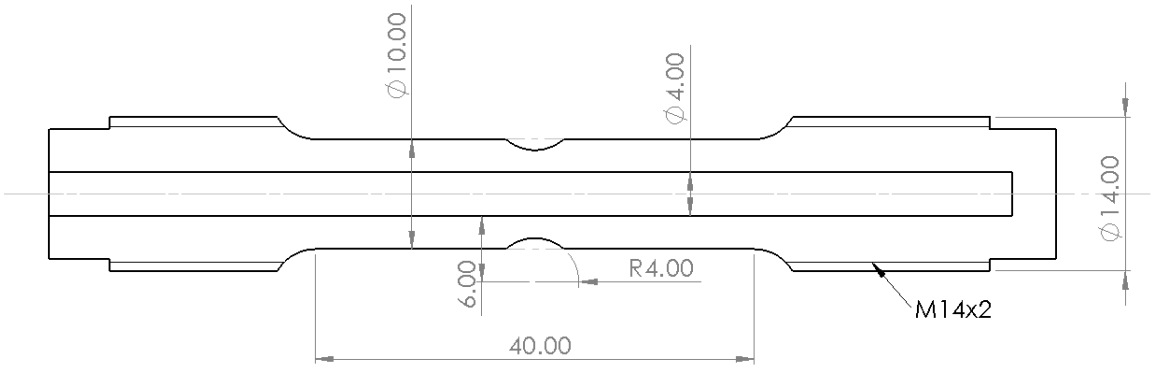

Figure 3.8: A schematic drawing of the sample. The dotted lines in the notch area represent the geometry of the smooth samples. For the drawing with full specifications, see Appendix B.

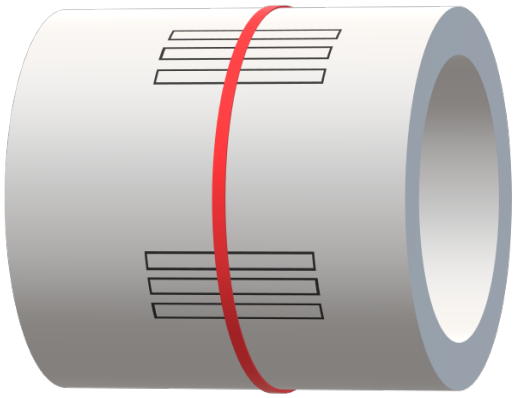

Figure 3.9: An overview of how the samples were machined from the pipe material. The girth weld is shown as a red band, outlines of samples are shown as black rectangles.

present in the pipe. Because of this and the fact that the specimens design is hollow, they can be seen as a pipe including a matching girth weld. The samples include a blind hole that extends across almost the entire specimen length. This hole creates the volume that is pressurised with gas for the tests.

Most samples for this research feature a notch, that has been included because the weld metal over-matches the base metal by roughly 25%, meaning that the tensile strength of the weld metal is 25% higher than that of the base metal [18, 25]. A notch is therefore necessary to enforce fracture in the weld zone.

3.2.3. Test matrix and procedure

The test specimens contain many variables of which the effect is yet unknown such as the notch, the weld metal and the HE behaviour. In order to draw any conclusions from the data gathered for this research, these variables need to be understood. For this reason, different sets of specimens with different characteristics were tested in order to elucidate the effect of each of these variables separately. These different sets have been visualised in a test matrix, which will be discussed in this section. Furthermore, this section will deal with the procedure for testing that was developed for the new setup.

Table 3.4: Test matrix containing the samples that were tested.

Sample	Environment	Subset	Goal
Base metal Smooth	Lab environment 100 bar N_2 100 bar H_2	A1 A2 A3	Material properties Effect of pressure Effect of Hydrogen
Base metal Notched	100 bar N_2 100 bar H_2	B1 B2	Effect of stress concentration Effect of stress concentration and hydrogen
Notched Weld Zone	100 bar N_2 30 bar H_2 70 bar H_2 100 bar H_2	C1 C2 C3 C4	Properties of weld Effect of hydrogen pressure

Test matrix
The test matrix for the tensile tests is depicted in Table 3.4. The table lists different subsets of samples, their specifications and their goals for testing. The variables of different materials, non-linear stress states due to the notch, added stresses due to the internal pressure and hydrogen evolution into the material are considered separately from each other.

The matrix consists of three sets of samples; set A consists of smooth base metal specimens, set B of notched base metal specimens and set C of the specimens containing a notched Weld Zone. All these sets have different subsets that apply different environmental conditions to the test samples. All subsets consist of three samples.

Set A has three subsets. Subset A1 tests the base metal in lab environment conditions. The goal of these sets is to obtain basic mechanical performance of the X60 steel. Subset A2 introduces pressure into the system by loading the samples with 100 bar of internal nitrogen pressure. Subset A3 introduces hydrogen gas instead of nitrogen, to be able to characterise the embrittlement of the X60 base metal. Because of subset A2, the effects of the hydrogen gas pressure and the hydrogen itself can be evaluated separately.

Set B is the first set of samples that contains a notch. The first subset, B1, is tested to observe the difference in mechanical behaviour caused by the notch. Because 100 bar N_2 is used, it can be compared to tests from subset A2. Furthermore, B1 is used as a reference to subset B2 in which the N_2 is substituted by H_2. The tri-axial stress state created by the notch will create different conditions for HE compared to subset A3.

Set C introduces the weld metal into the test. Subset C1 is used as a benchmark, where 100 bar N_2 will be applied throughout the test. This will provide a baseline for the other subsets in set C. Since the geometries of sets B and C are similar, the results from this subset can be compared to B1 to identify the behaviour of the weld metal compared to the base metal. In the remaining subsets C2, C3 and C4, different H_2 pressures are applied to the sample. The expectation for these subsets is that with increasing hydrogen pressure, elongation until failure will decrease. The performance of these samples, as well as their fracture surfaces, will be compared to those of sets A and B to allow an assessment of the susceptibility of the weld metal to HE.

Test procedure
Tests performed on the setup that was designed for this research consist of two main steps; the pre-charging and the test itself. This section discusses the procedures for these in some detail. The step by step operating instructions including leak testing and charging the setup can be found in Appendix A.

Before testing samples in a hydrogen environment, a pre-charging step is essential to allow for the hydrogen to diffuse into the specimen. However, since small amounts of oxygen can inhibit hydrogen absorption significantly, the system is first flushed with nitrogen three times, and evacuated in between. The system is only filled with hydrogen after the system has been evacuated three times. This pressure

is then held overnight for about 17 h. Before placing any specimen in the setup for pre-charging, it is cleaned in an ultrasonic bath in isopropanol for at least 5 min. The weld samples were also sanded on the inside using a brush containing 600 grit SiC particles before ultrasonic cleaning. Then, the gauge length, gauge length diameter and diameter at the notch root are noted down. A safety shield is in place in front of the setup. It can be opened to allow operation of valves close to the sample and the extensometer. It is always closed when access to the sample is not required.

Before starting the test, after pre-charging, a pre-load of 1000 N is approached by the tensile tester to get rid of any play in the system and adapter connections. When the pre-load is reached, an extensometer with a gauge length of 20 mm is applied over the notch, to eliminate any deformation of the load train from the measurement. Once the yield point has been reached and the force is approaching is maximum value, the extensometer is removed. This happened at 2 % strain (as calculated from extensometer data) for the smooth samples and 1 % strain for notched samples. After this point the force does not increase as much as during elastic deformation, and the extension of the sample can be measured using the cross-head displacement more accurately. Furthermore, it eliminates the risk of damaging the extensometer upon fracture of the sample.

The software records several values during the test. The ones that are used are the test time, the applied force, the absolute cross-head displacement and the strain signal. All values are stored once every second during the test. It should be noted that the values for strain are calculated from the extensometer data as long as it is connected, after which the software automatically switches to cross-head displacement data, which it scales to the original extensometer length to maintain continuity in the strain data.

The test speed is set to $1.5\,\mathrm{mm\,h^{-1}}$ in order to give the hydrogen enough time to diffuse throughout the sample even during the test. Fracture is used as the end-of-test criterion, which is set to be considered when the load drops more than 5 % between two measurements. In practice this will mean that fracture happens when the load drops more than 5 % in one second. If this criterion is not reached before the force reaches 20 % of its maximum value during the test, the test is stopped as well.

If a test with hydrogen was performed, the system is flushed with nitrogen before removal of the sample to remove leftover hydrogen.

3.2.4. Data analysis

For the smooth samples tested in this thesis, the extensometer is used to calculate the strain for the first part of the test, proceeded by the cross-head displacement data. This switch can be made because the strain is constant over a smooth specimen. For the notched samples, however, the elongation is used instead of strain, which cannot be accurately calculated for the entire sample just from extensometer data. Therefore, in order to make the data gathered from the notched tests comparable to each other and to the deformation model presented in the next section, a correction is made that transforms the tensile curve to show the stress in the notch region of the samples as a function of the elongation of the entire gauge length.

During the early stages of a notched test, the extensometer is attached over the notch region which also includes a part of the smooth regions outside the notch. This means that the elongation as calculated from the extensometer is not representative of the whole sample. This becomes problematic when the extensometer is removed, since the software considers the sample to be smooth, and calculates the strain accordingly using the cross-head displacement data. This results in inaccurate elongation data for the notched specimens from the software, which means manual correction is needed to generate realistic data.

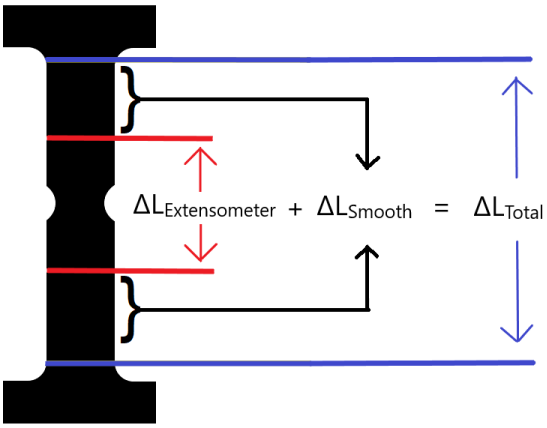

Figure 3.10: The position of the extensometer during the test.

Upon deformation of the entire specimen, the total elongation consists of the extensometer section and the smooth section that makes up the rest of the gauge length, $\Delta L_{\text{Total}} = \Delta L_{\text{Extensometer}} + \Delta L_{\text{Smooth}}$. This is displayed graphically in Figure 3.10.

$\Delta L_{\text{Extensometer}}$ is accurately measured by the extensometer for as long as it is attached. To obtain ΔL_{Total}, the stress level in the smooth part of the specimen is calculated at every measurement point. Then, the elongation of sample A1.1, a smooth base metal sample tested without any gas, is scaled to the remaining length outside of the extensometer span and added to $\Delta L_{\text{Extensometer}}$. This means that $\Delta L_{\text{Total}} = \Delta L_{\text{Extensometer}} + \Delta L_{\text{A1.1}}$. When the elongation of the extensometer span reaches $0.1\,\text{mm}$, the calculation of the elongation is switched to the cross-head displacement like in a normal test. Using this method, the elongation of the entire gauge length is calculated both when the extensometer is still attached and after it has been removed. This correction method has been used for all notched samples in this thesis. For some samples, however, the switch was made before the $0.1\,\text{mm}$ extensometer strain point because unloading happened before this point, which is not compatible with the method. In all samples, force did not increase significantly after switching to the cross-head displacement data, meaning any added elastic deformation of the load train included in this data is minimal.

3.3. Computational Methods

This section discusses two finite element models that were used as support for the setup that was discussed in Chapter 3. Both models were created using Abaqus. A diffusion model is used to determine the duration of the pre-charging phase, another is used to elucidate the state of triaxial stresses that occur in the notch region throughout the test.

3.3.1. Diffusion model for estimation of pre-charging duration

For the tests performed in this research, hydrogen concentrations should be sufficiently uniform throughout the sample thickness to ensure the full effect of hydrogen embrittlement. A pre-charging step is included in the test procedure to assure this equilibrium condition, but it was not experimentally validated. The required pre-charging duration has instead been estimated with an FEA model using the hydrogen diffusion speed throughout the two metals to calculate when an equilibrium is reached.

Material input data

This model uses a axisymmetric elements to construct the gauge length of the cylindrical sample as discussed in Section 3.2.2. The mesh is created with Abaqus' structural mesh option that automatically generates a mesh which fits the section it is being placed in. Especially for slightly curved sections like the notch, this setting is less prone to generating triangular elements than free or direction-based mesh-

ing. This is important because triangular elements are incompatible with quadratic mesh types that are used in the model. The sketch is split up into a base metal and a weld metal section, which have both been assigned specific diffusivities. Mohtadi-Bonab et al. calculated the effective diffusivity D_{eff} of an X60 steel with a similar microstrucure to that used in this research as being $0.81\,\text{mm}^2\,\text{h}^{-1}$ (They use D_{app} in their table but speak only of D_{eff} in the rest of their text)[41]. An ER70S-6 weld metal was tested by Panico et al. to have an effective diffusivity of $1.044\,\text{mm}^2\,\text{h}^{-1}$ [54]. Both these values were tested by electrochemical permeation testing in a modified Devanathan-Stachurski setup. Although the welding parameters for the weld metal tested by Panico et al. are unknown, it is the same weld metal as was used to create the welds used in this research, so their diffusivities are assumed to be similar. The higher value of D_{eff} for the weld metal compared to that of the base metal is expected because the weld metal has a high density of grain boundaries, which act as fast diffusion paths for hydrogen.

Boundary conditions
The inner surface of the model was set to a constant concentration that was calculated with Sievert's law given in Equation 2.3. It was calculated as being $1.722 \times 10^{-11}\,\text{mol}\,\text{mm}^{-3}$ at a temperature of $293\,\text{K}$ and a pressure of $100\,\text{bar}$. An explicit dynamic analysis was run to observe the concentration gradient through time. Before starting the dynamic analysis, the bulk concentration of the sample was set to 0. Desorption at the outer surface was not modelled since it is concentration dependent and a boundary condition that accurately represents it does not exist in Abaqus. Furthermore, the desorption rate is expected to be very low and is countered by the constant influx of hydrogen from the inside area of the sample. The full hydrogen diffusion model as well as a closeup of the notch area are shown in Figure 3.11. The distance between nodes differs throughout the model, between approximately $0.1\,\text{mm}$ in near the notch root and $0.5\,\text{mm}$ in the base metal section. All elements are standard quadratic heat transfer nodes, denoted by the name DCAX8 in Abaqus.

Abaqus uses a form of Fick's equations for mass diffusion with the normalised concentration ϕ as the main variable, which is defined as $\phi = c/s$ where c is the actual concentration and s is the solubility of the material. This is done so that the normalised concentration will be continuous over boundaries between different materials that share nodes. The boundary condition applied to the inside surface is regarded as a normalised concentration by Abaqus. Therefore a solubility value is not used in the calculations for this model. Instead, the solubility is set to 1 for both materials to set the normalised concentration as equal to the actual concentration. The solubility becomes an important factor in diffusion analysis if concentrations approach the solubility limit of the material. However, solubilities for these materials found in the same literature as the diffusivities are a factor 100 higher than the concentrations reached here, so diffusion is not limited by the solubility of either steel. This does mean that this model is valid only for analyses where the concentrations are well below the solubility limit.

The notch root on the outer surface reaches a value of $1.68 \times 10^{-11}\,\text{mol}\,\text{mm}^{-3}$ after $17\,\text{h}$ of charging. This is more than 97% of the original inner surface concentration which is considered sufficiently close to equilibrium conditions to start the test. A concentration over time plot is shown in Figure 3.12. The time of $17\,\text{h}$ has been taken as a maximum because this is the time that samples can pre-charge overnight in between office hours. It can be concluded that pre-charging samples overnight is sufficiently long for them to reach near-equilibrium hydrogen concentrations throughout the notch region.

3.3.2. Deformation model

This section discusses the creation of a plastic deformation model of the sample geometry including the notch. The introduction of a notch in a cylindrical specimen has significant effects. The reduction in cross-sectional area it causes will increase the hoop stress and even though the notch is blunt, it will create a tri-axial stress state that is different from that outside of the notch area. To understand how high the hydrostatic stresses and stress tri-axialities are in the notch, a deformation model is created. The geometry for this model is the same as that of the diffusion model discussed in the previous section. Because both models are created after the sample geometry, their mesh is identical except that in the deformation model, the mesh elements are quadratic deformation elements denoted as CAX8.

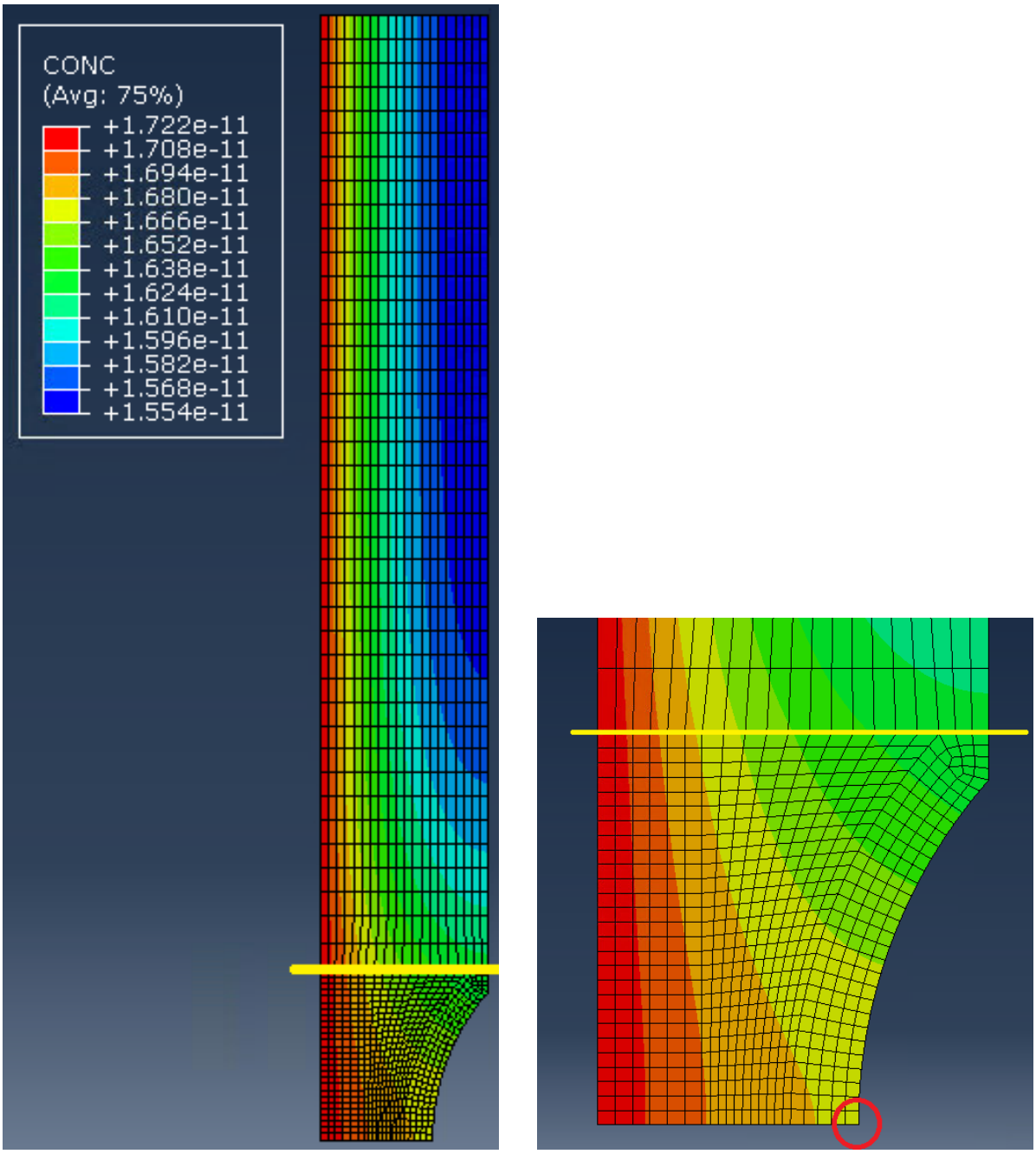

(a) (b)

Figure 3.11: (a The full diffusion model after 17 h of pre-charging which shows the concentration gradient. Units are $\mathrm{mol\,mm^{-3}}$. b) A close-up of the weld zone after 17 h of pre-charging. The red circle indicates the notch root on the outer surface, where the concentration has reached more than 97% of the concentration at the inner surface. In both pictures, the yellow line signifies the separation between weld metal and base metal.

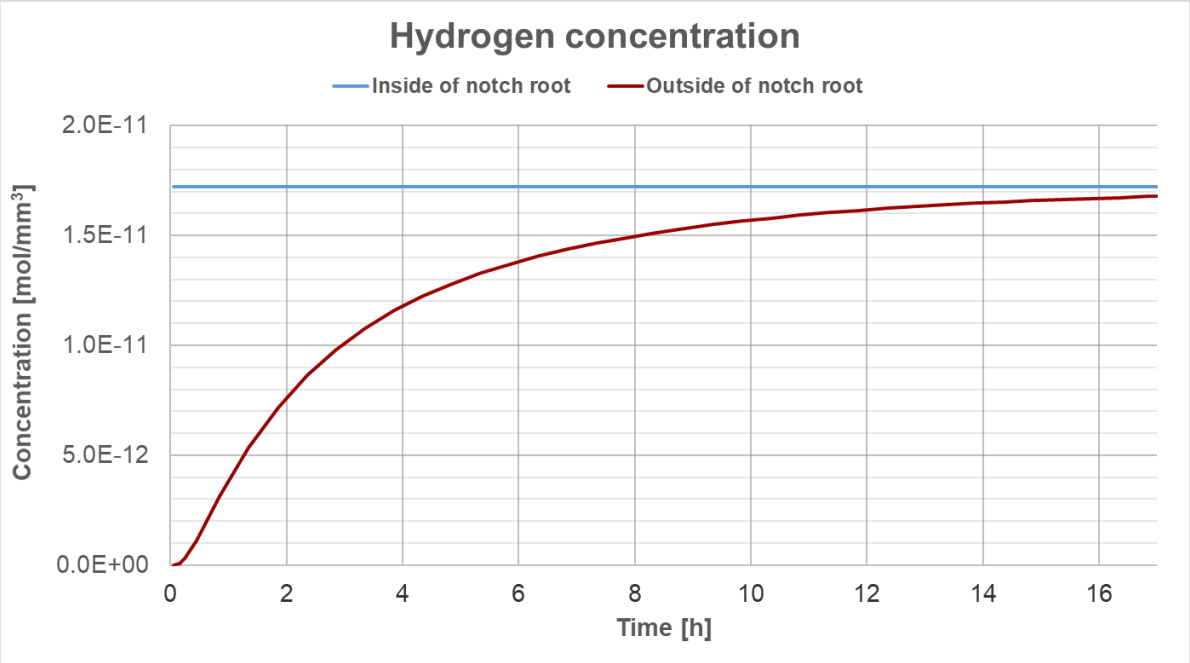

Figure 3.12: A plot of the hydrogen concentrations of the inner and outer surfaces of the notch root over time. After 17 h the outer surface reaches over 97% of the concentration of the inner surface.

Boundary conditions

Two boundary conditions are applied to this model. The first is a symmetric boundary condition on the bottom surface, the second a displacement on the top surface. The displacement is used to model the load applied by the tensile tester, while the symmetric boundary condition acts to create an equal and opposite force on the other side of the sample that is not modelled. A displacement boundary condition is used rather than a load, because small increases in load can result in very large displacements in materials that experience low strain hardening. A small increase in displacement is desirable to be able to isolate single steps in the loading process. An overview of the mesh and boundary conditions is given in Figure 3.13. The calculation process for this model consists of two steps. In the first step, a pressure is applied to the inside surface to model 100 bar of internal nitrogen or hydrogen pressure. To more realistically represent the tensile test, the displacement boundary condition is only applied during the second step. Both the pressure and displacement are applied in increments. Because large deformations are involved in this model, Abaqus has been set up to regard nonlinear geometries, meaning it updates the stiffness matrix after each increment. Stresses, strains and displacements are saved for each node at each increment of the loading step.

3.3.3. Material input data

Unlike the diffusion model, the deformation model only consists of base metal and as such models the samples from set B. Because detailed material data for the specific weldment steel present in the samples are not available and no tests are performed on just the weld metal, extracting material data for the weld metal only is a task outside the scope of this thesis. For the base metal, however, data was gathered that can be used as an input for the model. These data points are shown in Table 3.5. The material input for this model was taken from test A1.1 and shall therefore be discussed in the next chapter after the tensile results have been presented. This data was taken up to the point of the onset of necking of the sample. Abaqus assumes perfect plasticity of a material if no further data is given. This means that in this model, perfect plasticity is assumed after the onset of necking, which is not realistic. The model should therefore only be used until the point where the maximum stress is reached at any point in the model.

Table 3.5: The data points taken from the true stress (s) - true strain (e) curve of sample A1.1 to use as input data for the Abaqus deformation model.

True Plastic Strain e_p	0.00	0.01	0.03	0.05	0.075
True Stress s [MPa]	453	486	530	557	576

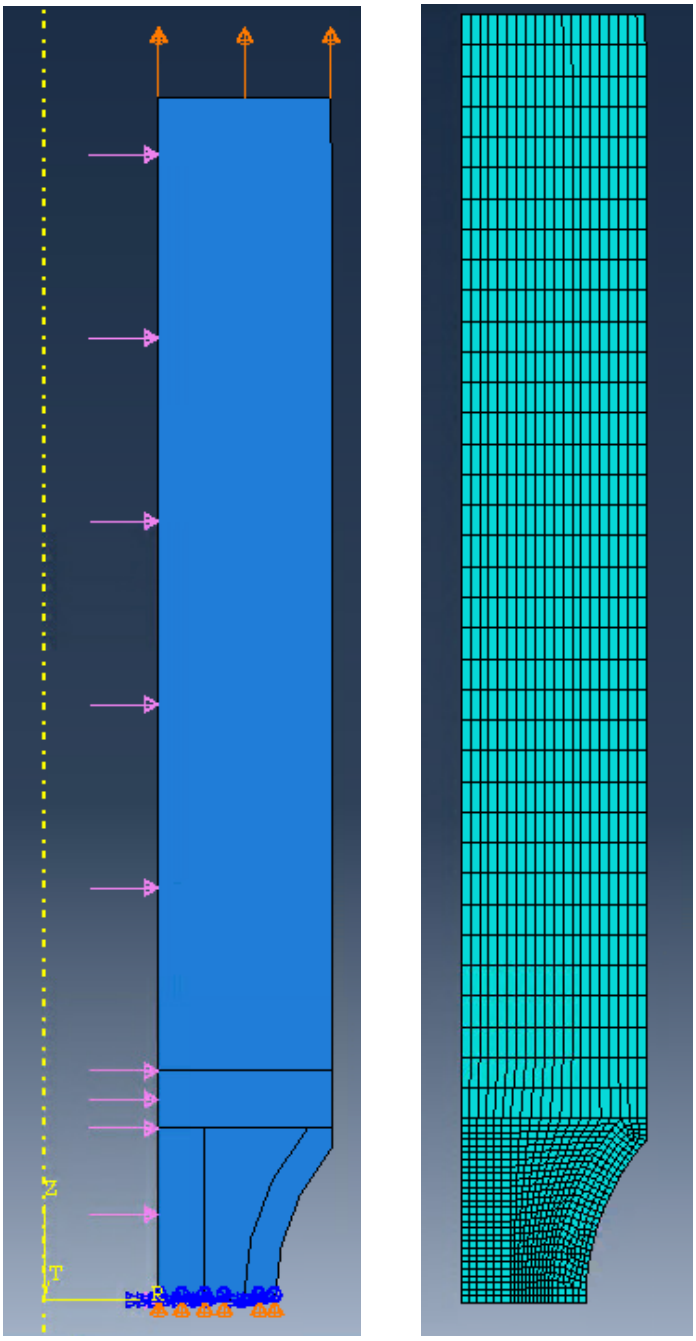

(a) (b)

Figure 3.13: a) The boundary conditions for the Abaqus deformation model. The pink arrows denote the load to model the inside pressure, the orange arrows at the top denote the displacement condition to model the tensile force. The small arrows at the bottom denote the symmetry conditions to transform half the sample that was measured to a whole tensile specimen. b) The mesh that was used in both the diffusion and deformation model.

4

Results and Discussion

This chapter presents the results of the tests that were performed for this thesis. The results of the smooth specimens are presented first, and this data is used to explain the basic effect of hydrogen on the base metal. The results for the notched base metal specimens are discussed afterwards, using the Abaqus deformation model to get an insight into what effect the stress states in the notch have on the behaviour in a hydrogen environment. Next, the results of the weld specimens are presented and the effect of hydrogen on the weld metal is discussed. Lastly, several fractographic observations are presented and are coupled to the mechanical performance of the specimens.

Throughout this chapter, the samples will be frequently referred to by their subset and sample number rather than by their material and test environment. Table 4.1 below lists the different specimen subsets and their defining characteristics for reference. Sample references including an extra number, like A1.1, represent the first repetition of the tests in subset A1.

4.1. Smooth specimens: the effect of hydrogen on the base metal

4.1.1. Tensile results

Smooth base metal specimens were tested as a reference for the notched samples under similar environments. This section discusses the differences between the specimens tested in different environments.

Table 4.1: An overview of the different subsets that were tested in this thesis..

Sample	Environment	Subset
Base Metal Smooth	No Gas 100 bar N_2 100 bar H_2	A1 A2 A3
Base Metal Notched	100 bar N_2 100 bar H_2	B1 B2
Notched Weld Zone	100 bar N_2 30 bar H_2 70 bar H_2 100 bar H_2	C1 C2 C3 C4

Figure 4.1: The three specimens comprising subset A1 of smooth base metal specimens, from 0% to 1% engineering strain.

Deviating yield behaviour

The curves for all specimens from subset A1 are given in Figure 4.1, which is focused on the samples' yield points. As can be seen in the figure, samples A1.1 and A1.3 have a distinct yield point, whereas yielding in sample A1.2 happens much more gradually. This could be explained by considering the way pipelines are formed from steel plates. The two most used methods of plate bending are called JCOE and UOE. JCOE is the most used method, in which the plate is bent into J, C and O shapes in consecutive steps. The E stands for Expansion, which is performed to homogenise the stresses in the pipe wall after bending. The stresses reached during bending are non-uniform through the pipe circumference. Parts of the pipe that were subjected to higher compressive stesses beyond the yield stress, will have a reduced tensile yield strength as a result of the Bauschinger Effect, even if the compressive stress is no longer present. Because dislocations were created using compressive stress, they are pinned to each other and grain boundaries in 'compressive direction'. The back stress that dislocations receive from being pinned assists the backwards movement of dislocations in 'tensile direction', hence the yield stress in tensile direction decreases. Since not every location inside the pipeline wall has a similar deformation history, differences in yield behaviour are not unlikely. Exactly how the pipeline that was used for this thesis was deformed is unknown. Multiple tested specimens throughout the tests were observed to behave similarly to specimen A1.2. The deviating yield behaviour does not seem to have an influence on the behaviour of the specimens after the yield point.

Effect of hydrogen on the base metal

Representative tensile curves for the three subsets in set A are shown in Figure 4.2. The results of all samples in Set A can be found in Appendix C. Each subset related to different environmental conditions consists of 3 tested specimens. Additionally, yield strength, UTS and strain at fracture are displayed in Table 4.2.

Neither the N_2 nor H_2 pressures seem to have an effect on the yield strength or UTS. A difference is visible in Figure 4.2, but this is because of individual variance between samples. From the values in Table 4.2 it can be seen that values for the yield strength and UTS are very similar for all three subsets, with differences falling within a standard deviation of each other. A significant difference is seen, however, in the strain at fracture. Specimens tested in 100 bar nitrogen have a strain at fracture that is 2.5% lower than those tested without gas, on average. However, the absolute difference in strain at fracture is still within one standard deviation of the samples tested without gas. Therefore this dif-

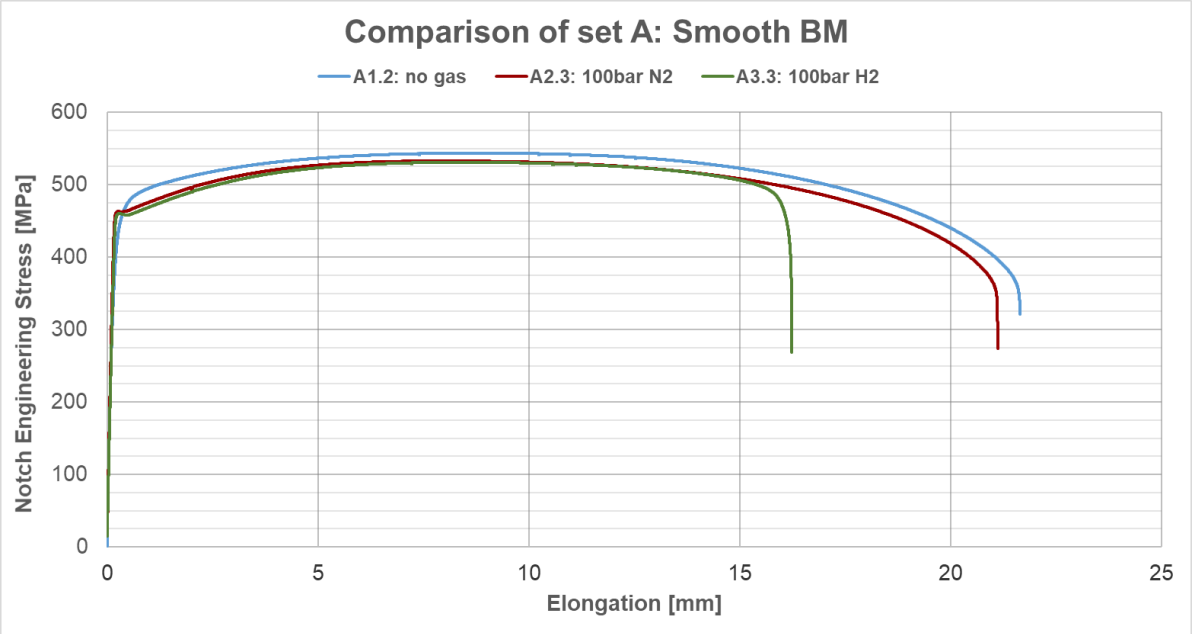

Figure 4.2: Comparison of tensile performance of the smooth base metal samples. Representative curves are displayed for each subset.

Table 4.2: The yield strength, UTS and strain at fracture for samples from set A; Smooth base metal. All averages and standard deviations are based on sets of 3 samples. The reduction in strain at fracture is calculated relative to the specimens without gas.

	Smooth BM		
Yield strength [MPa]	**No Gas**	**100 bar N2**	**100 bar H2**
Average	461.0 $\pm$ 6.4	460.0 $\pm$ 2.4	467.0 $\pm$ 5.9
UTS [MPa]			
Average	535.0 $\pm$ 6.1	532.0 $\pm$ 0.9	535.0 $\pm$ 2.9
Strain at fracture [%]			
Average	21.7 $\pm$ 0.6	21.2 $\pm$ 0.3	15.8 $\pm$ 0.9
Reduction [%]	-	2.5	27.3

ference cannot directly be attributed to the effect of the pressure. The reduction in strain at fracture of the specimens tested in 100 bar H_2 is 27.3% on average, relative to the specimens tested without gas. Because pressure of inert nitrogen gas did not cause a significant difference, this value is large enough to be confidently attributed to the effect of hydrogen on the base metal.

These findings are in line with the results that were obtained from the literature in Chapter 2. Reduction in ductility is seen as the predominant consequence of HE as represented in Figure 2.10 [46]. Some studies find influence on the UTS or yield stress of the steels they research, but with the amount of samples tested per set in this research, these findings cannot be confirmed nor rejected [56].

4.1.2. Reduction in cross-sectional area

Additional to the strain at fracture, the reduction in cross-sectional area (%RA) of the samples was calculated by measuring the cross-sectional area of the samples after fracture using a digital microscope and comparing them to the original cross-section. As an indication of the measurement error relating to this method, one specimen surface was measured five times. The standard deviation of values was found to be just 0.28% of the mean value, with the largest deviation being 0.38% of the mean. Table 4.3 lists the %RA values for the smooth base metal specimens from Set A. The higher %RA values cor-

Table 4.3: % Reduction in cross-sectional area (%RA) of samples from Set A after fracture, compared to before the tests.

	Smooth BM		
%RA	**No Gas**	**100 bar N2**	**100 bar H2**
Average	75.5 ± 0.6	76.6 ± 0.9	55.2 ± 2.6
Reduction [%]	-	-1.5	26.9

responding to the samples tested in nitrogen suggest that more necking occurred in these specimens relative to those tested without gas. However, a 1.5% difference in between sets of three samples, with standard deviations of around 1%, is likely the effect of chance. The %RA values for the samples tested in hydrogen are much lower, meaning that necking occurred to a much lesser extent than in the samples tested without gas or those tested in nitrogen. The difference between the H_2 and no gas samples is 26.9%, which approaches the value for reduction in elongation at failure which was 27.3% for these samples. This similarity in figures is expected since both reduction in ductility and %RA area are given as indicators of hydrogen embrittlement in the literature.

4.1.3. Input for deformation model

The data gathered in subset A1 was used to provide material input data for the deformation model because it was retrieved from base metal samples without the influence of any gas and pressure. Specifically, specimen A1.1 was used because the results from this test lie closest to the average of the subset.

Since Abaqus models the material behaviour regardless of geometry, the input data for mechanical material behaviour should be given in true stresses and true strains. Engineering stress σ and strain ϵ are defined as the force and change in length divided by the original cross-section of the sample, respectively. Because the original cross-section of a sample can be easily measured, these variables are often used to plot a tensile curve. However, the true stress s and strain e in a sample should be calculated by using the cross-sectional area at that moment in time rather than that when starting the test. The stresses and strains are related to each other before the onset of necking by:

$$e = ln(1 + \epsilon) \tag{4.1}$$

$$s = \sigma(1 + \epsilon) \tag{4.2}$$

Using these equations, the test data was converted to a s - e curve. Then the elastic strain E/σ was subtracted from e to give the true plastic strain e_p that Abaqus uses as input data for the strain. The s - e curve of sample A1.1 is shown in Figure 4.3 until the onset of necking in the sample. Since strains during elastic deformation are very small for metals, the engineering and true components of the stress and strain are equal before the yield point.

Five points were sampled from the s - e curve of Sample A1.1 to input into Abaqus. The first point is the yield point where $e_p = 0$ and the last point is the point of maximum force during the test, before the onset of necking, where $e_p = 0.075$. These points are shown in Table 3.5 in Chapter 3.3.

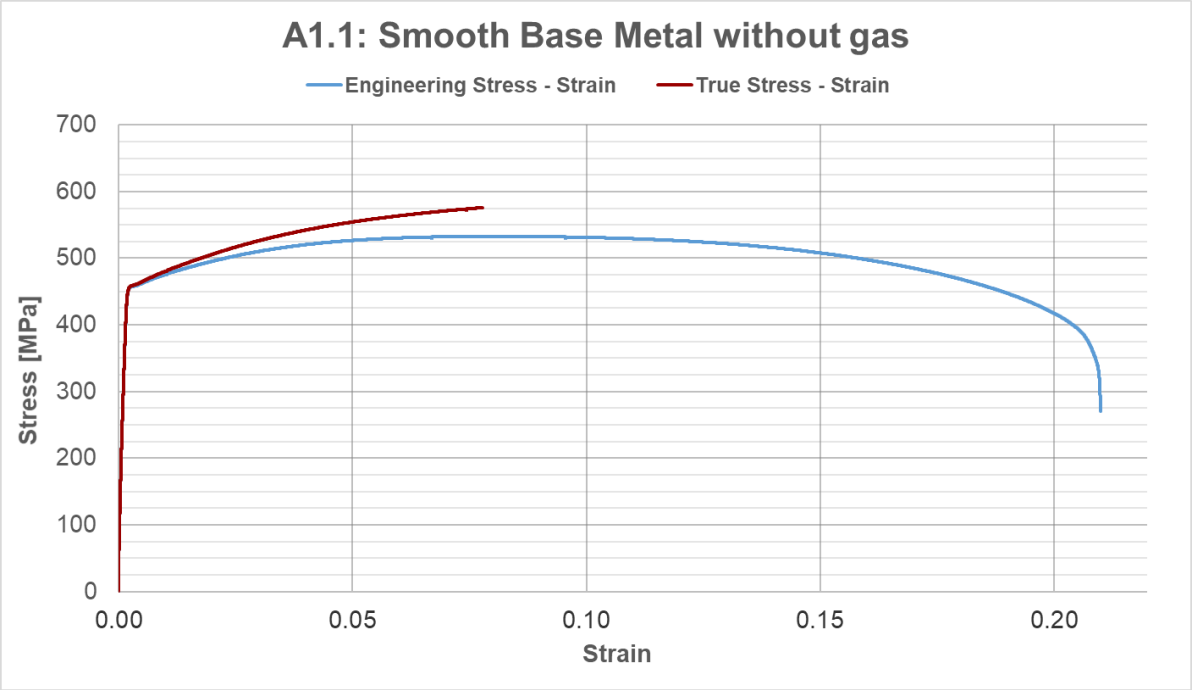

Figure 4.3: The engineering (σ - ϵ) and true (s - e) stress-strain curves for sample A1.1; smooth base metal without gas.

4.2. Notched base metal specimens: the effect of stress fields on HE

4.2.1. Deformation model verification

With the input data from Set A, the model should be able to calculate the behaviour of the samples in subset B1 until necking. Therefore, the experimental data from this subset can be used to verify the model. Sample B1.2 was compared with the deformation model. For this comparison, the model was made to fit the exact dimensions of the sample so that the results can be compared by force as well as by stress. This is useful since Abaqus outputs the cumulative force acting on the top surface of the geometry, to mimic the tensile force. The Force - Elongation curves of the deformation model and sample B1.2 are shown in Figure 4.4. Slight mismatches between the model and the test data can be observed that can be explained by varying material behaviour in between samples, as can be seen in the data from set A1. Overall, the model approaches the specimen behaviour adequately until just before the onset of necking. For the purposes of the model in this thesis, it is considered sufficient.

4.2.2. Tensile results

Effect of the Notch

The representative tensile curves for Set B are given in Figure 4.5, as elongation of the gauge length against the notch engineering stress. All curves can be found in Appendix C. The effects of the notch are immediately apparent in these curves. The elongation of these samples is only $1.08\,\mathrm{mm}$ on average for subset B1. The strain in subset A2, by comparison, reached 21.2% which corresponds to $8.9\,\mathrm{mm}$ on a gauge length of $42\,\mathrm{mm}$. This is a direct effect of strain localisation in the notch region. The notch also has an effect on the yield behavior of the sample, creating a much more gradual change in slope of the curve near the yield stress than was observed in the samples from set A. The less defined yield point arises because material inside the notch root will reach the yield point first, while sections more towards the edge will reach a similar level of stress at increasing amounts of force, since the cross-sectional area in the notch changes very gradually. The curve for the entire sample will therefore show a gradual decrease of slope from the elastic region towards the plastic region.

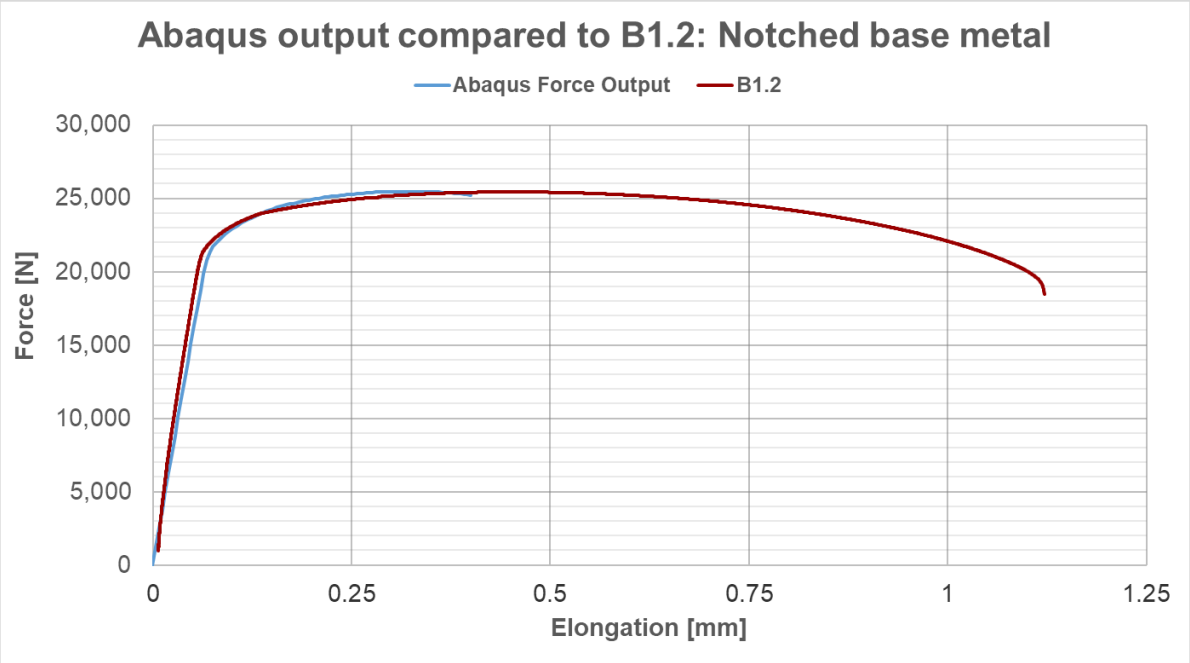

Figure 4.4: The Force - Elongation curves of notched base metal sample B1.2 tested in 100 bar N_2 compared to the deformation model using material data from smooth base metal sample A1.1.

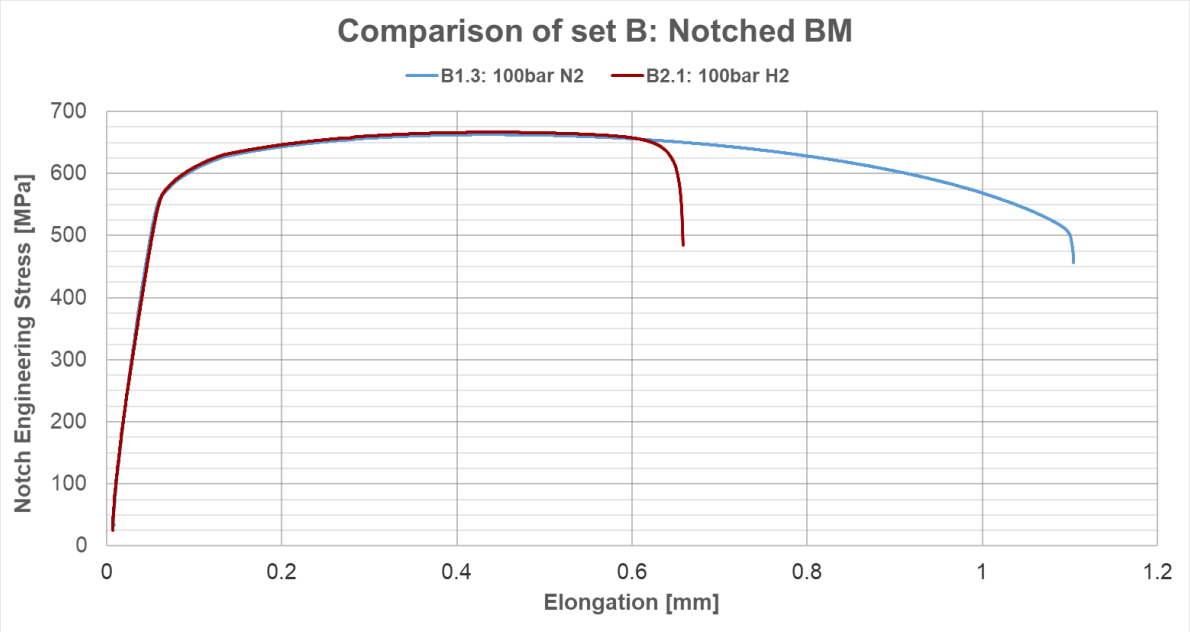

Figure 4.5: A comparison of tensile curves from both subsets B1 and B2 of notched base metal in nitrogen and hydrogen, respectively. Representative curves for each subset are presented.

Furthermore, the tensile stresses reached in set B are higher than those from subset A2. This can be explained with the Von Mises yield criterion as shown below.

$$(\sigma_1 - \sigma_2)^2 + (\sigma_2 - \sigma_3)^2 + (\sigma_3 - \sigma_1)^2 = 2{S_y}^2 \tag{4.3}$$

Figure 4.6: a) The true Von Mises and b) S22 stresses from the deformation model at the point of UTS. S22 is the stress in y-direction modelling the stress in direction of the tensile tester. c) Stresses reached at the point of UTS.

(a)

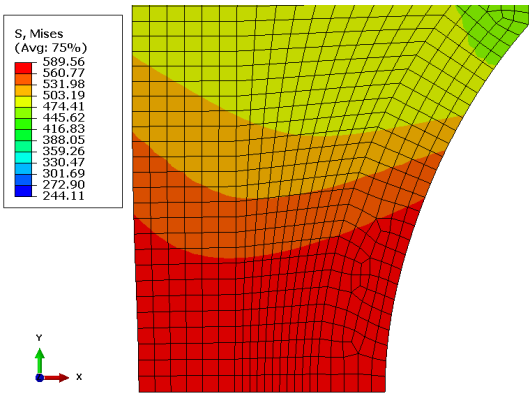

(b)

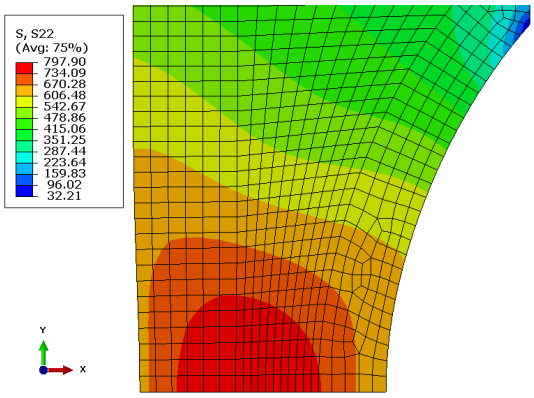

(c)

	Mises	S22
True Stress	590	798
Engineering stress	525	711

In this equation, the different principal stresses are displayed as σ_1, σ_2 and σ_3 respectively as positive when in tensile direction. σ_1 is the stress applied by the tensile device and that displayed in Figure 4.5. The effect of a circumferential notch in combination with an internal pressure is the creation of stresses in different directions, like a hoop stress in radial direction which results in a σ_2 that is nonzero and positive. S_y denotes the onset of yielding in the sample, which needs to be reached to cause yielding. Introduction of other stresses than just σ_1 will decrease the left hand term of the equation if σ_1 does not increase. This means that when a state of tri-axial stress is reached, higher stresses are needed to cause deformation. This is the reason that stresses in set B are higher than those from subset A2. The effect can be visualised using the deformation model, as is shown in Figure 4.6 which shows the Von Mises equivalent stress in Figure 4.6a and the stress in y-direction, or that caused by the tensile tester in Figure 4.6b.

The true stresses given in Figure 4.6 can be recalculated to give an approximation of the engineering stresses. These values are given in Figure 4.6c in order to enable comparison with tensile data. The Von Mises stress at this point in the model is close to the measured UTS from subset A1 of 535 MPa. S22, which is σ_1, is 711 MPa. This is close to the measured UTS from subset B1 of 674 MPa. The tri-axial stresses in the sample at this point are causing the necessary tensile stress for deformation to rise above the actual yield stress of the material. Stress tri-axiality is usually reported in literature as a dimensionless value that is calculated by taking the ratio of the hydrostatic stress to the Von Mises equivalent stress or $Stress\ tri-axiality = \sigma_h/\sigma_{\text{mises}}$. Figure 4.7b shows the stress tri-axiality in the notch at UTS, and Figure 4.7a shows the pressure. The pressure and hydrostatic stress relate by $\sigma_h = -\sigma_p$.

Effect of hydrogen on notched base metal specimens

The two subsets in set B as shown in Figure 4.5 show very similar tensile results to each other. Both yield strength and UTS only differ slightly between the two sets. The data for yield strength, UTS and elongation at failure is shown in Table 4.4. There is a large observable difference in elongation at failure because of the effect of hydrogen gas. A reduction in ductility of 40.4% is observed, which is higher than the reduction value for subset A3 compared to A1 which was 27.3%. This is also an effect of the notch geometry, as it is known that high σ_h exacerbates the effect of hydrogen embrittlement. In this case, the reduction in elongation of notched specimens is about 1.5 times as large as that of smooth specimens. Table 4.5 presents the %RA values of set B. As expected, the reduction in cross-sectional

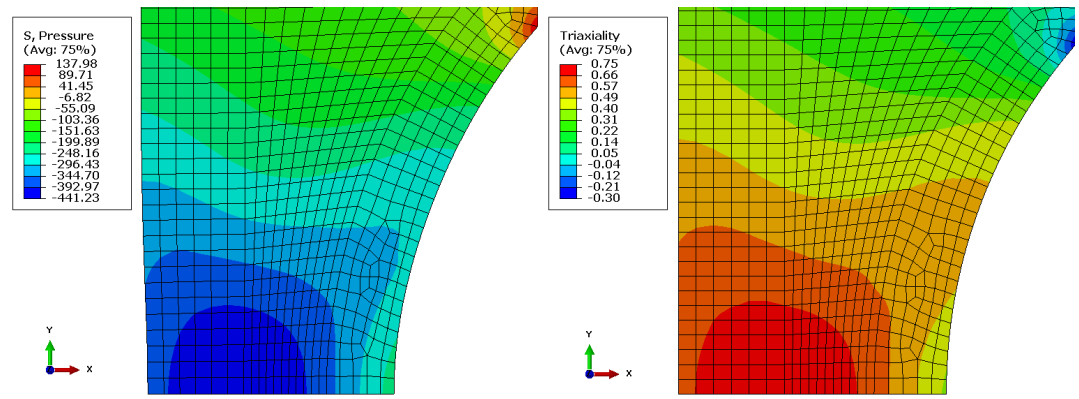

Figure 4.7: The a) pressure and b) stress tri-axiality inside the deformation model near the point of UTS. Since Abaqus outputs the pressure instead of the hydrostatic tensile stress, and they each other's negative, the colour scheme of a) should be read as its inverse.

Table 4.4: Averages and standard deviation of the yield strength, UTS and elogation at failure for the base metal notched samples from set B. Both subsets consist of 3 specimens.

	Notched BM	
Yield Strength [Mpa]	**100 bar N2**	**100 bar H2**
Average	626.0 $\pm$ 24.6	631.0 $\pm$ 18.3
UTS [Mpa]		
Average	674.0 $\pm$ 15.1	677.0 $\pm$ 12.9
Elongation at fracture [mm]		
Average	1.08 $\pm$ 0.04	0.64 $\pm$ 0.06
Reduction [%]	-	40.4

area is much diminished in the samples tested in H_2 compared to those tested in N_2. Samples tested in H_2 have a 28% smaller %RA value than those tested in N_2, on average. This number is not as high as the reduction in elongation between the two subsets, meaning that the samples from subset B2 showed proportionally more necking relative to the elongation than those from B1.

The %RA value is 26.9% for subset A3 relative to A1, meaning that the difference in %RA between sets A and B is not as large as the difference in reduction of ductility. The %RA values of both sets instead stay very similar to each other regardless of differences in sample geometry. This suggests that %RA values rather than reduction in elongation as an indicator for HE might prove a more constant indicator influenced more by material properties than geometrical effects.

Table 4.5: The %RA values for set B of notched base metal specimens. Both subsets consist of 3 specimens.

	Notched BM	
%RA	**100 bar N2**	**100 bar H2**
Average	72.1 $\pm$ 1.0	52.0 $\pm$ 2.0
Reduction [%]	-	28.0

4.3. Notched weld metal and the effect of different hydrogen pressures

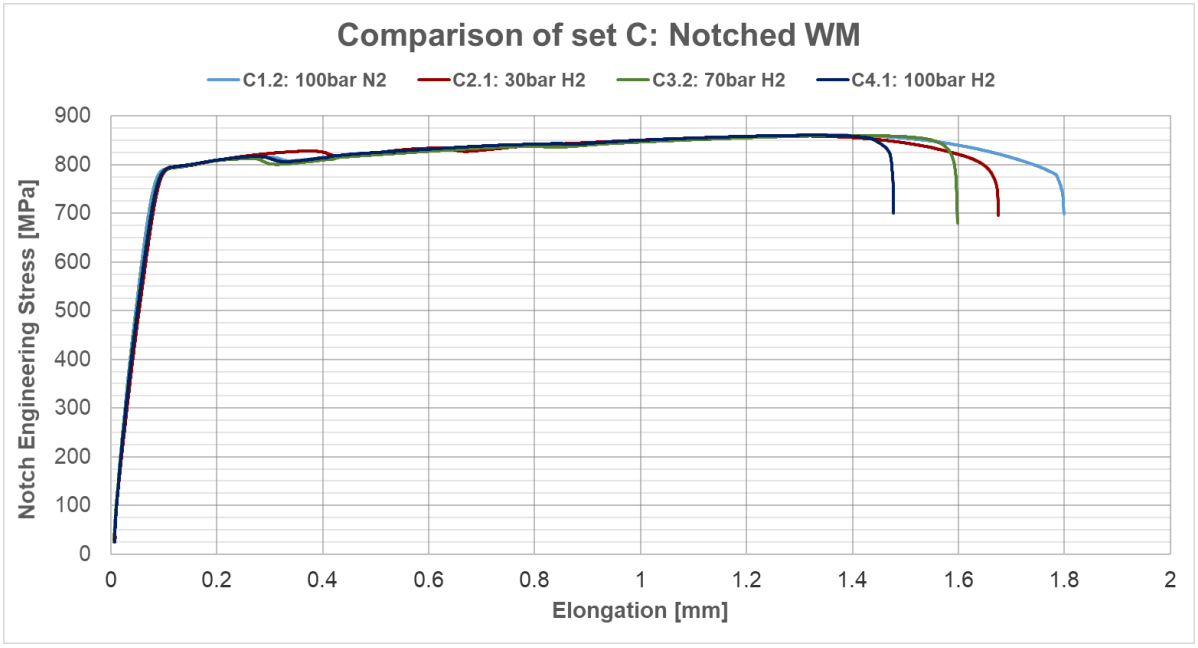

(a)

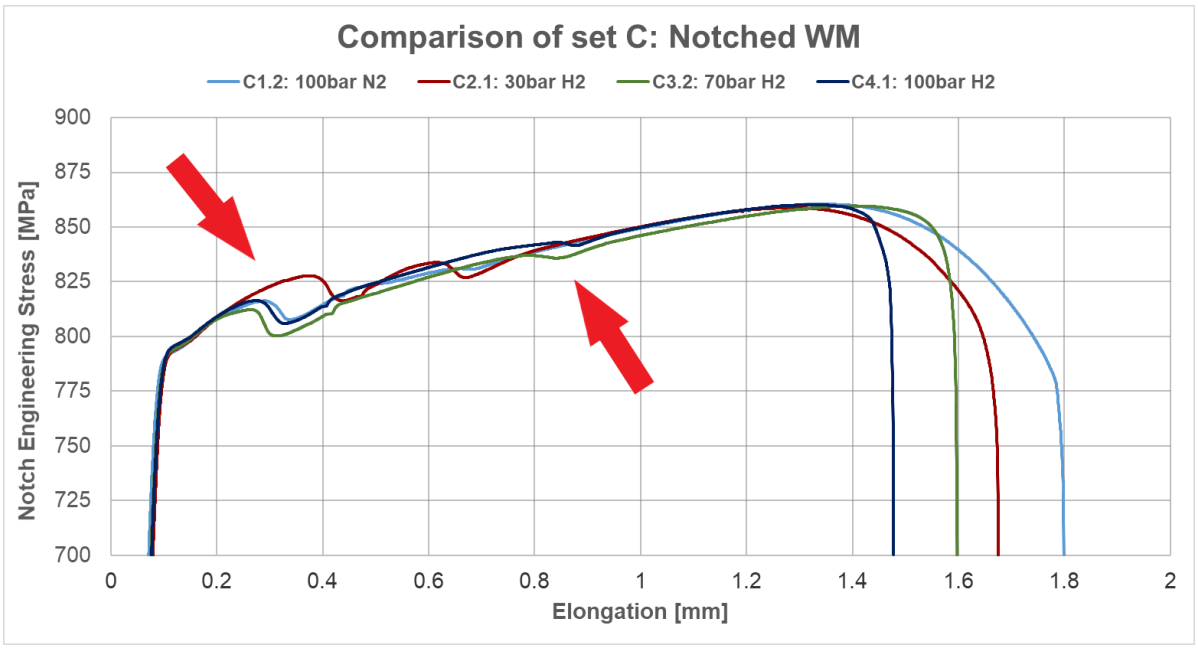

(b)

Figure 4.8: a) A comparison of different specimens from set C, the samples including weld zone, and b) A magnified section of the set C curves shown in Figure 4.8a.

4.3.1. Effect of the weld metal

Figure 4.8a shows the representative curves for Set C, consisting of specimens with the notch applied in the weld metal. All other curves can be found in Appendix C. Set C consists of 4 subsets, one tested in a nitrogen environment and three tested at different hydrogen pressures. Table 4.6 lists the related data for yield strength, UTS and reduction in elongation. Like in the previous sets, yield strength and UTS are not affected by either the pressure or the presence of hydrogen gas. The curves in Figure 4.8a all show similar behaviour, which is different from that of the notched base metal samples in multiple ways. Firstly, the yield point of the weld samples shows much more similarity to that of the smooth base metal samples than that of the notched base metal ones. This suggests that it is the base material outside of the notch rather than the notch region itself that starts yielding first. A comparison between the smooth base metal and notched weld metal samples is made in Figure 4.9.

The second way in which the weld specimens differ from the notched based metal ones, is the emergence of two points of reduction in force in the plastic zone of the tensile curves. Figure 4.8b presents the plastic region of the curves in Figure 4.8a. These two drops in force can be related to two different yield points that belong to the HAZ and the weld metal, respectively. In Section 3.1.3, it was discussed that the hardness values of the HAZ lie in between those of the base metal and the weld metal. This would suggest that the yield strength of the HAZ also lies in between those of the other metals. Therefore the first drop in force is assigned to the yield point of the heat affected zone. Moreover, because the weld metal is present in the notch, more gradual yield behaviour is expected like that of the notched base metal samples from set B. However, because different metals are deforming in series, their behaviours are superposed in the curves, making their individual yield behaviour harder to distinguish. When the two yield points are compared from Figure 4.8b, it can be observed that the second yield point shows a much more gradual drop and recovery of the force, suggesting that this yield point belongs to the weld metal. After the weld metal yields, strain hardening in the base metal and HAZ outgrow the hardening of the weld metal, causing strain localisation in the notch region that eventually results in fracture.

Lastly, the weld metal specimens show a larger elongation until failure than the base metal specimens, on average. This is shown in Table 4.6. The specimens tested in nitrogen show an elongation of $1.74\,\mathrm{mm}$ compared to $1.08\,\mathrm{mm}$ in the specimens from subset B1. However, some of this extra elongation happened in the smooth base metal area outside the notch. Samples tested in $100\,\mathrm{bar}$ H_2 show $1.48\,\mathrm{mm}$ of elongation compared to $0.64\,\mathrm{mm}$ in the base metal. In nitrogen, this is a 61% increase in elongation. In hydrogen it is a 130% increase. This means that relative to the base metal, the weld metal retains more of its ductility when subjected to hydrogen.

Effects of hydrogen pressures

From the data presented in Table 4.6, the reduction in elongation at failure of the samples from set C can be seen to increase with increasing pressure. The elongation at failure increases from 3% to 14% between 30 and $100\,\mathrm{bar}$ of hydrogen pressure. Even though the amount of different pressures that were tested is low, the existence of a trend is evident.

Table 4.6: The values for the yield strength, UTS and elongation at failure for the notched weld specimens of set C. Subsets C1, C2 and C3 consist of 3 specimens each. Subset C4 consists of 5 specimens.

	Notched WM			
Yield Strength [Mpa]	**100 bar N2**	**30 bar H2**	**70 bar H2**	**100 bar H2**
Average	810.0 ± 5.9	813.0 ± 7.1	812.0 ± 2.7	812.0 ± 4.8
UTS [Mpa]				
Average	857.0 ± 6.4	859.0 ± 1.8	862.0 ± 1.6	861.0 ± 1.5
Elongation at failure [mm]				
Average	1.72 ± 0.16	1.67 ± 0.02	1.60 ± 0.03	1.48 ± 0.11
Reduction [%]	-	3.0	7.3	14.0

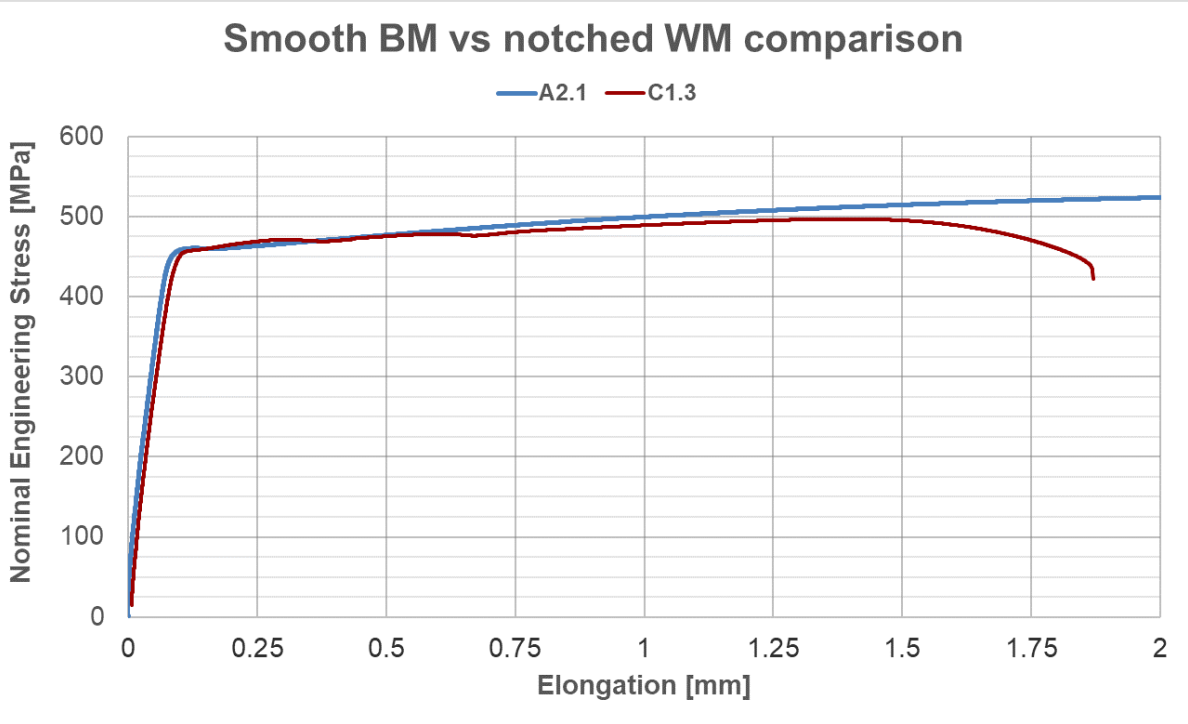

Figure 4.9: The curves of specimens A2.1 and C1.3 to compare the yield points of the smooth BM and notched WM specimens.

	Notched WM			
%RA	**100 bar N2**	**30 bar H2**	**70 bar h2**	**100 bar H2**
Average	48.2 $\pm$ 1.5	42.9 $\pm$ 0.6	43.0 $\pm$ 0.8	41.7 $\pm$ 3.0
Reduction [%]	-	11.0	10.9	13.5

Table 4.7: The %RA values of all samples from set C, notched weld metal specimens. Subsets C1, C2 and C3 consist of 3 specimens each. Subset C4 consists of 5 specimens.

Table 4.7 presents the %RA data for Set C. A first observation is that even when tested in a nitrogen environment, the weld samples show a reduction in cross-section of only 48.2%. This means that even though their elongation until failure is much larger than that in the base metal specimens, they experience less necking. Furthermore, the reduction in area only decreases by 11% and 10.9% for hydrogen pressures of 30 bar and 70 bar respectively, and 14% for 100 bar. The standard deviation of the %RA values for the subset tested in 100 bar H_2 is high compared to the other subsets in set C because of one sample that showed a very small %RA value compared to the others from the same subset. If this measurement is dropped from the calculation, the average %RA becomes 43.03% with a standard deviation of 1.8%. This would give a reduction of %RA compared to the nitrogen tested sample of 10.8%, which is not significantly different from the values seen for subsets C2 and C3. This means that if this measurement is dropped from the subset, there is no decrease in %RA visible as an effect of the hydrogen pressure from these tests. This suggests that there is no correlation between the reduction in ductility and the reduction in cross-sectional area, even though a higher ductility is normally a result of more necking, which decreases the cross-sectional area of a tensile sample. This mismatch between the data for ductility and that of %RA for both the notched base metal and weld metal specimens shows that the %RA measurements are not a reliable source of predicting the reduction in ductility of tensile samples due to hydrogen embrittlement.

4.4. Fractographic analysis

In order to further clarify the findings from the tensile tests and cross-sectional area measurements, fractographic analysis was performed on the fractured specimens with SEM and optical microscopy. Because two materials were researched, they will be discussed separately in this section. The section will first discuss general obsevations regarding cracking, before the base metal and weld metal will be discussed in order. Lastly, the section briefly touches upon which HE models might be contributing to fracture.

4.4.1. Crack initiation

When a notch is applied to a tensile sample, the largest stress concentration is created on the surface of the notch root. For this reason, fracture is expected to initiate at this location. For all samples tested in this research, however, fracture was observed to travel from the inside surface of the sample towards the outside. Fracture even initiated on the inside surface under influence of hydrogen, when the material is expected to behave in a more brittle way. To investigate the cause of this, tilted SEM images were made of the inside surfaces of some samples. It was discovered that secondary cracking parallel to the fracture surface often occurs in the tensile samples. Figures 4.10a and 4.10b show the secondary cracks below the fracture surfaces of specimens tested without gas and in 100 bar H_2, respectively. Both show extensive secondary cracking with cracks that seem to reach at least 100 µm of depth. The cracks surfaces are dominated by ductile failure modes for the no gas sample and quasi-cleavage for the hydrogen sample. In comparison, secondary cracks in a notched base metal sample seem to be less deep than in the two smooth specimens, as shown in Figure 4.11. An explanation for the difference in crack depth could be that they are deeper in the smooth specimens because the samples underwent more strain throughout the gauge length, whereas strain in the notched samples was concentrated to the notch root. This larger zone of strain in the smooth specimens could have opened smaller pre-existing cracks that were present on the inside surface of the samples.

The cracks in the inner surface of the sample in Figure 4.11 appear to be spaced apart regularly by 100 to 200 µm. Furthermore, the fracture surface also originated from one of these cracks. This suggests that there could have been pre-existing irregularities on the surface, perhaps because of the machining process. When testing in a hydrogen environment, small defects like these cracks could cause premature failure of a test specimen. The samples for this thesis were reamed on the inside surface, meaning that their surfaces were mechanically smoothened. Therefore the defects on the surface are not considered to be any more severe than what might be present on the surface of other pipeline material, so failure in these tests could be suspected to be slowed down rather than sped up relative to what might happen to actual pipelines in operation.

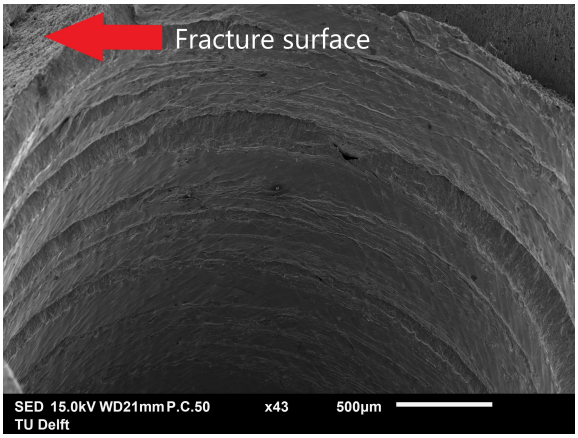

(a)

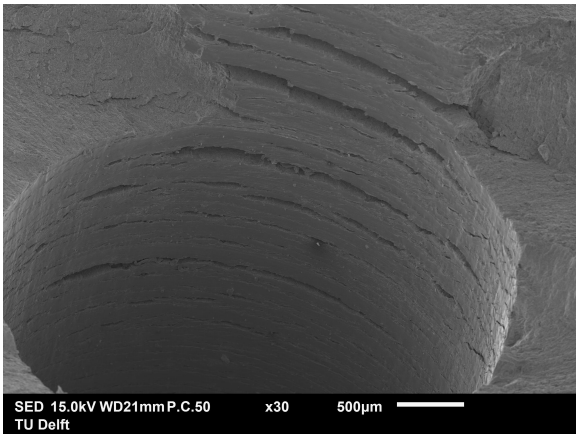

(b)

Figure 4.10: a) A 45° tilted image of the inside surface of a smooth BM sample tested without gas and b) tested in 100 bar H_2.

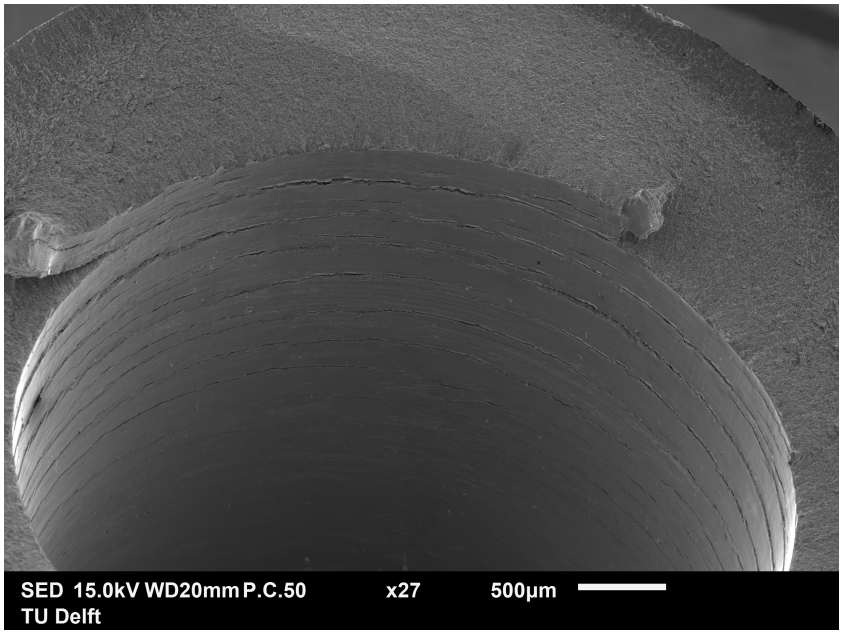

Figure 4.11: A 45° tilted image of the inside surface of a notched BM sample tested in 100 bar H_2.

4.4.2. Base metal

Fracture mechanism without H_2

The fracture surfaces of base metal samples tested without gas and with N_2 were analysed as a reference to be able to identify any changes that happen when H_2 is introduced. A 45° tilted view of the fracture surface of a smooth BM sample tested without gas is shown in Figure 4.12a, from which a very distinct cup-cone fracture can be seen. This morphology is found in ductile metals where MVC is the dominant fracture mode. The dominance of this fracture mechanism can also be identified in a higher magnification image of the surface given in Figure 4.12b, which shows dimpling of the surface on scale of $1-10\,\mu m$. This same micro-void coalescence fracture mode is dominant across the entire fracture surface of the samples from this subset. The morphology of the samples tested in 100 bar N_2 is similar to that of subset A1 without gas on a macroscopic as well as microscopic level. The hoop stress induced by the pressure does not seem to have influenced the fracture surface. This is expected since the tensile performance of the two subsets was very similar as well.

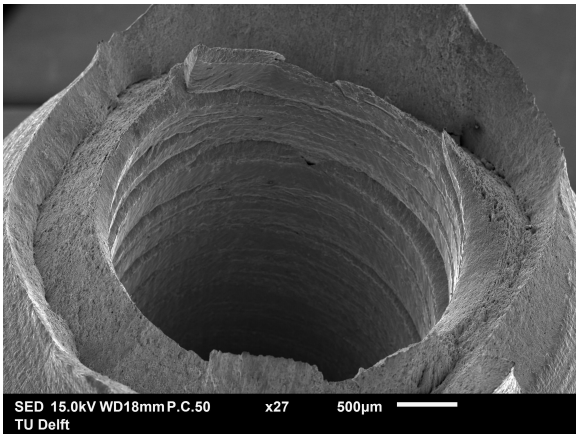

(a)

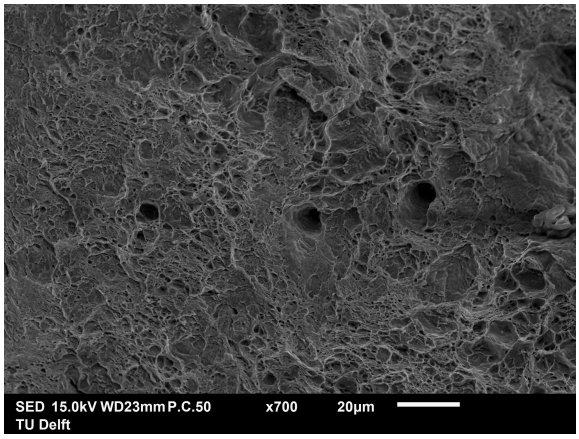

(b)

Figure 4.12: a) A 45° tilted low magnification overview of a smooth BM sample tested without gas, b) An overview of the MVC fracture mode of the surface shown in (a).

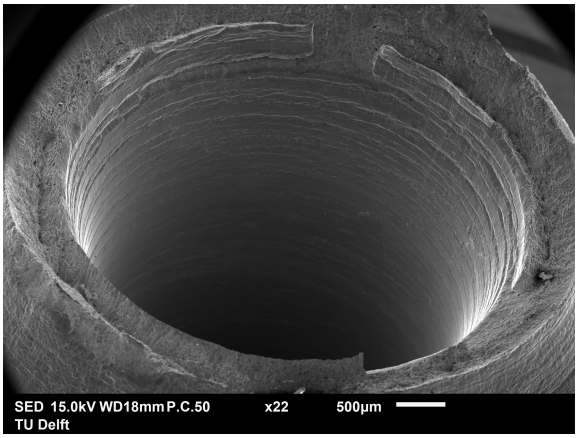

(a)

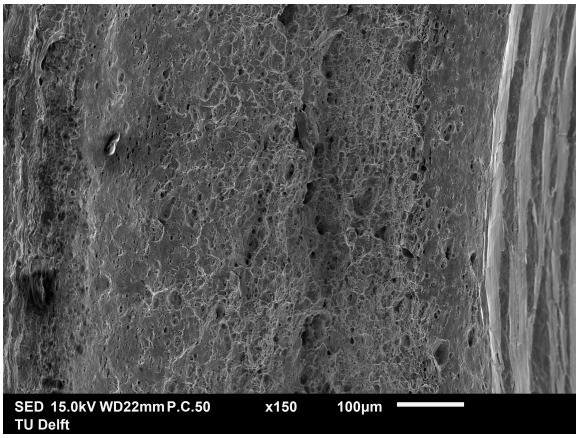

(b)

Figure 4.13: a) a 45° tilted view of a notched BM sample tested in 100 bar N_2, b) an untilted view of the sample shown in (a) showing a large void size in the middle section of the wall thickness.

In the notched BM specimens tested in nitrogen from subset B1, a similar cup-cone morphology is visible over the whole cross-section of the sample. 4.13a shows a low magnification overview of a section of the wall thickness of the specimen. Figure 4.13b shows a magnified image of the fracture surface across the wall thickness. A difference can be seen in this picture between the size and number of dimples in the middle section of the wall thickness and the regions near the edges. Near the edges of the fracture surface, the density of dimples is much lower than that seen on the fracture surfaces of the smooth samples. The middle section, however, shows much larger dimples than those seen on the samples from set A. The amount of dimples in the middle section is much higher than that near the edges of the same specimen. The difference between the middle and outer section of the fracture surface can be explained by the zone of hydrostatic stress that is created by introducing a notch into the sample. As shown in Figure 4.7a, the middle section is subjected to the highest hydrostatic stresses. This stress state promotes creation and growth of voids, resulting in a higher density of dimples than on the outer edges of the fracture surface.

Fracture of the base metal in H_2

Base metal samples that were tested in a hydrogen environment show a very different fracture surface than those tested in nitrogen gas. To illustrate this, Figure 4.14 shows an overview of the fracture surface of a smooth base metal sample tested in 100 bar H_2. Even the macroscopic overview given in Figure 4.14a looks distinctly different from that of the nitrogen tested samples. The micro-void coalescence fracture has almost completely disappeared from the fracture surface and the cup-cone morphology is no longer present on the surface. Instead, the fracture surface is largely flat, except for a small region near the outside surface, which is shown in Figure 4.14b, where a transition occurs to micro-void coalescence and shear lips appear.

A magnification of the main fracture mode is given in Figure 4.14c. This mode can be identified as quasi cleavage fracture based on its smooth features on an irregularly faceted fracture surface. Furthermore, secondary cracks can be observed on the fracture surface, that have been magnified in Figure 4.14d, which are assumed to be created as a result of the hoop stress that is present in the sample during testing. A further magnified image is shown in Figure 4.15, where characteristic features like ridges and secondary cracks have been marked.

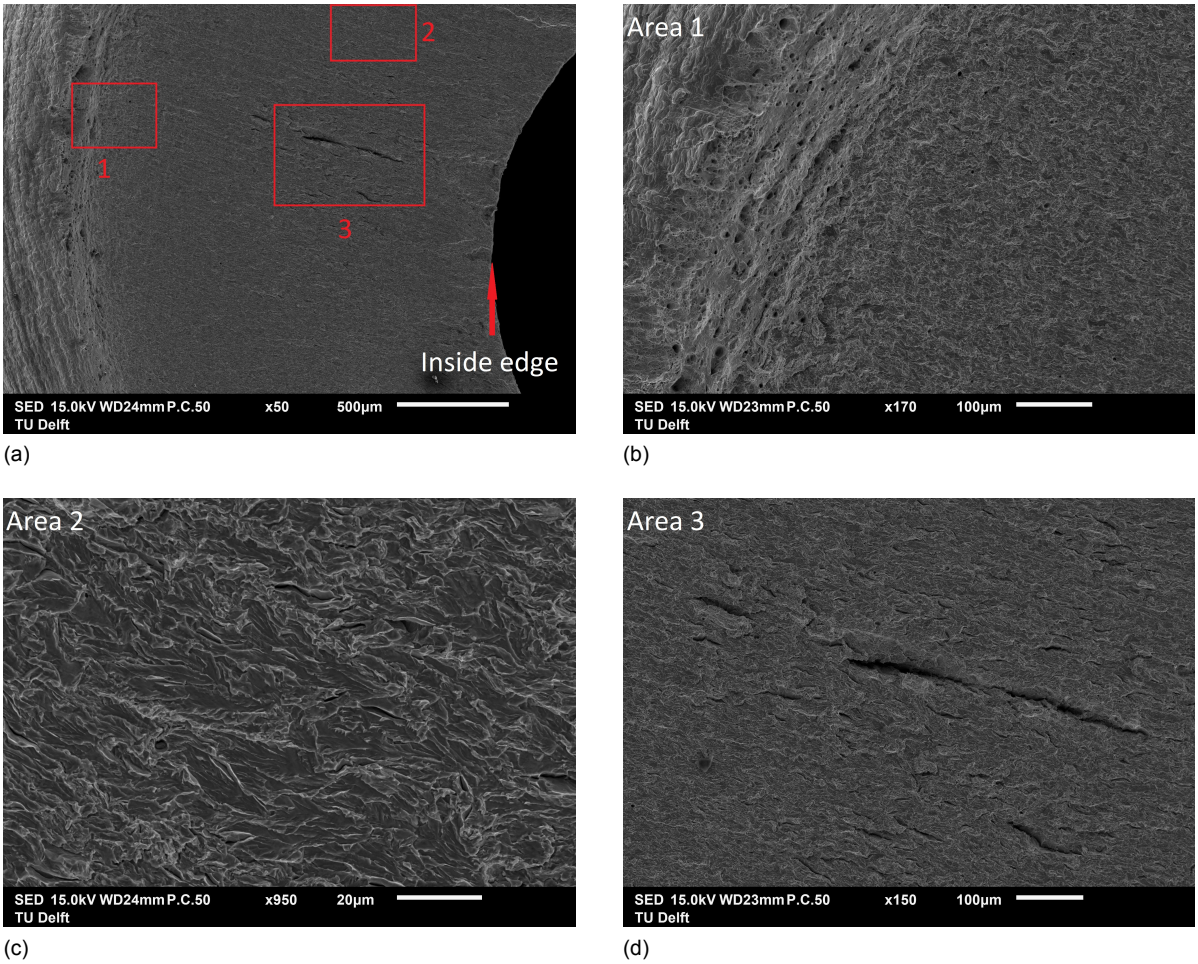

Figure 4.14: An overview of the fracture surface of a smooth BM sample tested in hydrogen gas showing a) a low magnification overview of the wall thickness, b) a magnification of area 1 marked in (a), c) a magnification of area 2 marked in (a) and d) a magnification of area 3 marked in (a).

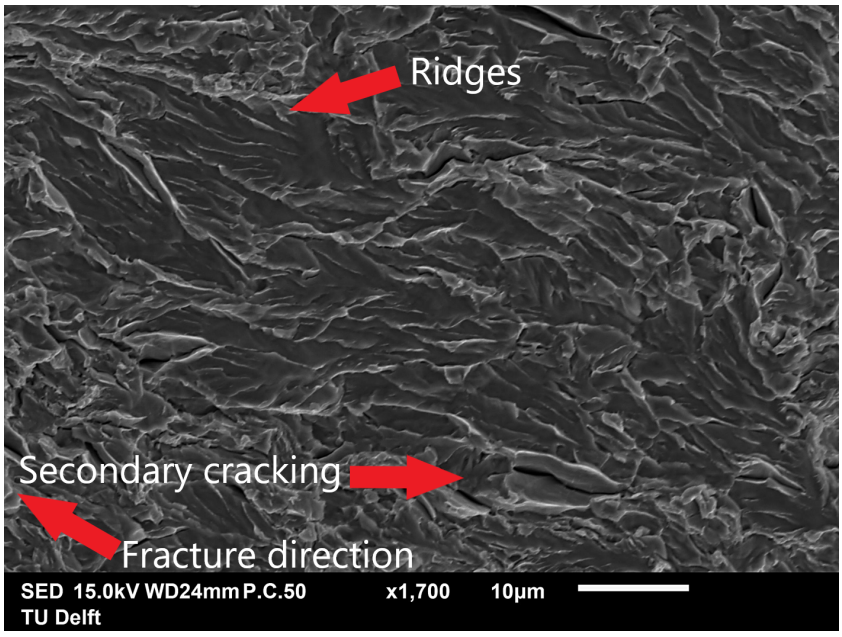

Figure 4.15: A high magnification image of characteristic quasi-cleavage features in a smooth BM specimen tested in 100 bar H_2 gas.

Notched base metal specimens tested in hydrogen gas showed a higher UTS and elongation at failure than the two other samples from its subset, while it also showed more pronounced characteristics of HE. Some images of a fracture surface from this subset are shown in Figure 4.16. Figure 4.16a shows that this specimen underwent significant secondary cracking in the hoop direction. Figure 4.16c presents a magnified image of the area marked in Figure 4.16a, zoomed into the secondary cracks, which shows larger scale 'ridges' that have plastically deformed towards the opposing side of the crack. This indicates that plastic deformation occurred at these small scales. At even higher magnification, Figure 4.16b shows undulations and ridges on the fracture surface on a microscopic scale. The undulations show similarity to those described by Martin et al, whose image is shown in the literature review in Figure 2.6 [37]. Furthermore, the ridges in Figure 4.15 are of the same scale as Martin et al. present in their paper, so their proposed model is assumed to have occurred in these samples. This shows that during QC cracking, plastic fracture mechanisms dominate at a microscopic scale while the fracture surfaces look brittle on a macroscopic scale. This change in fracture mode towards QC with extremely localised plastic deformation reflect the reduction in ductility that was found in the tensile tests for these samples.

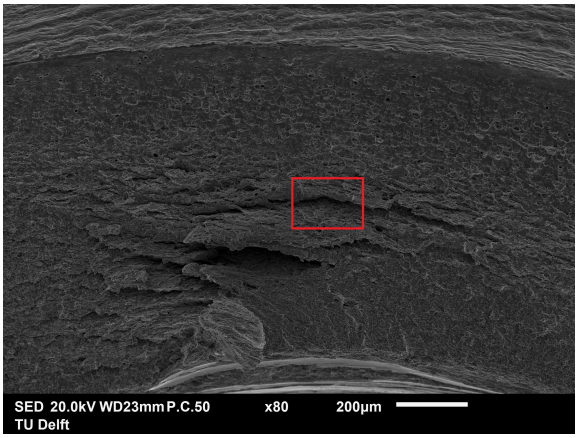

(a)

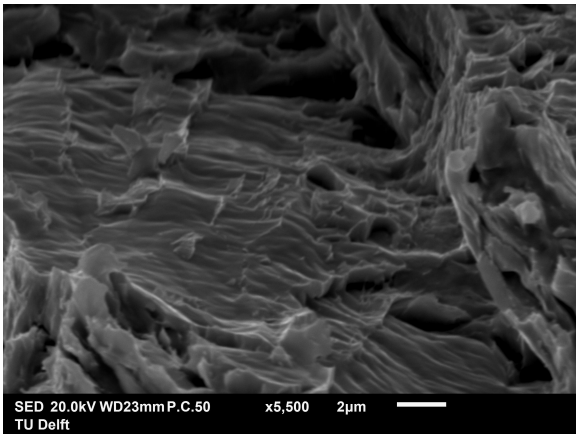

(b)

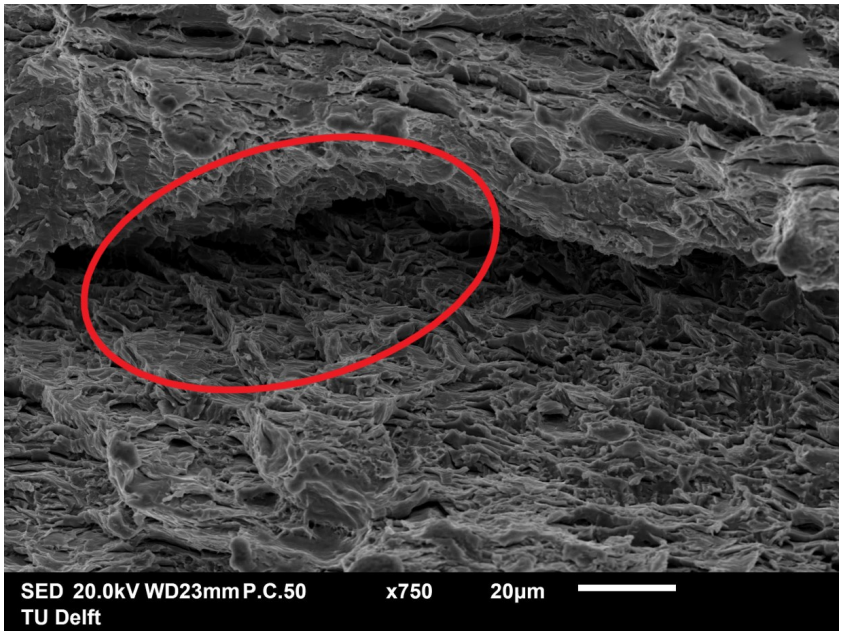

(c)

Figure 4.16: An overview of the fracture surface of a notched BM sample that was tested in hydrogen, showing a) a low magnification overview of the wall thickness, b) a higher magnification image of the area marked in (a), c) the area in between secondary cracks which show ridges matching on opposite surfaces in the circled area.

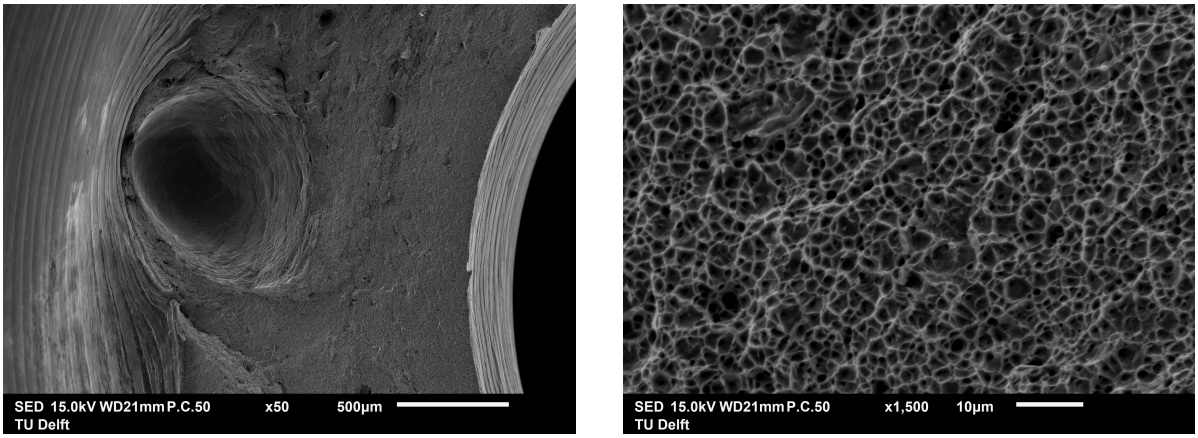

(a) (b)

Figure 4.17: An overview of the fracture surface of the a WM sample tested in 100 bar N_2 showing a) the presence of a weld defect and b) a higher magnification image of the MVC fracture mode which shows dimples of a much smaller size than in the BM.

4.4.3. Weld metal

Fracture mechanism without H2

The weld metal fractures according to the same micro-void coalescence mechanism as the base metal. However, many secondary cracks as well as pits were present that most likely originated due to the presence of different microstructures within weld passes. Overall, the cup-cone fracture morphology was still present. Some samples contained weld defects of a considerable size. Figure 4.17a shows such a weld defect of approximately 500 µm in diameter. It is unclear whether the presence of weld defects in the samples had any distinguishable effect on their tensile performance. Figures 4.17b shows a magnified image of the fracture mode of the weld metal without the influence of hydrogen. Although the fracture surface shows the same dimpled appearance as the base metal samples, the dimples in the weld metal are of a much smaller size than those in the base metal. Where the base metal showed dimpling on a scale of $1-10$ µm, those in the weld metal are on the order of 1 µm without showing any larger dimples. This is in line with the finer microstructure on the same order of size that was observed in Chapter 3.1.

Fracture of the weld metal in H_2

The weld metal undergoes a similar change in fracture mode from MVC to QC as the base metal when tested in hydrogen gas. However, the extent to which this happens in the weld metal is different. Figure 4.18 shows a 45° tilted view of the wall thickness of a specimen that was tested in 70 bar H_2. Cracking initiates from the inside surface into a zone where QC is the dominant fracture mechanism. This zone of the fracture surface stays perpendicular to the loading direction. In comparison with the QC fracture surfaces of the base metal, distinguishable elements on the weld metal surfaces are much smaller in scale. Similar to the grain size in the weld metal, the WC facets are around 1 µm in size. Secondary cracking was less prominent in the weld specimens, as was the appearance of ridges and smooth areas that were all found on the base metal fracture surfaces. Since the size of individual elements in the weld metal is on the order of the size of the ridges that were formed in the base metal, the refined microstructure could have stopped them from forming at the same scale in the weld metal.

Approximately halfway through the wall thickness, the fracture surface in Figure 4.18 starts curving upwards. At this point, dimples start appearing inside zones dominated by quasi cleavage fracture, and the fracture mode gradually changes to become more MVC dominant. Eventually, no more QC features are visible and the sample displays clear shear lips near the outer edge. This change in fracture mode has been indicated in Figure 4.19 where 4.19a presents an untilted overview of the fracture surface, 4.19b an image of the QC surface, 4.19c an image of the transition zone and 4.19d an image of the MVC dominated surface.

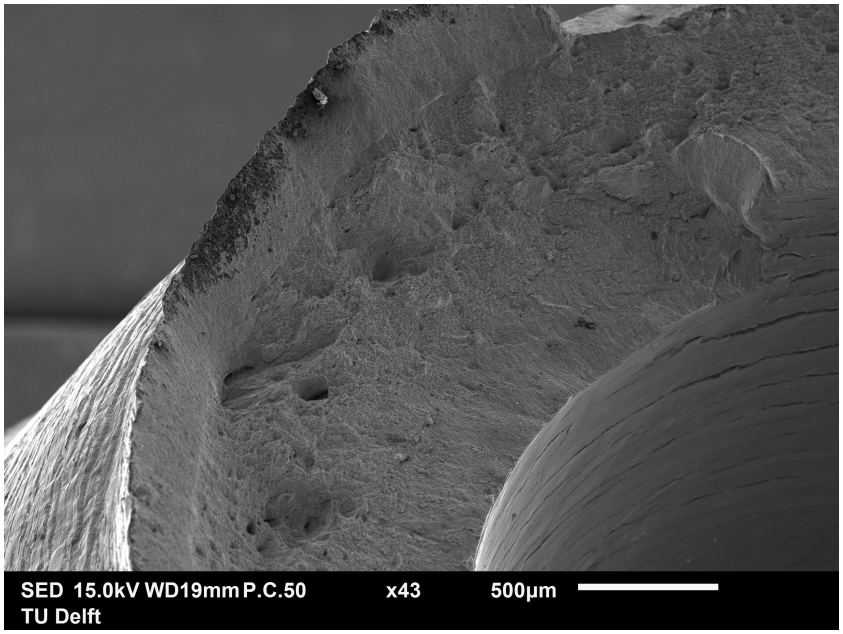

Figure 4.18: A 45° tilted view of the fracture surface of a WM specimen tested in 70 bar H_2.

Similar behaviour was observed in all WM samples that were tested in H_2 gas. In 30 bar of H_2 gas, the zone of QC cleavage extends onto the fracture surface for a distance on the order of 100 µm, in 70 bar it is 400 µm and in 100 bar it is up to 600 µm. However, because of variable distances in between samples as well as in between different location of the same sample, no relation can be concluded between the distance of the QC zone and the pressure with any confidence. The small increase in QC dominated fracture area with pressure could be an explanation to why the %RA values for weld samples were very similar for different pressures. A larger area fraction of QC relative to MVC dominated fracture area would result in a smaller reduction in area at fracture. Since the differences in QC dominated fracture area between weld samples are small, this could either be a cause of or contribute to the small differences observed in the %RA values.

Change in fracture mode

No definitive answer to why the fracture mode changes from QC back to MVC in the weld metal samples was found in this research. The three variables that contribute most to the change in fracture mechanism are the hydrogen concentration, the stress state and the microstructure.

Figure 4.20 shows two locations on the fracture surface of a smooth BM specimen tested in 30 bar H_2. During the test, a crack on the side given in Figure 4.20a propagated through the entire wall thickness to create a hole in the sample. The hydrogen gas escaped through this hole without causing failure of the test sample, creating a sudden release of gas and hoop stress from the sample during the test. Another area of the specimen as shown in Figure 4.20b can be seen to fracture with the QC fracture mode dominating up to a certain point. This is believed to be the point at which the gas escaped the specimen. Figure 4.21 presents a magnified view of this transition point which can be seen to transition very abruptly on a µm scale. In Section 4.1.1 it was shown that the pressure does not have a significant effect on the performance of the tensile specimens because the hoop stress that it creates is very small compared to the tensile stresses caused by the tensile tester. This suggests that the release of the hydrogen gas from the sample causes the sudden change in fracture mode. This means that presence of hydrogen gas during crack growth might be the main contributor to the existence of the quasi cleavage fracture mode. A crack that forms on the inside of a tensile specimen might propagate with the QC mode as long as hydrogen gas is in contact with the fracture surface, and revert back to MVC when the gas is no longer there.

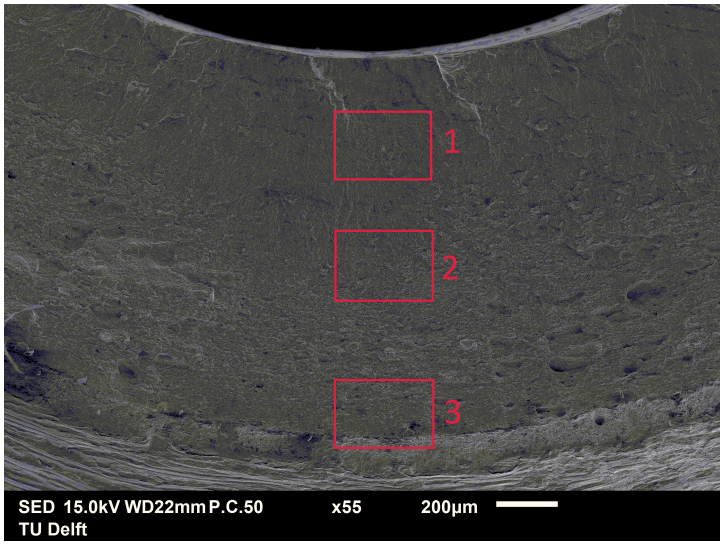

(a)

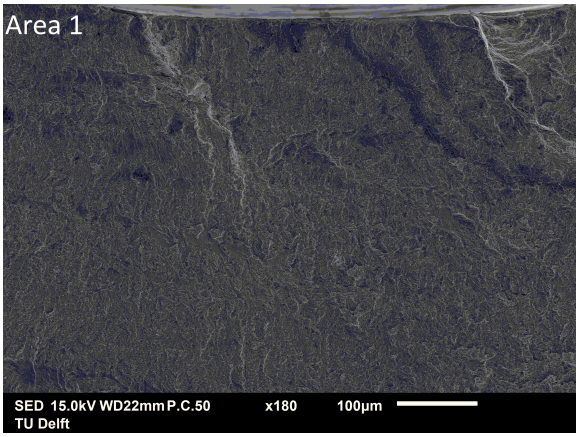

(b)

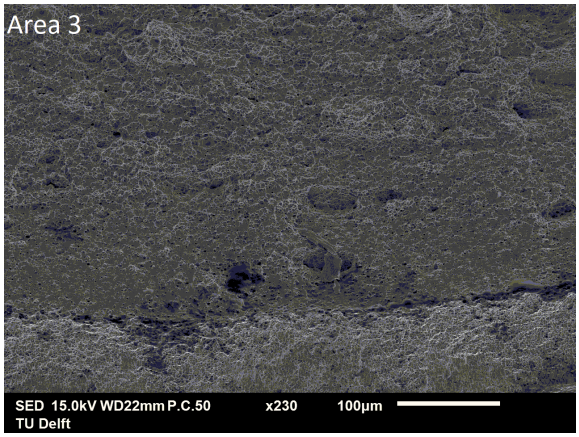

(c)

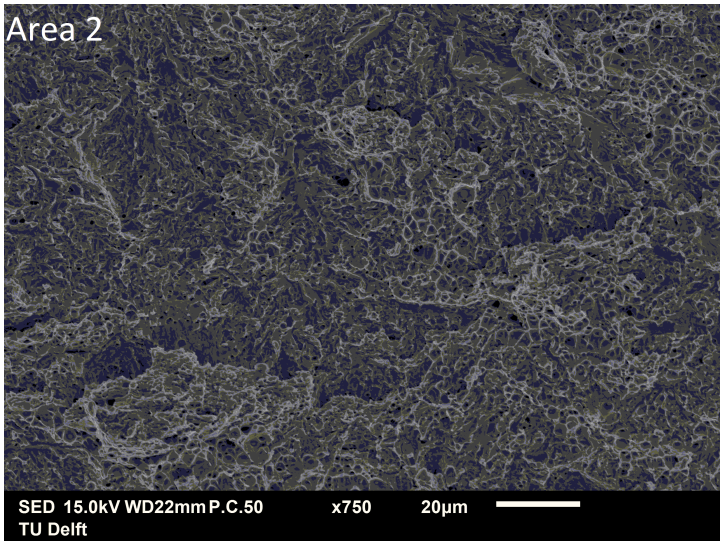

(d)

Figure 4.19: a) A low magnification overview of the fracture surface of a WM specimen tested in 70 bar H_2, b) a magnified view of area 1 from (a), c) a magnified view of area 3 from (a), d) a magnified view of area 2 from (a).

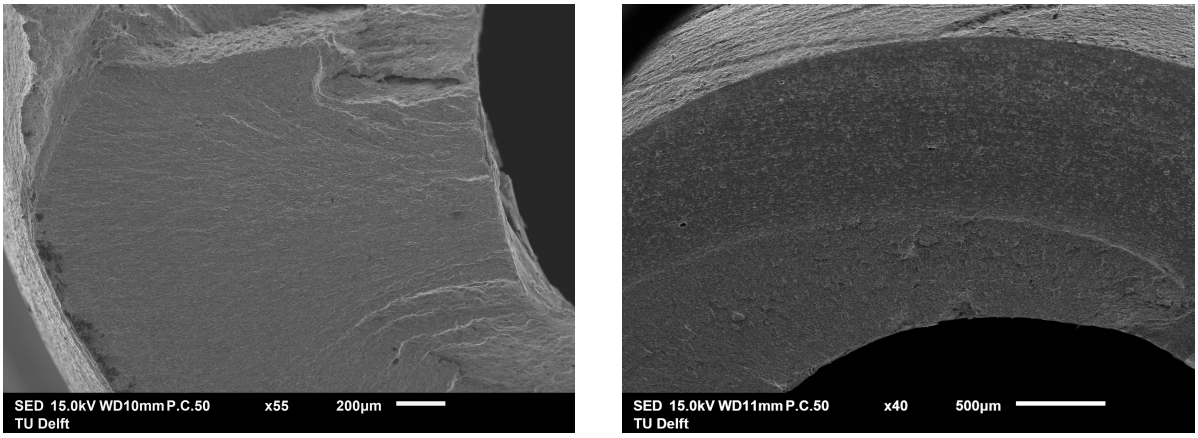

(a) (b)

Figure 4.20: a) Low magnification overview of the area on the fracture surface of the smooth base metal test specimen, tested in hydrogen, where quasi-cleavage (QC) fracture propagated until the outside surface and b) of the top side of the fracture surface of the same specimen tested in 30 bar H_2 showing a transition between QC and microvoid coalescence fracture modes.

Base metal notched tests performed in hydrogen all showed a degree of gradual unloading before fracture, whereas the weld specimens seemed to fracture more abruptly without an unloading period. This time window of decreasing force could be the moment where the crack grows while still being in contact with the hydrogen gas, thereby creating the quasi-cleavage fracture mode. Weld specimens show a smaller region of unloading, which might correspond to their smaller regions of QC fracture observable on their fracture surfaces.

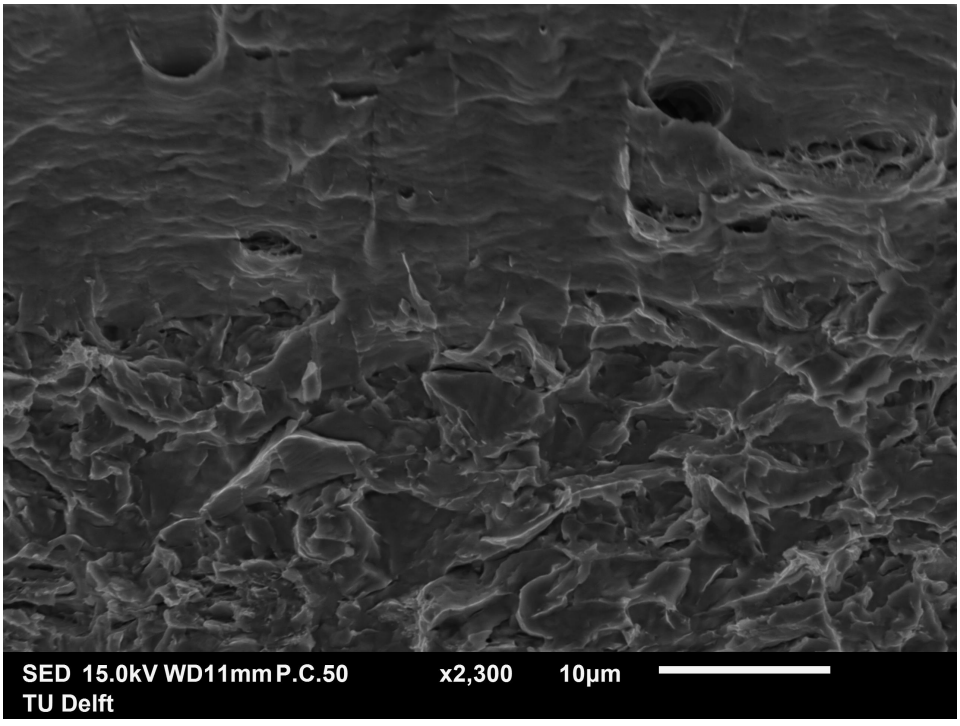

Figure 4.21: A magnified view of the transition zone as seen in Figure 4.20b.

4.4.4. Fracture mechanisms

In their paper discussing smooth facets of QC surfaces, Martin et al. reject the possibility of the AIDE mechanism playing a role in fracture, because they see no clear dislocation structures or gradients that indicate dislocation emission from the surface [37]. However, the findings from this research that the fracture mechanism changes abruptly upon release of the gas do suggest that the presence of the gas itself plays a role in the formation of QC fracture surfaces, which would be compatible with the AIDE mechanism. More in depth study at higher magnifications is needed to provide further insight into this matter. It is possible that the HELP mechanism was supported by the HEDE or HID mechanisms in the tests, but since no intergranular fracture was observed, these mechanisms cannot be proven to have been active. Most likely, hydrogen concentrations in a gaseous environment are too low to cause sufficient reduction in either grain boundary or interatomic bond strength to cause decohesion. The hydrogen concentration increases because of dislocation nucleation during plastic deformation, but any hydrogen trapped in dislocations is more likely to contribute to the HELP or AIDE mechanisms than to cause HEDE or HID fracture.

5

Conclusions and Recommendations

The last chapter of this thesis will present the conclusions that can be drawn from the research. Additionally, it will discuss several recommendations for future research that could answer some of the questions that were left unanswered by this thesis, or were discovered during the research.

5.1. Conclusions

From the research presented in this thesis, several conclusions can be drawn. First of all, the research objectives stated in Chapter 2 can be answered.

1. To develop an in-situ gaseous charging setup with the aim of simulating the charging situation in a pipeline for gaseous hydrogen transport.

   An in-situ gaseous charging setup was developed. By designing a sample geometry that mimics a pipeline including girth weld, a test environment was created that accurately models the environment and locations within the pipe of different metals that are present in a gas pipeline.

2. To validate the setup by testing several hydrogen pressures and characterising changes in mechanical performance of the specimens.

   By testing in both N_2 and H_2 environments, a comparison was made to highlight the effect of hydrogen gas on the tensile performance of the base and weld metals. There were no effects of hydrogen gas on the yield strength or the ultimate tensile strength of the samples. Rather there was a pronounced effect on the ductility of both metals, creating a reduction in ductility and a smaller reduction in cross-sectional area compared to samples tested in a nitrogen environment. The test setup was successfully validated through these experiments.

3. To identify how these hydrogen pressures will alter the fracture behaviour of the weld metal in presence of a stress concentration and what embrittlement mechanisms dominate fracture.

   All samples showed a change in fracture mechanism from micro-void coalescence to quasi cleavage to some degree. In the base metal, this change happened over most of the fracture surface, even without introduction of a notch. The introduction of a notch into the samples did not have an added effect on the fracture mechanism. The weld metal showed QC fracture in a zone surrounding the inside surface of the samples. In each weld sample, the fracture mechanism reverted back towards micro-void coalescence with increasing distance from the inside to the outside edge of the fracture surface for increasing hydrogen pressures. The HELP mechanisms is assumed to dominate fracture behaviour. The data suggests involvement of the AIDE mechanism as well. No evidence of the HEDE/HID mechanisms being present was found.

4. To assess the performance of X60 pipeline steel and its weldment to hydrogen pressures expected to be used in hydrogen pipelines.

By testing under various hydrogen pressures, a decrease in ductility was found at the lowest tested pressure of 30 bar for the weld metal. The base metal was only tested at 100 bar. Furthermore, increasing the pressure led to a decrease in ductility for each increment. The %RA values decreased in a hydrogen environment compared to nitrogen, but varying the pressure did not seem to have an effect on the %RA values. It was shown that both metals are susceptible to HE, but the weld metal is more resistant than the base metal.

Outside of the research questions, other conclusions can also be drawn.

- The behaviour of the notched base metal specimens was shown to be adequately modelled by using an Abaqus plastic deformation model using material input data obtained from the tensile tests on a smooth sample.
- The presence of a blunt notch in the specimens resulted in extra reduction in ductility when testing in hydrogen gas. This effect arises because of regions of tri-axial stresses that are created in the notch. The notch did not show to decrease the %RA area any further than was seen in the smooth samples.
- The measured values for %RA were shown not to be an accurate representation for the reduction in ductility for the metals. Where a trend of decreasing ductility with increasing hydrogen pressure as found from the tensile results, no such effect was visible in the %RA data.
- Fracture was found to initiate from the inside surface of the specimen, both for smooth samples as well as notched samples.
- Since the fracture mode changed from QC to MVC immediately upon release of gas from the specimen, it can be concluded that the concentration of hydrogen that is present in the material alone is not enough to cause QC fracture.

Any effects of hydrogen on the base and weld metal found in this research were only apparent at high amounts of plastic strain, after the onset of necking. The hydrogen concentration cause by presence of high pressure hydrogen gas was not sufficient to have any extra effects on the metals before this point. Since pipelines only operate in the elastic regime with possible occasional low plastic strains, no degradation of UTS or yield strength is expected when transporting hydrogen gas. Gradual changes in geometry like weld toes are not expected to increase the HE effects. There are, however, other perspectives that have not been covered in this research, which will be discussed in the next section.

5.2. Recommendations

Only a fraction of the necessary research to uncover the effects of hydrogen on steel was performed in this thesis. This section discusses other opportunities from research based on findings from this thesis.

1. Since a blunt notch was used in this thesis, the effect of high stress concentrations and high stress tri-axialities was not studied. Sharp notches or crack tips will increase the HE susceptibility of the steel, and they can be present in pipelines. Therefore, they should be studied before any conclusions about the feasibility of transporting hydrogen through pipelines can be made.
2. Because pipelines experience mostly cyclic loading of varying intensity, cyclic tests should be performed. Especially in combination with pre-existing cracks, in-situ fracture toughness testing would provide valuable data for assessing whether pipeline steels and welds will still be safe to operate when defects are considered.
3. It was suggested that fracture initiation is promoted by small irregularities in the surface, like machining scratches. In hydrogen environments, samples were shown to fail due to cracks that originated from them. Applying machining marks could be utilised for in-situ testing to enforce cracking in a certain location. Initiation on the outside surface of a sample instead of the inside surface, for example, could be used to evaluate the effect of the hydrogen gas being in contact with the surface where cracking initiates.

4. For pipeline operating conditions, it could be useful to test different mixtures of H_2 with other gases, so that the pressure and hydrogen concentration can be varied independently. Especially in cases where the gas is released during the test, this method could be used to assess whether the presence of hydrogen gas or the stress state that arises because of the pressure is the cause of a change in fracture mechanism.

5. The necessary pre-charging time and equilibrium conditions of the setup depend on the diffusivity of the metal that is tested, and the equilibrium between sub-surface and gaseous hydrogen. Since these will be different for different metals, they should be independently validated before reliable tests can be performed with them on this setup.

In order to more fundamentally understand the mechanisms of hydrogen embrittlement on steels in general, several approaches have to be taken.

- Hydrogen concentrations should be measured. Not only can pre-charging time be validated in this way, but a direct link between material performance and hydrogen concentration can be made, rather than one between pressure and performance. High resolution measurements are necessary as well, since hydrogen concentrations can vary locally depending on the stress state or the presence of dislocations or other microstructural features like inclusions or grain boundaries. Results relative tot the hydrogen concentration could also be related back to different charging environments.

- Smaller scale characterisation is needed to provide a better understanding of the fracture mechanisms present in HE, because effects happen on a scale that was not observed in this thesis. In the literature, TEM is often used to identify dislocation structures underneath the fracture surface.

- Different microstructures should be tested under similar conditions. Not only base pipeline steels, but especially welds have varying microstructures. Since the microstructure has an influence on multiple variables like the hydrogen equilibrium concentration, the hydrogen diffusivity and the fracture behaviour, every different microstructure will have a different response. This means that different welding procedures will also have a definitive influence on HE characteristics.

- By identifying hydrogen trap sites and linking them to microstructural feature that can be experimentally observed, modelling approaches are necessary in addition to experimental methods to assess HE susceptibility.

Bibliography

[1] R. L. Amaro, E. S. Drexler, and A. J. Slifka. Fatigue crack growth modeling of pipeline steels in high pressure gaseous hydrogen. *International Journal of Fatigue*, 62:249–257, may 2014.

[2] ASTM. G129, standard practice for slow strain rate testing to evaluate the susceptibility of metallic materials to environmentally assisted cracking. *American Association for Testing and Materials*, 2013.

[3] ASTM. G142, standard test method for determination of susceptibility of metals to embrittlement in hydrogen containing environments at high pressure, high temperature, or both. *American Association for Testing and Materials*, 2013.

[4] ASTM. F1624-12, standard test method for measurement of hydrogen embrittlement threshold in steel by the incremental step loading technique. *American Association for Testing and Materials*, 2018.

[5] A. Barnoush. *Hydrogen embrittlement, revisited by in situ electrochemical nanoindentation*. PhD thesis, Universitaet des Saarlandes, 2007.

[6] A. Barnoush and H. Vehoff. Electrochemical nanoindentation: A new approach to probe hydrogen/deformation interaction. *Scripta Materialia*, 55(2):195–198, 2006.

[7] C. D. Beachem. A new model for hydrogen-assisted cracking (hydrogen “embrittlement”). *Metallurgical and Materials Transactions B*, 3(2):441–455, 1972.

[8] L. Briottet, R. Batisse, G. de Dinechin, P. Langlois, and L. Thiers. Recommendations on X80 steel for the design of hydrogen gas transmission pipelines. *International Journal of Hydrogen Energy*, 37(11):9423–9430, jun 2012.

[9] A Brown and C. L. Jones. Hydrogen induced cracking in pipeline steels. *Corrosion*, 40(7):330–336, 1984.

[10] J. Capelle, J. Gilgert, I. Dmytrakh, and G. Pluvinage. Sensitivity of pipelines with steel API X52 to hydrogen embrittlement. *International Journal of Hydrogen Energy*, 33(24):7630–7641, dec 2008.

[11] K. Christmann. Some general aspects of hydrogen chemisorption on metal surfaces. *Progress in surface science*, 48(1-4):15–26, 1995.

[12] J. A. Clum. The role of hydrogen in dislocation generation in iron alloys. *Scripta Metallurgica*, 9 (1):51–58, 1975.

[13] European Commission. A European Green Deal, 2020. URL `https://ec.europa.eu/info/strategy/priorities-2019-2024/european-green-deal_en`. Accessed on 30 August 2020.

[14] L. S. Darken and R. P. Smith. Behavior of hydrogen in steel during and after immersion in acid. *Corrosion*, 5(1):1–16, 1949.

[15] M. B. Djukic, G. M. Bakic, V. S. Zeravcic, A. Sedmak, and B. Rajicic. Hydrogen embrittlement of industrial components: Prediction, prevention, and models. *Corrosion*, 72(7):943–961, 2016.

[16] C. F. Dong, X. G. Li, Z. Y. Liu, and Y. R. Zhang. Hydrogen-induced cracking and healing behaviour of X70 steel. *Journal of Alloys and Compounds*, 484(1-2):966–972, sep 2009.

[17] E. S. Drexler, A. J. Slifka, R. L. Amaro, N. Barbosa, D. S. Lauria, L. E. Hayden, and D. G. Stalheim. Fatigue crack growth rates of API X70 pipeline steel in a pressurized hydrogen gas environment. *Fatigue and Fracture of Engineering Materials and Structures*, 37(5):517–525, 2014.

[18] Elektriska Svetsnings-Aktiebolaget (ESAB). Weld 70S-6. Specification Sheet, 2018.

[19] P. J. Ferreira, I. M. Robertson, and H. K. Birnbaum. Hydrogen effects on the interaction between dislocations. *Acta materialia*, 46(5):1749–1757, 1998.

[20] W. W. Gerberich, R. A. Oriani, M. J. Lji, X. Chen, and T. Foecke. The necessity of both plasticity and brittleness in the fracture thresholds of iron. *Philosophical Magazine A*, 63(2):363–376, 1991.

[21] H. E. Hänninen, T. C. Lee, I. M. Robertson, and H. K. Birnbaum. In situ observations on effects of hydrogen on deformation and fracture of a533b pressure vessel steel. *Journal of materials engineering and performance*, 2(6):807–817, 1993.

[22] H. Hillenbrand, M. Grass, and C. Kalva. Development and production of high strength pipeline steels. niobium science and technology. In *Proc. Int. Symposium on Niobium*, pages 2–5, 2001.

[23] J. P. Hirth. Effects of hydrogen on the properties of iron and steel. *Metallurgical Transactions A*, 11(6):861–890, 1980.

[24] F. Huang, J. Liu, Z. J. Deng, J. H. Cheng, Z. H. Lu, and X. G. Li. Effect of microstructure and inclusions on hydrogen induced cracking susceptibility and hydrogen trapping efficiency of X120 pipeline steel. *Materials Science and Engineering: A*, 527(26):6997–7001, oct 2010.

[25] American Petroleum Institute. Api 5l specification for line pipe, forty-third edition, 2004.

[26] ASME Internatinoal. Rules for construction of pressure vessels part viii division 1. *ASME Boiler and Pressure Vessel Code*, 2010.

[27] T. Y. Jin, Z. Y. Liu, and Y. F. Cheng. Effect of non-metallic inclusions on hydrogen-induced cracking of API5L X100 steel. *International Journal of Hydrogen Energy*, 35(15):8014–8021, aug 2010.

[28] W. H. Johnson. On some remarkable changes produced in iron and steel by the action of hydrogen and acids. *Proceedings of the Royal Society of London*, 23(156-163):168–179, 1875.

[29] I. H. Katzarov and A. T. Paxton. Hydrogen embrittlement ii. analysis of hydrogen-enhanced decohesion across (111) planes in α-fe. *Phys. Rev. Materials*, 1:033603, Aug 2017.

[30] K. Kiuchi and R. B. McLellan. The solubility and diffusivity of hydrogen in well-annealed and deformed iron. In *Perspectives in Hydrogen in Metals*, pages 29–52. Elsevier, 1986.

[31] M. Koyama, C. C. Tasan, E. Akiyama, K. Tsuzaki, and D. Raabe. Hydrogen-assisted decohesion and localized plasticity in dual-phase steel. *Acta Materialia*, 70:174–187, 2014.

[32] S. P. Lynch. Environmentally assisted cracking: Overview of evidence for an adsorption-induced localised-slip process. *"Acta Metallurgica"*, 36(10):2639 – 2661, 1988.

[33] S. P. Lynch. Mechanisms of hydrogen assisted cracking–a review. *Hydrogen effects on material behaviour and corrosion deformation interactions*, pages 449–466, 2003.

[34] S. P. Lynch. Hydrogen embrittlement (HE) phenomena and mechanisms. *Stress corrosion cracking: Theory and practice*, i:90–130, 2011.

[35] I. Maroef, D. L. Olson, M. Eberhart, and G. R. Edwards. Hydrogen trapping in ferritic steel weld metal. *International Materials Reviews*, 47(4):191–223, 2002.

[36] M. L. Martin, J. A. Fenske, G. S. Liu, P. Sofronis, and I. M. Robertson. On the formation and nature of quasi-cleavage fracture surfaces in hydrogen embrittled steels. *Acta Materialia*, 59(4): 1601–1606, 2011.

[37] M. L. Martin, I. M. Robertson, and P. Sofronis. Interpreting hydrogen-induced fracture surfaces in terms of deformation processes: a new approach. *Acta Materialia*, 59(9):3680–3687, 2011.

[38] R. B. McLellan and Z. R. Xu. Hydrogen-induced vacancies in the iron lattice. *Scripta Materialia*, 36(10), 5 1997.

[39] E. Merson, A. V. Kudrya, V. A. Trachenko, D. Merson, V. Danilov, and A. Vinogradov. Quantitative characterization of cleavage and hydrogen-assisted quasi-cleavage fracture surfaces with the use of confocal laser scanning microscopy. *Materials Science and Engineering A*, 665:35–46, 2016.

[40] T. Michler and M. P. Balogh. Hydrogen environment embrittlement of an ods raf steel–role of irreversible hydrogen trap sites. *International Journal of Hydrogen Energy*, 35(18):9746–9754, 2010.

[41] M. A. Mohtadi-Bonab, J. A. Szpunar, and S. S. Razavi-Tousi. A comparative study of hydrogen induced cracking behavior in API 5L X60 and X70 pipeline steels. *Engineering Failure Analysis*, 33:163–175, oct 2013.

[42] M. A. Mohtadi-Bonab, J. A. Szpunar, R. Basu, and M. Eskandari. The mechanism of failure by hydrogen induced cracking in an acidic environment for API 5L X70 pipeline steel. *International Journal of Hydrogen Energy*, 2015.

[43] M. A. Mohtadi-Bonab, M. Eskandari, K. M. M. Rahman, R. Ouellet, and J. A. Szpunar. An extensive study of hydrogen-induced cracking susceptibility in an API X60 sour service pipeline steel. *International Journal of Hydrogen Energy*, 41(7):4185–4197, feb 2016.

[44] I. Moro, L. Briottet, P. Lemoine, E. Andrieu, C. Blanc, and G. Odemer. Hydrogen embrittlement susceptibility of a high strength steel X80. *Materials Science and Engineering: A*, 527(27-28): 7252–7260, oct 2010.

[45] M. Nagumo. Hydrogen related failure of steels–a new aspect. *Materials Science and Technology*, 20(8):940–950, 2004.

[46] N. E. Nanninga, Y. S. Levy, E. S. Drexler, R. T. Condon, A. E. Stevenson, and A. J. Slifka. Comparison of hydrogen embrittlement in three pipeline steels in high pressure gaseous hydrogen environments. *Corrosion Science*, 59:1–9, jun 2012.

[47] T Neeraj, R Srinivasan, and J. Li. Hydrogen embrittlement of ferritic steels: observations on deformation microstructure, nanoscale dimples and failure by nanovoiding. *Acta Materialia*, 60 (13-14):5160–5171, 2012.

[48] Gasunie new energy. NortH2, 2020. URL `https://www.gasunienewenergy.nl/projecten/north2`. Accessed on 7 July 2020.

[49] M. G. Nicholas and C. F. Old. Liquid metal embrittlement. *Journal of Materials Science*, 14(1): 1–18, 1979.

[50] V. Olden, A. Alvaro, and O. M. Akselsen. Hydrogen diffusion and hydrogen influenced critical stress intensity in an API X70 pipeline steel welded joint – Experiments and FE simulations. *International Journal of Hydrogen Energy*, 37(15):11474–11486, aug 2012.

[51] R. A. Oriani. The diffusion and trapping of hydrogen in steel. *Acta Metallurgica*, 1970.

[52] OSF. Background:IJVER, 2019. URL `https://offshoreservicefacilities.nl/ijmuiden-ver`. Accessed on 25 October 2019.

[53] OSF. News, 2019. URL `https://offshoreservicefacilities.nl/news`. Accessed on 25 October 2019.

[54] M. Panico, D. Baker, Sh. Nawathe, A. Bahrami, and D. Fairchild. Effect of testing variables on fracture toughness in sour environment. *Proceedings of the International Offshore and Polar Engineering Conference*, 2015-January:134–139, 2015.

[55] G. T. Park, S. U. Koh, H. G. Jung, and K. Y. Kim. Effect of microstructure on the hydrogen trapping efficiency and hydrogen induced cracking of linepipe steel. *Corrosion Science*, 50(7):1865–1871, jul 2008.

[56] L. N. Pussegoda and W. R. Tyson. Relationship between microstructure and hydrogen susceptibility of some low-carbon steels. *TMS/AIME*, pages 349–360, 1981.

[57] K. M. Mostafijur Rahman, M. A. Mohtadi-Bonab, R. Ouellet, and J. Szpunar. A Comparative Study of the Role of Hydrogen on Degradation of the Mechanical Properties of API X60, X60SS, and X70 Pipeline Steels. *Steel Research International*, 1900078:1–9, 2019.

[58] Rijksoverheid. HyWay 27 gaat van start: EZK, Gasunie en TenneT onderzoeken inzet landelijk gasnet voor de ontwikkeling van waterstofinfrastructuur, 2020. URL https://www.rijksoverheid.nl/actueel/nieuws/2020/06/15/hyway-27-gaat-van-start-ezk-gasunie-en-tennet-onderzoeken-inzet-landelijk-gasnet-voor-de-ontwikkeling-van-waterstofinfrastructuur. Accessed on 7 July 2020.

[59] P. C. Rivera, V. P. Ramunni, and P Bruzzoni. Hydrogen trapping in an api 5l x60 steel. *Corrosion Science*, 54:106–118, 2012.

[60] I. M. Robertson. The effect of hydrogen on dislocation dynamics. *Engineering Fracture Mechanics*, 64(5):649–673, 1999.

[61] A. Sieverts. The absorption of gases by metals. *Zeitschrift für Metallkunde*, 21:37–46, 1929.

[62] M. Skjellerudsveen, O. M. Akselsen, V. Olden, R. Johnsen, and A. Smirnova. Effect of microstructure and temperature on hydrogendiffusion and trapping in x70 grade pipeline steel and itsweldments. 2010.

[63] EE J. Song, S. W. Baek, S. H. Nahm, and U. B. Baek. Notched-tensile properties under high-pressure gaseous hydrogen: Comparison of pipeline steel X70 and austenitic stainless type 304L, 316L steels. *International Journal of Hydrogen Energy*, 42(12):8075–8082, mar 2017.

[64] M. A. Stopher and P. E. J. Rivera-Diaz-del Castillo. Hydrogen embrittlement in bearing steels. *Materials Science and Technology*, 32(11):1184–1193, 2016.

[65] A. Syrotyuk and R. Leshchak. Specific effects of hydrogen concentration on resistance to fracture of ferrite-pearlitic pipeline steels. *Procedia Structural Integrity*, 16:113–120, jan 2019.

[66] TenneT, DNV GL, Gasunie. Power-to-hydrogen ijmuiden ver. Technical report, DNV GL, 2019.

[67] TNO. From Grey and Blue to Green Hydrogen, 2020. URL https://www.tno.nl/en/focus-areas/energy-transition/roadmaps/towards-co2-neutral-fuels-and-feedstock/hydrogen-for-a-sustainable-energy-supply/. Accessed on 7 July 2020.

[68] Topsector Energie. Feasibility system integration gas + wind energyisland ijmuiden ver, 2019. URL https://projecten.topsectorenergie.nl/projecten/feasibility-system-integration-gas-wind-energy-island-ijmuiden-ver-00032947. Accessed on 21 October 2019.

[69] A. R. Troiano. The role of hydrogen and other interstitials in the mechanical behavior of metals. *trans. ASM*, 52:54–80, 1960.

[70] A. Turnbull. Hydrogen diffusion and trapping in metals. In *Gaseous hydrogen embrittlement of materials in energy technologies*, pages 89–128. Elsevier, 2012.

[71] A. V. Uluc. *Hydrogen sorption and desorption properties of Pd-alloys and steels investigated by electrochemical methods and mass spectroscopy.* PhD thesis, Delft Technical University, 2015.

[72] M. Wang, E. Akiyama, and K. Tsuzaki. Crosshead speed dependence of the notch tensile strength of a high strength steel in the presence of hydrogen. *Scripta Materialia*, 53(6):713–718, sep 2005.

[73] M. Wang, E. Akiyama, and K. Tsuzaki. Effect of hydrogen on the fracture behavior of high strength steel during slow strain rate test. *Corrosion Science*, 49(11):4081–4097, nov 2007.

[74] E. Wiebes. Kamerbrief routekaart windenergie op zee 2030, 2018. URL https://www.rijksoverheid.nl/documenten/kamerstukken/2018/03/27/kamerbrief-routekaart-windenergie-op-zee-2030. Accessed on 21 October 2019.

[75] E. Wiebes. Kamerbrief voortgang uitvoering windenergie op zee 2030, 2019. URL https://www.rijksoverheid.nl/documenten/kamerstukken/2019/04/05/kamerbrief-over-de-voortgang-uitvoering-routekaart-windenergie-op-zee-2030. Accessed on 21 October 2019.

[76] P. M. Withagen. De invloed van de reksnelheid op de waterstofverbrossing van x-56 staal. Master's thesis, Delft Technical University, 1994.

[77] H. B. Xue and Y. F. Cheng. Hydrogen permeation and electrochemical corrosion behavior of the X80 pipeline steel weld. *Journal of Materials Engineering and Performance*, 22(1):170–175, 2013.

[78] Y. Zhao, M. Y. Seok, I. C. Choi, Y. H. Lee, S. J. Park, U. Ramamurty, J. Y. Suh, and J. zi. Jang. The role of hydrogen in hardening/softening steel: Influence of the charging process. *Scripta Materialia*, 107:46–49, oct 2015.

A

Test Details

The top adapter of the test setup only acts as a clamp to be able to fit the sample with a screw connection. The bottom adapter has channels manufactured into it to allow for gas entry and exit through the adapter and into the sample, and is connected to two gas bottles. A sealing is added into the screw connection with the sample to prevent leakage and maintain gas pressure throughout the test. The two gas bottles, one for N_2 and one for H_2, have built in pressure regulation valves. They are connected by two more valves (Valves 1 and 2 in Figure A.1) and a T-piece to a tube that reaches valves 3, 4, and a pressure gauge before feeding into the bottom adapter for the tensile sample. This side of the setup supplies either N_2 or H_2 to the sample at the right pressure. The valves are each connected in a set of a needle valve and a plug valve, because the needle valve provides better leakage performance while the plug valve makes it easier to see whether it is open or closed, which is important for safety reasons. On the other side of the adapters, a tube goes outward to a relief valve (5 and 6) and a valve that connects to a vacuum gauge (7 and 8) and vacuum tubing. The relief valve is an essential part of the design in order to relieve the sample of high pressure before it is connected to the vacuum tubing. It can also be used in case a test needs to be terminated before completion to safely let out the hydrogen gas away from any ignition sources. After the relieve valve, a final valve opens to connect the high pressure tubing to a compound pressure gauge that measures vacuum, and a vacuum pump that can evacuate the setup of any gas. This is necessary because the whole system needs to be purged with nitrogen several times before hydrogen is let into the system, to make sure no oxygen is left to inhibit the absorption of hydrogen into the sample. This particular valve placement allows for a section of the tubing to be fully closed-off, including the sample. The gas bottles only need to be open during pressurisation of the system, and can be closed during testing because the containment volume is closed off and leak tight. In this way, the only gas that can escape is that from the containment volume, which has a volume of just $5\,\mathrm{mL}$.

Before testing with hydrogen, the system needs to be flushed with nitrogen gas, which is done according to the following steps:

- The sample is placed in the setup and the setup is pressurised with N_2 up to a low pressure.
- The pressure is let off with the release valve, and the whole system is evacuated of any gas. The vacuum pump is kept on for $3\,\mathrm{min}$
- The above steps are repeated twice more.
- This pressure is held for at least 10 minutes to check for any leaks.
- If no leaks are identified, the system is pressurised with H_2 gas up to the pressure that is needed for the test.
- This pressure is held overnight for approximately $17\,\mathrm{h}$.

Steps for any actions that need to be taken during the test are the following:

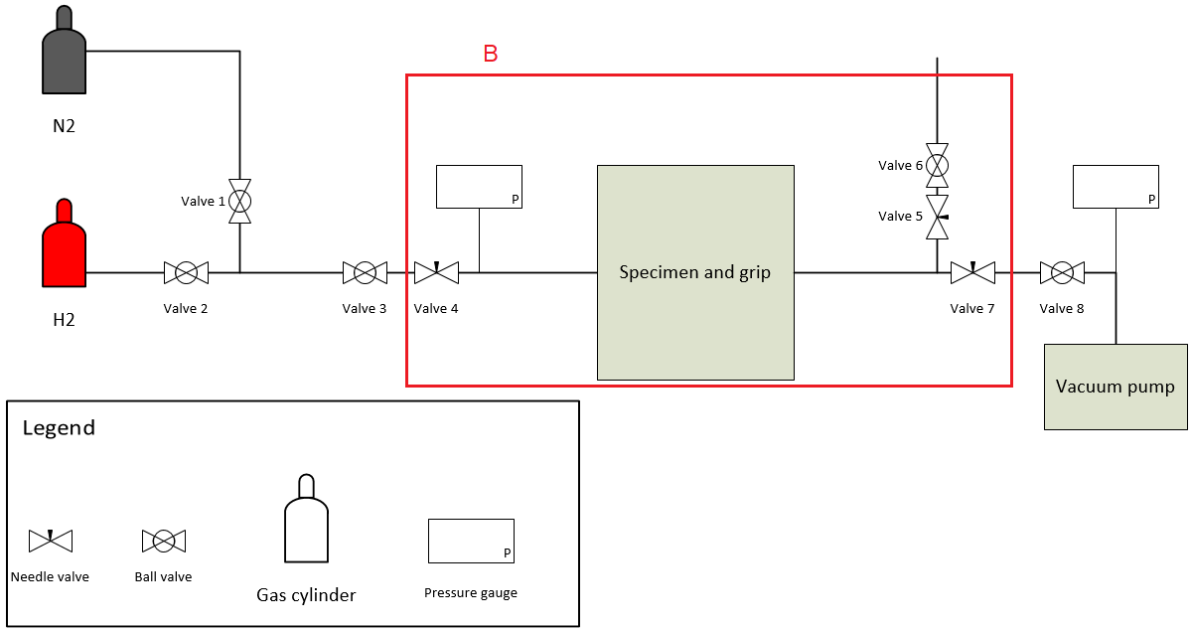

Figure A.1: A graphic overview of the test setup. The highlighted area is shown in Figure 3.7.

- A preload of $1000\,\mathrm{N}$ is applied to the sample to remove any play in the connections.
- The extensometer is attached to the sample.
- The test commences with a cross-head displacement speed of $1.5\,\mathrm{mm\,h^{-1}}$.
- After a set strain, the extensometer is removed.
- The test continues until the sample fractures. Any gas that is in the system will be released.
- If hydrogen was used during the test, the system is briefly flushed with nitrogen gas to avoid any combustion of hydrogen that is left in the system.

B

Specimen details

There are two major advantages to machining samples from the orientation chosen in this thesis. Firstly, this eliminates any problems that might arise due to the curvature of the pipe material, since the samples have the same longitudinal direction as the pipe. This means that the only constraint to the specimen dimensions is the thickness of the pipe wall. Secondly, this orientation allows for the girth weld steel to be included in the specimen. The samples were machined as cylinders with a diameter of $14\,\mathrm{mm}$, that were thinned to $10\,\mathrm{mm}$ in the gauge length area which is $40\,\mathrm{mm}$ long. On both sides of the sample, part of the remaining length was threaded with M14x2 thread. A gauge length of $10\,\mathrm{mm}$ means that the first and last weld passes of the girth weld are not included in the sample if it is milled from the middle section of the wall thickness. This eliminates any effect of strain remaining in these passes.

The thinned portion of the sample near the hole entry is used to create a pressure tight seal with the bottom adapter. The other side of the sample is thinned to allow the blind side of the hole to protrude past the threading. This is important since the blind end of the hole will create a big change in cross-sectional area of the specimen, which will result in a stress concentration. The threads themselves will also create stress concentrations, and if these two were to interact it could create a situation where the sample fails within the thread length, especially when in contact with hydrogen. When the hole protrudes past the thread, the end of the sample holds no load, so there will be interference of stress fields as a result of the blind hole.

ASTM G142 describes the use of a sharp notch when testing in a hydrogen environment [3]. However, the zone of large hydrostatic stress resulting from a sharp notch would have a very large influence on the fracture when hydrogen is introduced into the material. It is expected that the sample would fracture in a brittle way even at lower hydrogen pressures. Because of the probabilistic nature of brittle fracture, a large amount of tests would be needed to be able to draw any conclusions about mechanical performance. Therefore, a blunter notch was designed that limits the amount of hydrostatic stress and stress triaxiality in the sample so that effects of varying pressure can be measured with a smaller amount of samples. This geometry is a notch with a depth of $1\,\mathrm{mm}$, which results in a diameter inside the notch of $8\,\mathrm{mm}$ and a notch radius of $4\,\mathrm{mm}$. This is shown in Figure B.1.

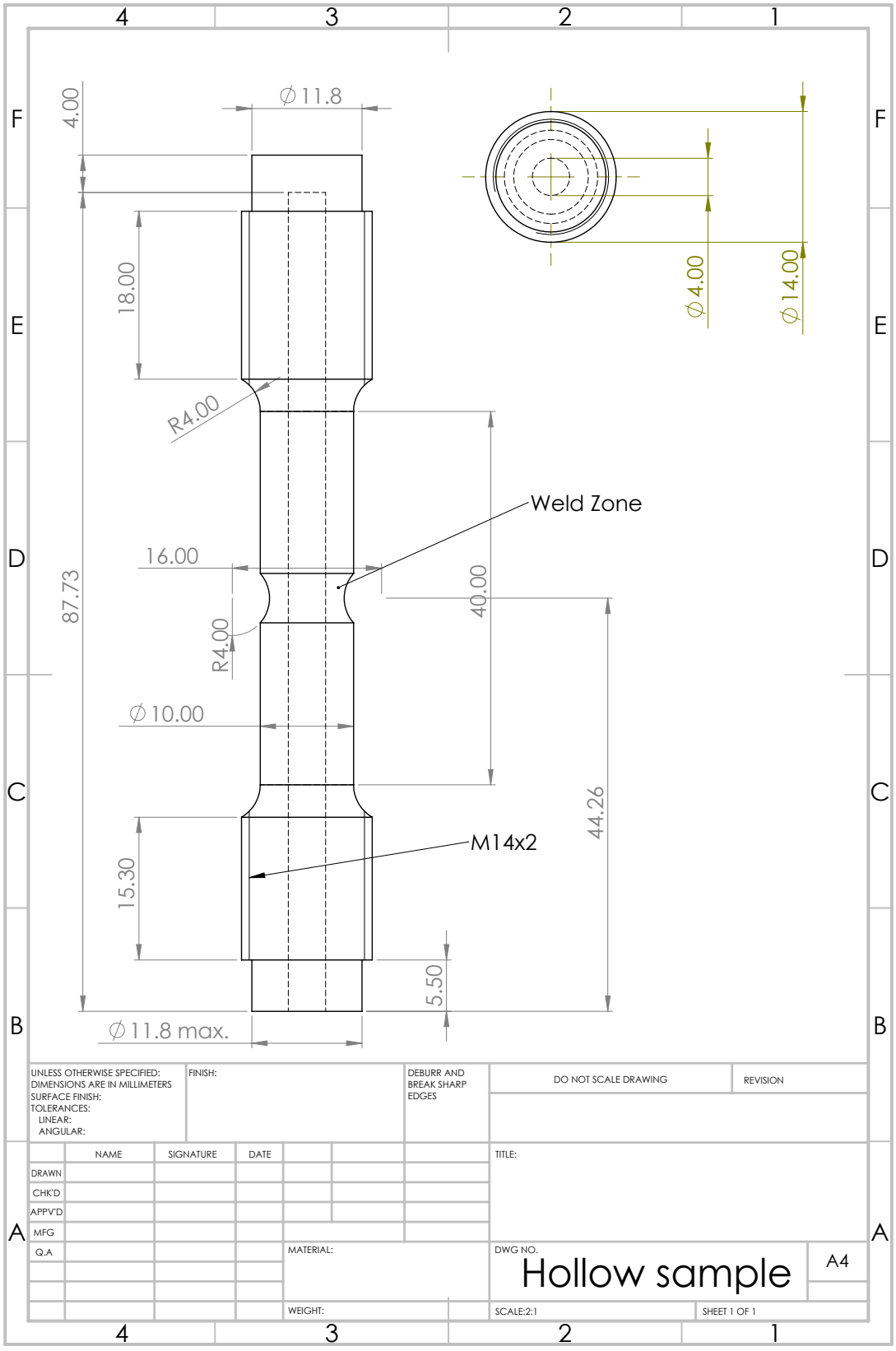

Figure B.1: The technical drawing of the sample geometry

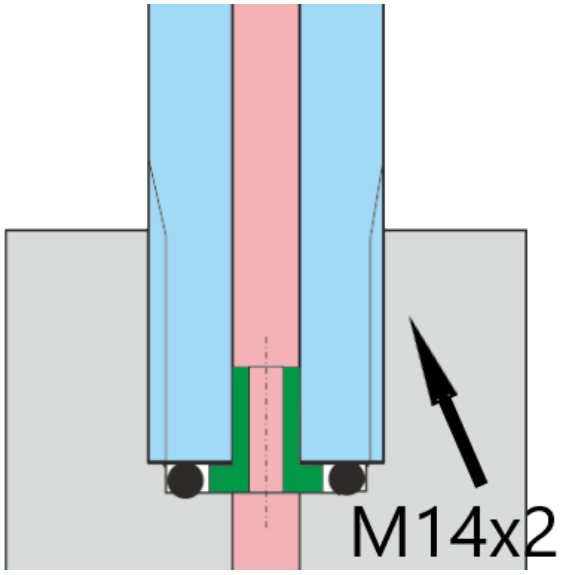

Figure B.2: A schematic overview of the sealing between the bottom adapter (grey) and the tensile samples (blue). An aluminium insert (green) is used to form a fitting space for an O-ring (black) to create a pressure tight seal for the gas.

A schematic overview of the seal between the bottom adapter and the sample is given in Figure B.2. To create a pressure tight sealing, an insert is placed into the hole in the sample in order to space it 1.6 mm from a flat surface that was machined into the grip. A rubber O-ring seal is placed around the insert in the grip. This creates an enclosed space for the O-ring to lie in, which is required for an O-ring to seal properly. In this way, the O-ring will separate the gas flow channel from the threading, which is not leak tight in itself. A seal of this type does not require compressive force to work. This means that the sample will not have to be tightly screwed into the adapter, which could damage the O-ring and could create shear stresses in the sample.

C

Tensile Curves

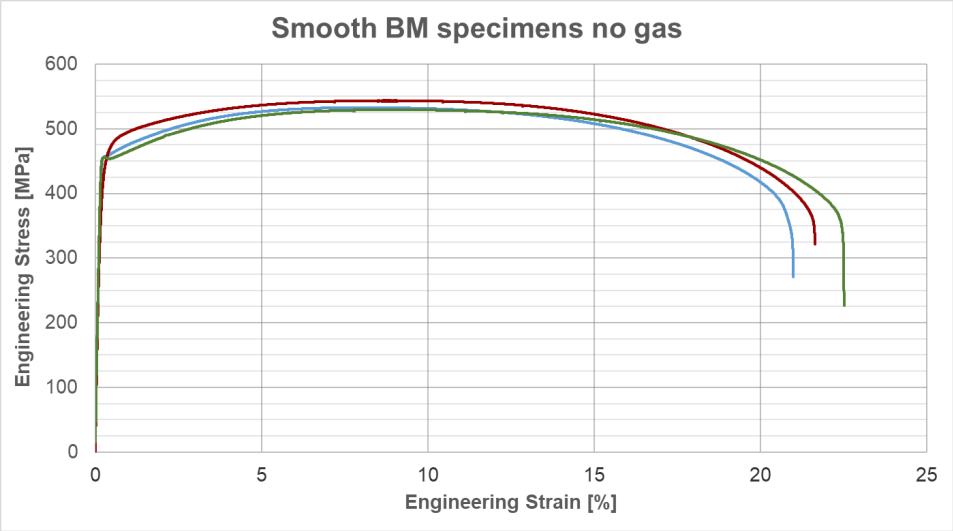

(a)

(b)

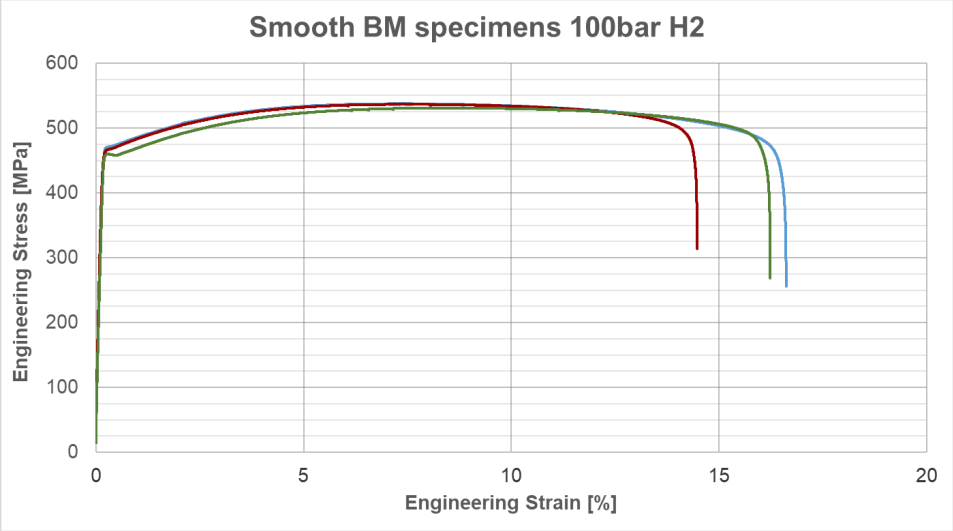

(c)

Figure C.1: The tensile curves for the smooth base metal specimens tested a) without gas, b) in 100 bar N_2 and c) in 100 bar H_2.

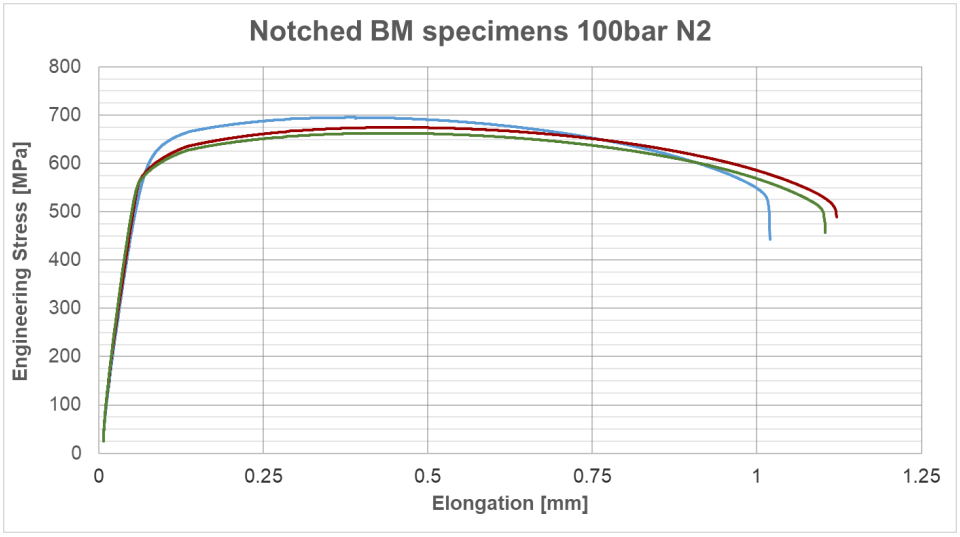

(a)

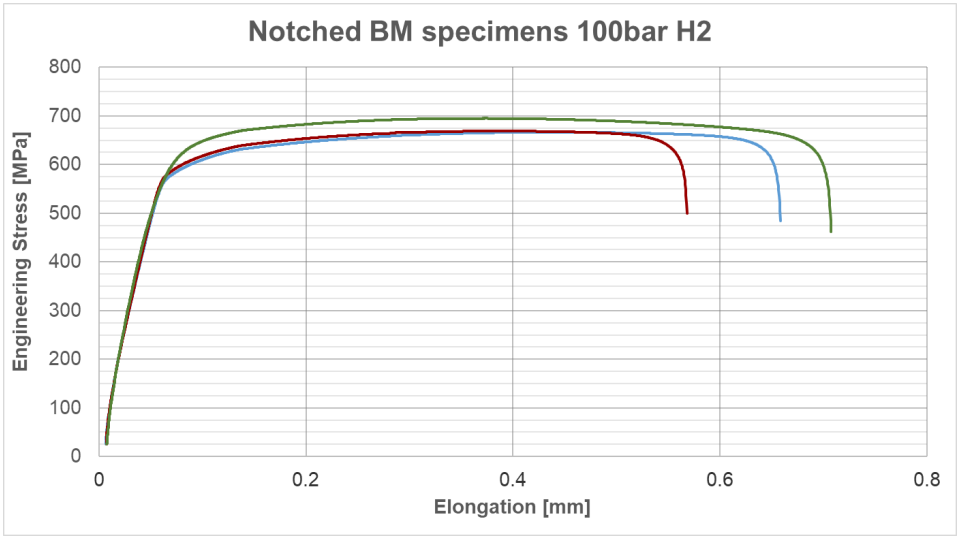

(b)

Figure C.2: The tensile curves for the notched base metal specimens tested a) in 100 bar N_2 and b) in 100 bar H_2.

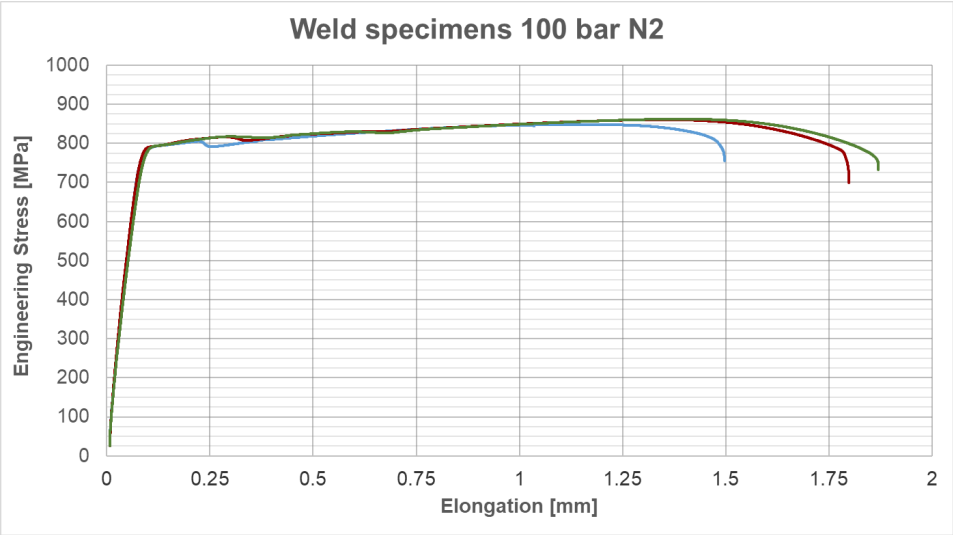

(a)

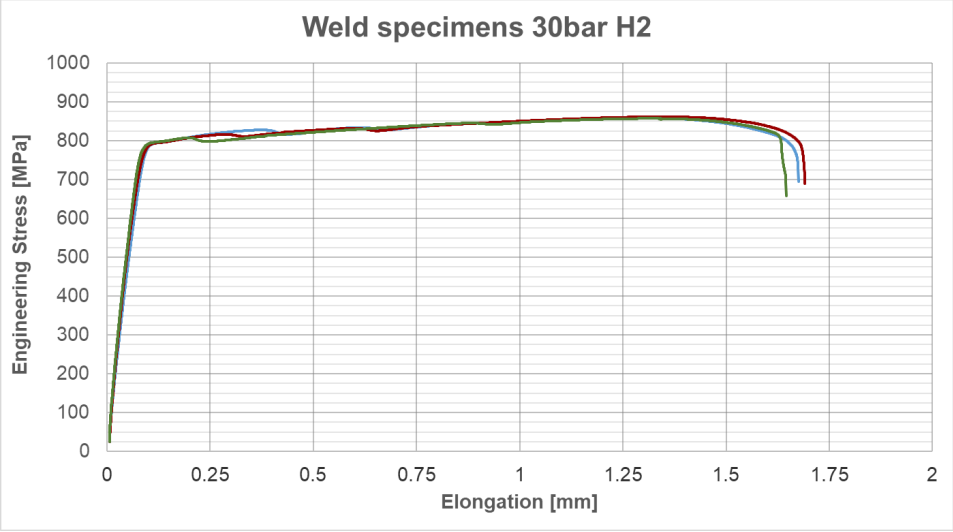

(b)

Figure C.3: The tensile curves for the weld metal specimens tested a) in 100 bar N_2 and b) in 30 bar H_2.

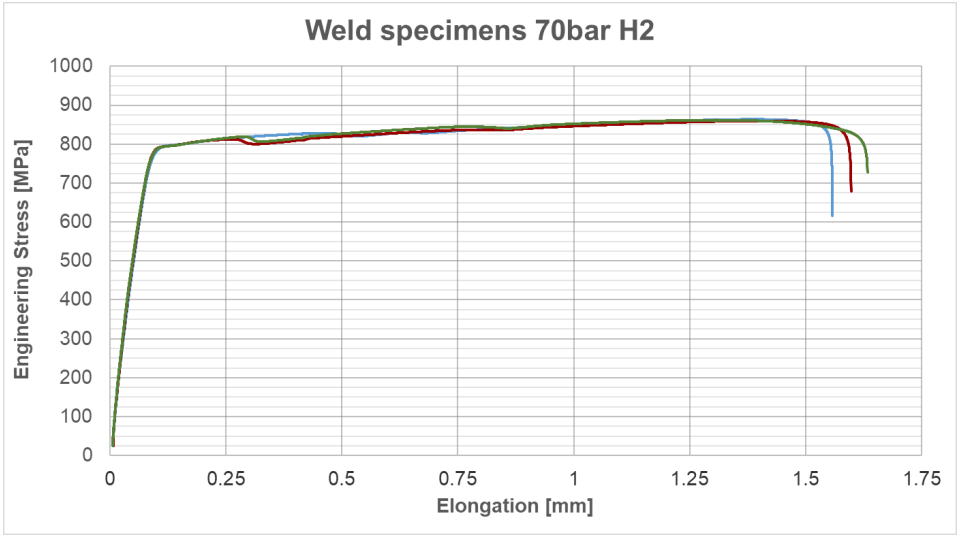

(a)

(b)

Figure C.4: The tensile curves for the weld metal specimens tested a) in 70 bar H_2 and b) in 100 bar H_2.